VERY HIGH ENERGY GAMMA-RAY OBSERVATION OF THE RADIO GALAXY M 87

by

Chiumun Michelle Hui

A dissertation submitted to the faculty of
The University of Utah
in partial fulfillment of the requirements for the degree of

Doctor of Philosophy

in

Physics

Department of Physics and Astronomy

The University of Utah

December 2011

The University of Utah Graduate School

STATEMENT OF DISSERTATION APPROVAL

The dissertation of **Chiumun Michelle Hui**

has been approved by the following supervisory committee members:

Stephan L. LeBohec	, Chair	**Oct 26, 2011** Date Approved
David S. Chapman	, Member	**Oct 26, 2011** Date Approved
David B. Kieda	, Member	**Oct 26, 2011** Date Approved
Clayton C. Williams	, Member	**Oct 26, 2011** Date Approved
Paolo Gondolo	, Member	Date Approved

and by **David Kieda**, Chair of the Department of **Physics and Astronomy**

and by Charles A. Wight, Dean of The Graduate School.

ABSTRACT

The majority of the known extragalactic very high energy (E>100 GeV) gamma ray emitting objects are blazars, active galactic nuclei with relativistic jets aligned close to the line of sight. Due to this geometry, the location of the gamma-ray emission along the jet is unclear. M 87 is a nearby radio galaxy with its jet misaligned with the line of sight. The proximity of M 87 and the jet misalignment allow detailed studies of spatially resolved emission regions in the radio, optical, and X-ray wavebands. The jet is unresolved in the gamma-ray regime, but contemporaneous flux variability measurements with other wavelengths provide a unique opportunity to constrain the emission origin and mechanisms responsible for high energy gamma-ray emission from an active galactic nucleus.

Ground-based imaging telescopes are used to observe the gamma-ray sky by detecting the Cherenkov light from the electromagnetic cascade initiated by gamma rays interacting with the Earth's atmosphere. The Very Energetic Radiation Imaging Telescope Array System (VERITAS) has monitored very high energy gamma-ray emission from M 87 since 2007. Over 170 hours of M 87 observations have been performed by the VERITAS array between 2007 and 2010. Flaring activities have been observed in 2008 and 2010 with flux variability in the time scale of days and with flux level up to 10 times the average nonflaring flux of M 87. The shortest variability time scale observed by VERITAS is 0.9 days, which constrains the size of the emission region. Simultaneous multiwavelength observations from radio to TeV gamma rays during the 2009 nonflaring period yielded a spectral energy distribution that is better described by leponic models instead of hadronic or large scale models. The details and implications of the VERITAS M 87 result are presented in this dissertation.

For my parents, who encouraged me to pursue my dream and have never doubted me.

CONTENTS

LIST OF FIGURES

LIST OF TABLES

ACKNOWLEDGMENTS

I would like to thank my advisor Stephan LeBohec, who has guided me every step of the way. He is a Renaissance man who has helped me progress not only as a scientist but also in life. I have had many fruitful discussions with him on topics varied from the latest work problem I encountered to beekeeping. I would also like to thank everyone in the University of Utah gamma-ray group: Dave Kieda for sharing his extensive knowledge; Pierre Colin for laying the ground work necessary for many of my projects and for the ski adventures; Stephane Vincent for his theoretical point of view and jokes; Sagar Godambe for all the interesting discussions both academic and cultural; Gary Finnegan for all the computing tricks that made my life much easier; and my office mate Paul Nuñez for helping me whenever I was stuck and listening to me ramble over many cups of coffee. Many thanks to the hospitable people at the VERITAS basecamp who have made all those night shifts enjoyable, and to my VERITAS collaborators who have taught me many things relating to the experiment and more.

Thank you to all my wonderful friends, in particular Nick Borys and Monica Allen, who gave me new perspectives on my work and put up with my shenanigans. I am very grateful to my parents and my sister for all their support and their unwavering faith in me. Lastly, I would like to express my gratitude to Dustin Winslow for supporting me through the past 5 years and surviving all my tantrums. He is my rock and is invaluable to me especially during the past few stressful months.

CHAPTER 1

INTRODUCTION

Gamma rays are the most energetic photons in the electromagnetic spectrum, spanning at least 8 decades of energy from 10^6 eV to greater than 10^{14} eV. While cosmic rays are the most energetic particles observed in the sky, they are composed of mostly protons and therefore affected by the interstellar and intergalactic magnetic fields. A gamma-ray photon does not experience this interference and is one of the most energetic radiation that leads back to its emission origin. Gamma rays can also be produced via cosmic-ray interaction in the interstellar medium. Through the study of gamma rays, we can gain insights into particle acceleration processes and environments of both galactic and extragalactic objects. Neutrinos, being charge-free, also have the same properties. They are products of hadronic interactions. However, currently there are only two known neutrino sources, the Sun from its core nuclear reactions, and the supernova SN 1987A. Neutrino astronomy is still in its early development stage.

Due to the large interaction cross section of gamma rays, the Earth's atmosphere is opague to them and cosmic gamma-ray photons cannot be directly observed from the ground. One solution is to go outside the Earth's atmosphere, either via satellite in space or balloon-borne experiment. Cosmic gamma-ray sources typically have energy spectra that follow a power-law distribution, which means the higher energy photons will have a lower flux than the less energetic photons. Therefore, space-based detectors are only viable up to 10^{11} eV energies due to the small collection area. Unlike optical space telescopes, in which optical photons are reflected by mirrors onto the detector to increase collection area, gamma rays cannot be reflected. Therefore the collection area is determined by the detector size. Currently there are two gamma-ray space telescopes, AGILE, sensitive from 30 MeV to 50 GeV with a 2.5 steradian field of view (Tavani et al., 2009), and the Fermi Gamma-ray Space Telescope, sensitive from 20 MeV to 300 GeV with a 2.4 steradian field of view (Atwood et al., 2009) .

To observe the very high energy (VHE, $10^{11} - 10^{14}$ eV) gamma rays, ground-based

imaging telescopes are used instead to observe the secondary products of the interaction between VHE gamma rays and the Earth's atmosphere. In 1948, Blackett suggested that cosmic-ray particles travelling through the atmosphere should produce a small contribution of light in the night sky due to Cherenkov radiation. Several years later, Galbraith & Jelley (1953) discovered light pulses associated with cosmic radiation with an experiment of a photomultiplier placed at the focus of a mirror and Geiger counters looking for coincidence between light pulses and cosmic particles. In the 1960s, the supernova remnant Crab Nebula, the radio galaxy M 87, and the starburst galaxy M82, were proposed as detectable sources of gamma rays (e.g., Rieke & Weekes, 1969). Initially gamma-ray source detection was scarce and unreliable due to difficulties in distinguishing gamma-ray signal from the cosmic-ray background signal. It was not until the detection of the Crab Nebula above 700 GeV at a statistical significance of 9 standard deviations (σ) above the background signal, reported in 1989 using a technique that rejects 98% of the background (Weekes et al., 1989), that the imaging atmospheric Cherenkov technique was validated. Currently there are three operating imaging atmospheric Cherenkov arrays, VERITAS in the US, MAGIC in the Canary Islands, and HESS in Namibia.

1.1 The gamma-ray sky

1.1.1 Galactic objects

Within our galaxy, there are several types of VHE gamma-ray sources: supernova remnants, pulsar wind nebulae, X-ray binaries, and unidentified objects. Supernova is a potential ending of a star's lifecycle. When an aging star with mass > 8 solar masses ($M_\odot$) runs out of hydrogen for nuclear fusion and begins burning higher mass elements, eventually the reaction becomes endothermic and the core of the star collapses due to gravity and results in an explosion (Ostlie & Carroll, 1996). If the star's initial mass is $> 25\,M_\odot$, a black hole is formed after the supernova; if the initial mass is $< 25\,M_\odot$, a neutron star is formed instead. The star's material ejected from the core-collapse supernova would then become part of the supernova remnant (green circles in Figure 1.1). Pulsar wind nebulae (pink circles in Figure 1.1) are supernova remnants with a rotating neutron star (also called a pulsar) at the center. Gamma rays may be produced via inverse Compton scattering from electrons accelerated by the shockwave of the supernova or the strong rotating magnetic field of a pulsar, or by cosmic-ray interaction with the supernova remnant. The environment of a supernova remnant is believed to be capable of accelerating protons and other charged

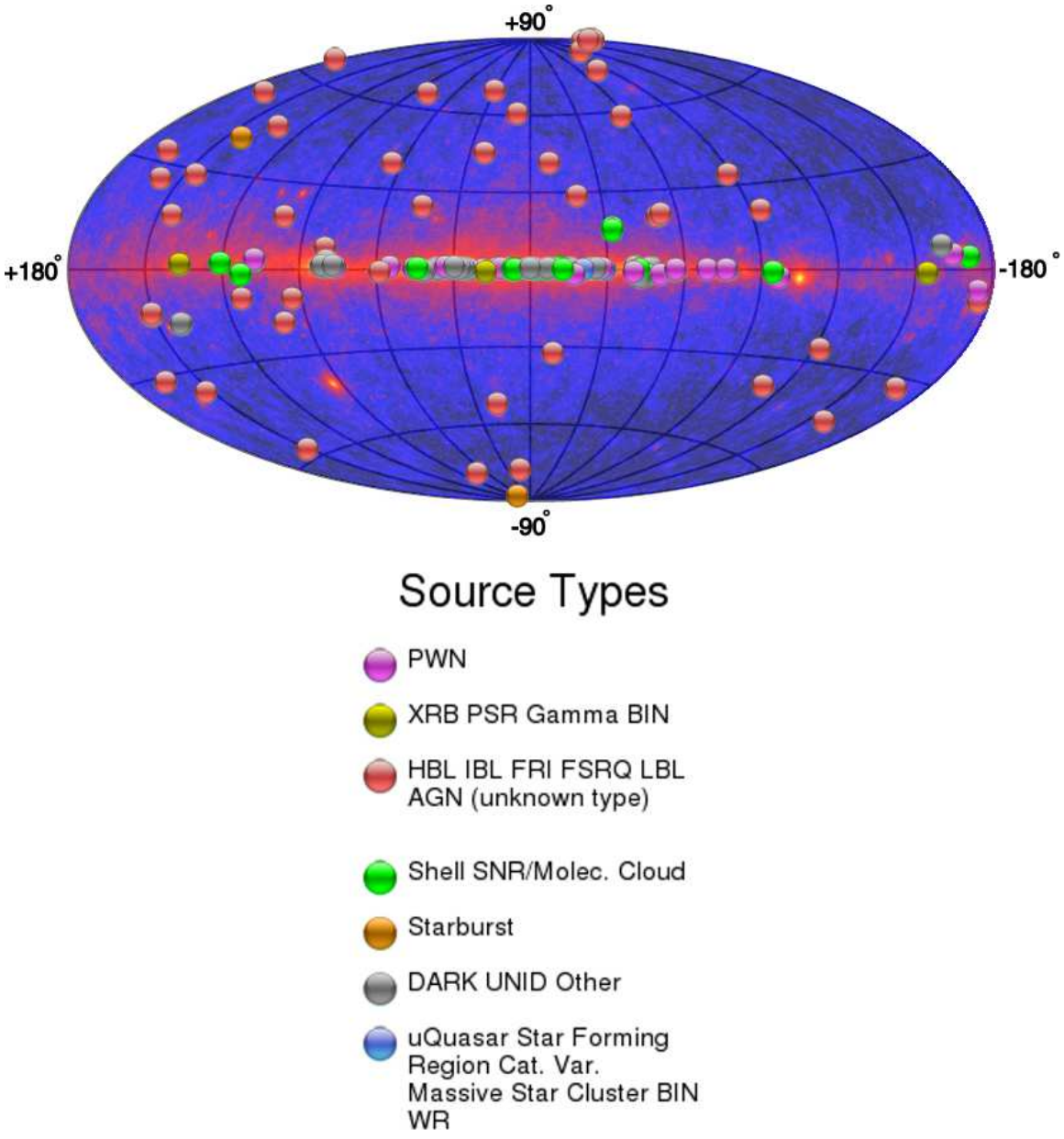

Figure 1.1. An image of the gamma-ray sky in galactic coordinates (reprinted with permission from Wakely & Horan (2008)). The map origin shows the center of our galaxy. The background image is the gamma-ray sky seen by the Fermi Gamma-ray Space Telescope in energy range between MeV and hundreds of GeV. The circles are gamma-ray sources detected in energy range between 100 GeV and tens of TeV by ground-based imaging atmospheric Cherenkov telescopes. The greyed region shows the part of the sky that is observable by the VERITAS telescopes located in southern Arizona, USA. The different source types are listed in the legend on the right: pink is pulsar wind nebula, yellow is X-ray binary, red is active galactic nucleus, green is supernova remnant, orange is starburst galaxy, grey is unidentified, and blue is star cluster.

particles to ultra high energy through Fermi acceleration and is a major source candidate for cosmic-ray acceleration.

X-ray binaries (yellow circles in Figure 1.1) are so called because they are the brightest X-ray sources in the galaxy. They are binary systems of a compact object, such as a black hole or a neutron star, in orbit with a star. Gamma rays may be produced via interaction between the pulsar and the star or via charged particle acceleration by the black hole relativistic jet. Unidentified gamma-ray objects (grey circles in Figure 1.1) are gamma-ray detections with no clear association with known sources at the same location.

1.1.2 Extragalactic objects

Outside of our galaxy, the potential TeV gamma-ray emitters are active galactic nuclei (AGN), starburst galaxies, galaxy clusters, gamma-ray bursts, and dark matter. In contrast to normal galaxies, which mostly emit thermal radiation in optical wavelength, AGN (red circles in Figure 1.1) are more luminous and their emissions extend over the entire electromagnetic spectrum. They are most likely powered by a black hole at the center surrounded by an accretion disk, with collimated jets of relativistic outflow. This type of object is discussed in more detail in the following chapter.

Starburst galaxies have high star formation and supernova rates, up to 10 times more than a normal galaxy. Since cosmic rays are believed to be accelerated by supernovae shockwaves, and gamma rays are expected from the interaction between cosmic ray and the interstellar medium, starburst galaxies are potential gamma-ray emitters. Currently two starburst galaxies have been detected in VHE gamma rays: M82 (VERITAS Collaboration et al., 2009), with a reported VHE flux that is compatible with theoretical models based on cosmic-ray acceleration in starburst galaxies, and NGC 253 (Acero et al., 2009), which suggested the starburst nucleus outshines the rest of the galaxy and implied a higher energy density of cosmic rays than our galaxy.

Gamma-ray burst (GRB) is the brightest phenomenon observed in any wavelength where it is detected. It was discovered in the early 1960s in the MeV energy range by a US satellite designed to monitor the testing of nuclear weapons. The origin and the radiation processes are still debatable, and various temporal structures have been observed within its burst-like behavior. Unfortunately, GRBs have yet to be detected in energy range greater than 100 GeV and only flux upper limits have been reported.

Galaxy clusters are the largest gravitationally bound structures in the Universe. Gamma-ray emission is predicted as a result of proton interactions with the ambient gas, of electron

interactions with the cosmic microwave background photons, or of dark matter annihilation. Currently only upper limits have been established for galaxy clusters in the gamma-ray energy range. Indirect search of dark matter particles can be performed by ground-based gamma-ray telescopes. Gamma-ray photons are expected from the decay or interaction of the weakly interacting massive particles predicted by the extensions of the standard model of particle physics. Dwarf spheroidal galaxies are one of the leading source candidates for the gamma-ray community. These are objects with high dark matter density, located nearby (tens of kiloparsecs), with negligible gamma-ray flux produced by conventional processes other than dark matter particle interaction. Currently only upper limits have been reported from ground-based gamma-ray observations of dwarf spheroidal galaxies.

1.2 Dissertation outline

This dissertation will first continue with the descriptions of AGN and radio galaxies in more depth in Chapter 2, and review the reasons why M 87 is a unique object to study particle acceleration mechanisms and emission processes in relativistic jets.

In Chapter 3, the imaging atmospheric Cherenkov technique is discussed, along with hardware and software information of the VERITAS array.

In Chapter 4 and 5, work on the distant laser calibration system and gamma-ray data analysis technique are presented. The analysis of the Crab Nebula data observed by VERITAS from 2007 to 2010 are also presented to demonstrate the robustness of the VERITAS array and the analysis algorithms used.

In Chapter 6, the results from VERITAS observation of M 87 from 2007 to 2010 are presented in detail, with separate sections dedicated to each flaring episode.

In Chapter 7, the radio, optical, and X-ray observations of M 87 during the multiwavelength campaign with VHE gamma-ray experiments are presented.

In Chapter 8, current models for M 87 and interpretation of the multiwavelength results are presented. A description of other radio galaxies that have been detected in VHE gamma rays is also given.

CHAPTER 2

ACTIVE GALACTIC NUCLEI (AGN)

AGN are galaxies with active nuclei and are very luminous across the entire electromagnetic spectrum, from radio to gamma rays. Unlike a normal galaxy where the majority of the emission is in optical and is of thermal origin. The luminous electromagnetic radiation of an AGN is believed to be generated in a compact volume close to a supermassive black hole with typical mass of $10^{8-9}\,M_{\odot}$(Weekes, 2003).

The AGN category is subdivided by observation characteristics. The first division comes from radio observation. Radio-loud AGN are more luminous in radio than optical emission by more than a factor of 10, and are about 15-20% of the AGN population (Urry & Padovani, 1995). Within the radio-loud AGN, there are blazars with their small viewing angle (essentially looking down the jet) and lack of emission lines, radio quasars with emission lines, and radio galaxies with twin radio-bright lobes.

Within the radio-quiet category, AGN are further divided by emission lines: Seyfert 1 with broad emission lines, Seyfert 2 with narrow emission lines. The difference in emission line widths are due to Doppler broadening from molecules moving around the central object. Then there are the radio-quiet quasars called quasi-stellar objects (QSOs). QSOs are named so because they appear to be galactic stars due to their extreme luminosity and compactness, but measuring their distances via redshifts reveals them as extragalactic in origin.

Figure 2.1 shows a schematic diagram of an AGN, with relativistic jets emerging from the central black hole, which is surrounded by an accretion disk that may be obscured by a dusty torus depending on the viewing angle. The current classification scheme of AGN assumes the different characteristics observed in individual sources are due to geometry, i.e., the angle between the jet and the observer's line of sight, rather than different physics (Urry & Padovani, 1995).

Many AGN are observed to have narrow jets emerging from the center, as illustrated in Figure 2.1. The jets are believed to be collimated by strong magnetic field near the black hole. Particles are accelerated to relativistic speeds in these jets and produce nonthermal

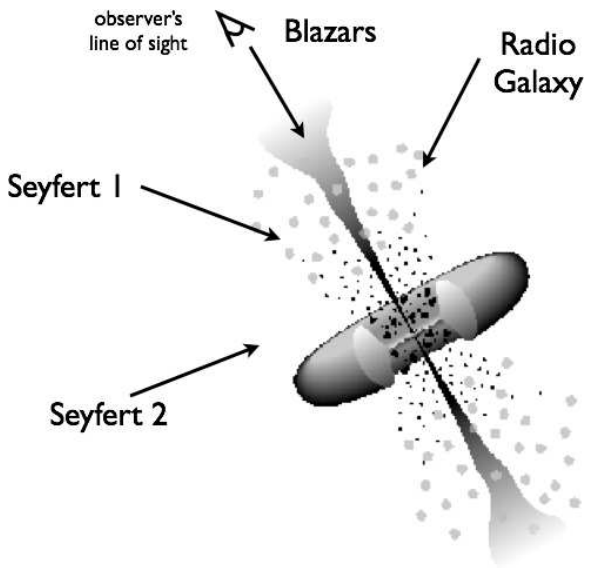

Figure 2.1. Schematic diagram of an active galactic nucleus, with relativistic jets emerging from the central black hole that is surrounded by an accretion disk (adapted from Urry & Padovani (1995)).

radiations across the electromagnetic spectrum. Radio lobes are sometimes observed near the end of jets in these radio-loud AGN. Thermal radiation is expected from the accretion disk, with infrared as the dominant radiation from the dusty torus.

The majority of the extragalactic VHE gamma-ray sources are blazars, AGNs with jets aligned along the line of sight to us. Superluminal motion has been observed in these jets. The apparent speed of the jet structures is greater than the speed of light due to Doppler boosting and the observed transverse velocity is related to the angle along the line of sight θ and the true velocity (see Figure 2.2 for diagram):

$$\begin{aligned} \Delta t_{obs} &= \Delta t - v\Delta t\cos\theta/c \\ v_{obs} &= \frac{v\Delta t\sin\theta}{\Delta t_{obs}} \\ \beta_{obs} &= v_{obs}/c \\ \beta &= v/c \\ \beta_{obs} &= \frac{\beta\sin\theta}{1-\beta\cos\theta} \end{aligned} \tag{2.1}$$

Hence for $\theta \sim 0$, $\beta \sim 1$ and $\beta_{obs} > 1$.

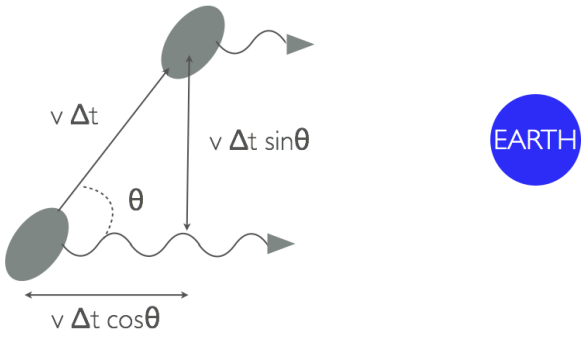

Figure 2.2. Diagram of perceived superluminal motion. A cartoon picture of an emitting blob traveling at an angle θ towards us (Earth). See equation 2.1 for derivation of observed superluminal speed.

The relativistic Doppler factor δ is given by:

$$\delta = \frac{1}{\gamma(1 - \beta\cos\theta)} \qquad \gamma = (1 - \beta^2)^{-1/2} \tag{2.2}$$

The observed luminosity is enhanced by factors of δ depending on the spectral index of the emission and the geometrical assumption of the emitting object. Relativistic beaming allows the gamma-ray photons to escape before being absorbed through photon-photon pair production, apparent superluminal motion in the emitting source, enhanced flux and shortened time variability due to special relativity effect.

The majority of VHE gamma-ray extragalactic objects are BL Lacertae (BL Lac) objects, blazars with no emission lines. The first two TeV extragalactic source discoveries, Markarian (Mrk) 421 (Punch et al., 1992) and Markarian 501 (Quinn et al., 1996), belong in this subclassification of AGN. They are observed to have variable flux and spectra, with a time scale as short as minutes in some flares (e.g., Galante & the VERITAS Collaboration, 2011; Acciari et al., 2011b; Abdo et al., 2011b, and references therein). The flaring timescale provides constraints on the size of the gamma-ray emission region.

Spectral energy distribution (SED) can be obtained from multiwavelength observations and helps constrain the environmental parameters in the emission modelling work. The VHE gamma-ray flux of Mrk 421 is observed to correlate with X-ray, which suggests both emissions originate from the same region and same population of charged particles. However, flaring activity in X-ray with no corresponding strong TeV gamma-ray activity and vice

versa, termed orphan flares, are also observed. The observed broadband spectral energy distribution (SED) of BL Lac objects can be described by standard one-zone synchrotron self-Compton model, where the double-peaked feature of SED can be explained by the synchrotron radiation of relativistic electrons and the inverse Compton emission of the same population of electrons and photons (Acciari et al., 2011a). The modelling work done by Acciari et al. (2011b) requires a large relativistic Doppler factor δ to describe the observed SED and rapid flux variability.

Gamma-ray photons are subjected to interaction with other photons and undergo pair production and create a pair of electron/positron. Due to this photon-photon interaction, the visibility range of VHE gamma rays is limited to a redshift z$\sim$1, or on the order of 10^9 parsecs (pc) (Aharonian, 2004). For spectral studies of distant objects, absorption correction must be done by assuming an extragalactic background radiation model in order to study the intrinsic source spectra.

2.1 Radio galaxies

AGNs with nonthermal radio emission and radio jets extending from the central black hole are called radio galaxies. The nonthermal radio emission is synchrotron emission of charged particles moving through the magnetic field of the AGN. Fanaroff & Riley (1974) gave two classifications to these extragalactic radio sources based on their morphology. Class I represents galaxies with bright radio emission close to the center of the galaxy while class II represents galaxies with peak radio emissions further away. From the subset of the Third Cambridge Catalogue of Radio Sources (3CR) that (Fanaroff & Riley, 1974) sampled, a luminosity threshold of $\approx 2 \times 10^{25}\,\mathrm{WHz^{-1}sr^{-1}}$ at 178 MHz is observed to distinguish class I and class II galaxies from each other. According to the unification scheme (Urry & Padovani, 1995), FR I radio galaxies are likely misaligned BL Lac objects. If this is indeed true, then multiwavelength observation of radio galaxies can help constrain the location of VHE emissions within the jet, which is not resolved by current VHE instruments.

Currently there are 4 radio galaxies detected in VHE gamma rays: M 87, Centaurus A, NGC 1275, and IC 310. This work focuses on the VHE gamma-ray observation of M 87 using the VERITAS array with a brief description of the other three radio galaxies since Centaurus A is not visible to the VERITAS telescopes, while NGC 1275 and IC 310 are not yet detected by VERITAS.

2.1.1 M 87

M 87 is the 87th object in the Messier catalogue published by Charles Messier in 1781. It is an FR I radio galaxy near the center of the Virgo cluster at right ascension (RA) $12^h30^m49.4^s$ and declination (δ)$12°23'28''$ (J2000). Its distance, obtained from the ACS Virgo Cluster Survey, is 16.7 ± 0.2 Mpc (Mei et al., 2007), making M 87 as one of the closest extragalactic objects observed in VHE gamma rays at a redshift of 0.0044 (Wakely & Horan, 2008). The distance quoted from Mei et al. (2007) is determined by the surface brightness fluctuations method, which measures the variance of a galaxy's surface brightness and is related to the galaxy's distance as a function of stellar population age and metallicity.

The core of M 87 is believed to be powered by a supermassive black hole of mass $(6.6 \pm 0.4) \times 10^9$ $M_\odot$ assuming a distance of 17.9 Mpc (Gebhardt et al., 2011). The black hole mass, derived from stellar kinematic data, scales linearly with the assumed distance as stated by Gebhardt et al. (2011). Using the distance assumption of 16.7 Mpc, the corrected black hole mass is $(6.0 \pm 0.5) \times 10^9$ $M_\odot$. This difference in mass does not impact the interpretation of VHE gamma-ray observations significantly.

The jet of M 87 is misaligned along the line of sight and is the first ever observed plasma jet (Curtis, 1918). This jet misalignment, coupled with the proximity of M 87, allows for high resolution studies of M 87 jet structures in different wavebands. The morphology of the M 87 jet is well studied in radio (e.g., Biretta et al., 1995; Ly et al., 2007; Kovalev et al., 2007; Cheung et al., 2007), optical (e.g., Biretta et al., 1999; Perlman et al., 2003), infrared (e.g., Perlman et al., 2001), and X-ray (e.g., Marshall et al., 2002; Wilson & Yang, 2002; Perlman & Wilson, 2005; Harris et al., 2009). The M 87 jet is 2 kilo-parsecs (pc) long (Owen et al., 2000). There are multiple jet features termed "knots" in the M 87 jet (see Figure 2.3) seen in radio, optical and X-ray. Bicknell & Begelman (1996); Perlman & Wilson (2005) suggested that the formation of these knots are due to instabilities in the jet outflow, which then result in formation of shocks in the jet. The jet morphology is similar in these wavebands, but displacements and brightness variations are seen in several knots in X-ray when compared to their radio/optical counterparts (Wilson & Yang, 2002; Perlman & Wilson, 2005). The closest feature to the nucleus is the knot HST-1, which is 0.86" (70 pc, projected) away. Further away, there are several knots ranging from 3" to 20" (240 to 1600 pc, projected) from the nucleus with knot D and A being the most luminous in X-ray among these knots. Wilson & Yang (2002); Harris et al. (2003, 2006) proposed that leptonic synchrotron radiation as the most likely process for the nonthermal emission

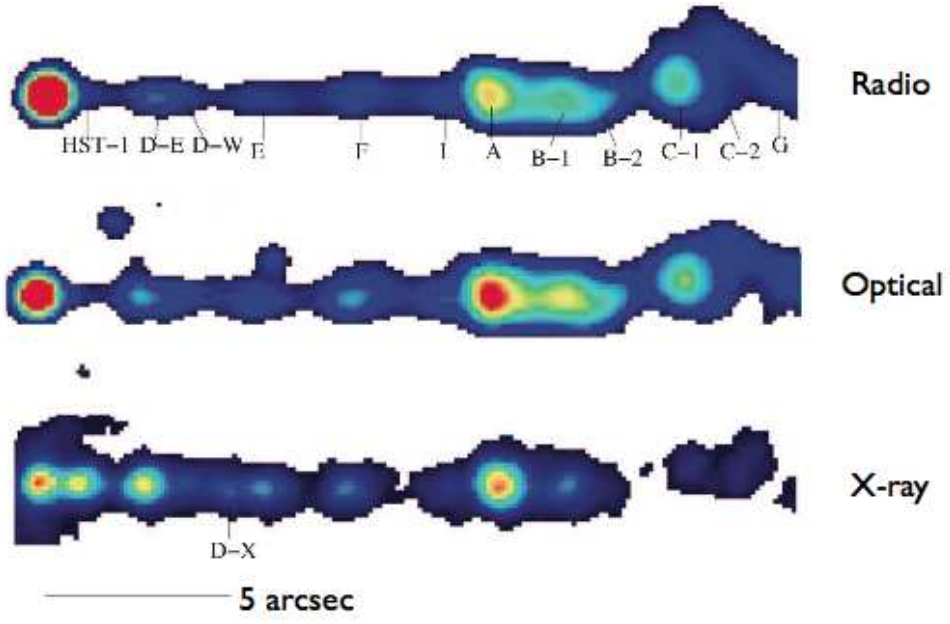

Figure 2.3. Image of M 87 jet (Perlman & Wilson, 2005) (reproduced by permission of the AAS). *Top panel*: Radio (VLA 15 GHz). *Second panel*: Optical (HST). *Bottom panel*: X-ray (Chandra).

associated with the jet based on the observed spectra of the various knots. Tsvetanov et al. (1998) suggested M 87 is a misaligned BL Lac object due to the observed featureless power-law continuum spectrum with spectral index typical of BL Lac objects. Unlike a typical BL Lacs, M 87 nucleus is faint due to the large angle between the jet axis and the line of sight and would not have been detected as a BL Lac if it were further away.

Despite the misalignment of the jet axis along the line of sight, apparent superluminal motion has been reported for different jet features and the jet angle can be constrained from the observed speed in the relativistic jet model. In radio, Biretta et al. (1995) deduced the line of sight angle $\approx 43^\circ$ using superluminal speed observed in knot D and the presence of a narrow linear feature in knot A; Cheung et al. (2007) observed multiple unresolved components within the knot HST-1 and constrains the jet angle at the location of the knot HST-1 less than $26^\circ \pm 4^\circ$. In optical, Biretta et al. (1999) constrains the jet angle to less than 19° along the line of sight using the largest apparent speeds observed within the knot

HST-1.

Flux variability has been observed in radio, optical, and X-ray in the nucleus and the knot HST-1. In radio, Chang et al. (2010) reported flaring activities from the nucleus in 2008 and the knot HST-1 in 2005. In the optical, Biretta et al. (1999) reported year-scale changes in the brightness of the knot HST-1. Perlman et al. (2003) reported month-scale flux variability in the nucleus and the knot HST-1 in both optical and X-ray. Harris et al. (2003) also reported X-ray month-scale variability in the nucleus and the knot HST-1. The observed time scales of these flares help constrain the modelling parameters for the M 87 jet environment (e.g., Harris et al., 2009).

Little evidence is found for thermal emission in infrared from the dusty torus of M 87 (Perlman et al., 2001). This suggests gamma-ray interaction with IR photons should be negligible. Bai & Lee (2001) suggested gamma-ray emission should be detectable for nearby FR I radio galaxies such as Centaurus A and M 87 according to the unified scheme of BL Lac objects. FR I radio galaxies should exhibit similar double-peaked structure in the spectral energy distribution as BL Lac objects. The double-peaked structure is likely due to synchrotron and inverse Compton emissions. Since the nonthermal X-ray emissions observed from M 87 are most likely associated with synchrotron radiation, Bai & Lee (2001) predicted the M 87 Compton emission peak at ~ 0.1 TeV. The following chapters describe how gamma rays are observed from ground-based telescopes, before going into details of the VHE gamma-ray observations of M 87 and their implications.

CHAPTER 3

IMAGING ATMOSPHERIC CHERENKOV TECHNIQUE

Gamma rays above a few MeV cannot be gathered and focused via reflection or refraction because the photons will interact with the reflecting/refracting material and will lose their energies or be completely absorbed. Therefore the collection area of a gamma-ray telescope in space is limited by the actual detector's size. Since gamma-ray emission is nonthermal, it follows a power-law distribution in which the flux decreases by order of magnitude that is equivalent to the power law index as energy increases. At over 100 GeV, the gamma-ray flux from an object is so low that it is impractical to observe VHE gamma rays from space.

In 1948, Blackett suggested Cherenkov radiation produced by cosmic-ray particles travelling through the atmosphere should make up $\sim 10^{-4}$ of the night sky background (Jelley, 1958). An extensive air shower (detailed in the next section) triggered by a cosmic ray generates a large number of particles which in turn produce a burst of Cherenkov light that is much more intense than the night sky background. Galbraith & Jelley (1953) confirmed that the Cherenkov light pulses from the night sky are related to cosmic-ray showers using a set of mirrors, photomultipliers, and Geiger counters. This led to the development of a series of ground-based array to detect atmospheric Cherenkov radiation initiated by gamma rays in the following years (Weekes, 2003).

However, advancement of ground-based gamma-ray astronomy was hampered by the overwhelming background of cosmic rays. It was not until the discovery of steady gamma-ray emission from the Crab Nebula at 9.0 standard deviations above the cosmic-ray background by the Whipple telescope in 1989 (Weekes et al., 1989) that the atmospheric Cherenkov technique was demonstrated as a reliable way to detect gamma rays from astronomical objects.

3.1 Extensive air shower

Even though the atmosphere is opaque to electromagnetic radiation above 10 eV, cosmic radiations at higher energies can still be observed via secondary products from interactions with the atmosphere. The Earth's atmosphere has a vertical thickness of $1030\,\mathrm{g\,cm^{-2}}$ above sea level which is approximately 28 radiation lengths (Weekes, 2003). One radiation length is the distance over which an electron loses all but 1/e of its energy via Bremsstrahlung radiation, or 7/9 of the mean free path for pair production from a high energy photon.

3.1.1 Gamma-ray shower

For photons above 10 MeV, the dominant interaction with matter is via pair production (Das & Ferbel, 2004), where a photon above 1.022 MeV (equivalent to the mass of an electron and a positron) can create an electron-positron pair. The pair production cross section scales as the square of the atomic number of the medium (Z^2), but at very high energy ($> 100\,\mathrm{MeV}$), the cross section can be characterized by a constant mean free path equivalent to the radiation length of electron. A radiation length is the distance at which an electron loses all but 1/e of its energy via bremsstrahlung.

The resultant electron-positron pair then loses energy via ionization and Bremsstrahlung (see Figure 3.1). When a charged particle is accelerated by the electric field of an atom and changes its trajectory, a photon with the energy difference between the initial and final energy of the charged particle is emitted. This is called Bremsstrahlung radiation.

When a gamma ray hits the top of the Earth's atmosphere, it initiates a particle shower (see Figure 3.2) by first creating an electron-positron pair, which then creates secondary gamma rays via Bremsstrahlung. This cycle of pair production and Bremsstrahlung radiation continues until the average energy of the charged particles drops off to $\sim 80\,\mathrm{MeV}$

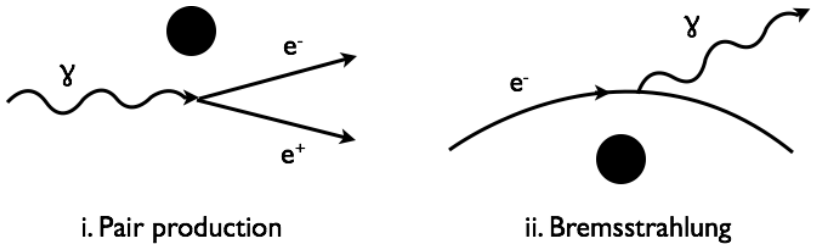

Figure 3.1. Particle interaction in matter: i) Pair production. ii) Bremsstrahlung.

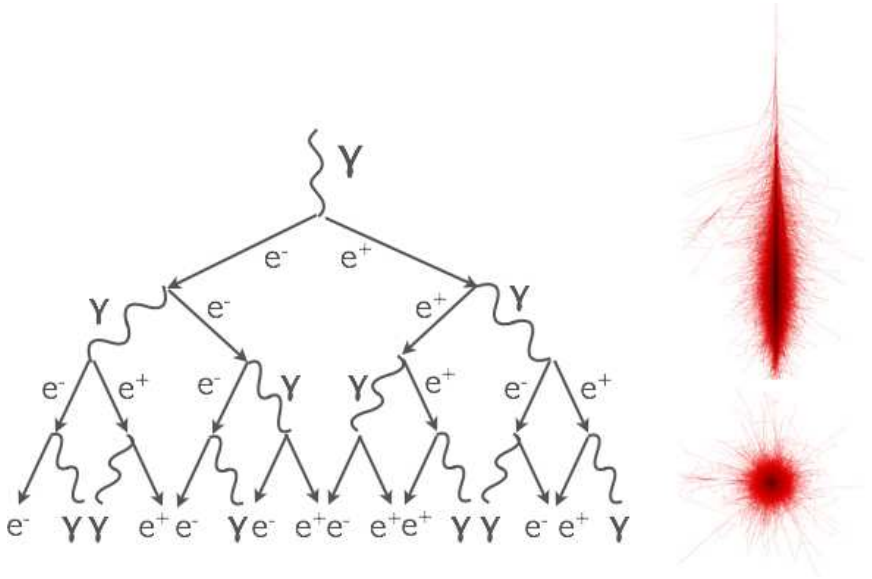

Figure 3.2. Development of a gamma-ray induced air shower. *Left:* Schematic of a gamma-ray shower development in a simplified view. *Right:* CORSIKA shower image of a 1 TeV photon, longitudinal and ground projections (reprinted with permission from Schmidt (2011)).

where ionization process begins to dominate and the number of electrons energetic enough to produce secondaries decreases. At this point the shower cascade reaches its maximum (shower maximum). The location of the shower maximum is dependent on the primary energy of the gamma ray as the number of interactions before shower maximum depends on the initial energy of the incoming gamma ray (Weekes, 2003).

3.1.2 Hadronic shower

When a cosmic-ray nucleus collides with a nucleus from the Earth's atmosphere, pions (π^0, π^+, and π^-) are produced with large transverse momentum (see Figure 3.3). This is one of the characteristics to distinguish gamma-ray induced versus cosmic-ray induced shower cascades. π^0, with a mean lifetime of the order of 10^{-16} s promptly decays into two gamma rays, which in turn initiates corresponding gamma-ray shower cascades. π^+ and π^- have a mean lifetime of 10^{-8} s and decay into muons. These muons then either decay into electrons/positrons and neutrinos, or remain intact and arrive to the ground (Longair, 2004). Since these muons can penetrate through the atmosphere, the Cherenkov

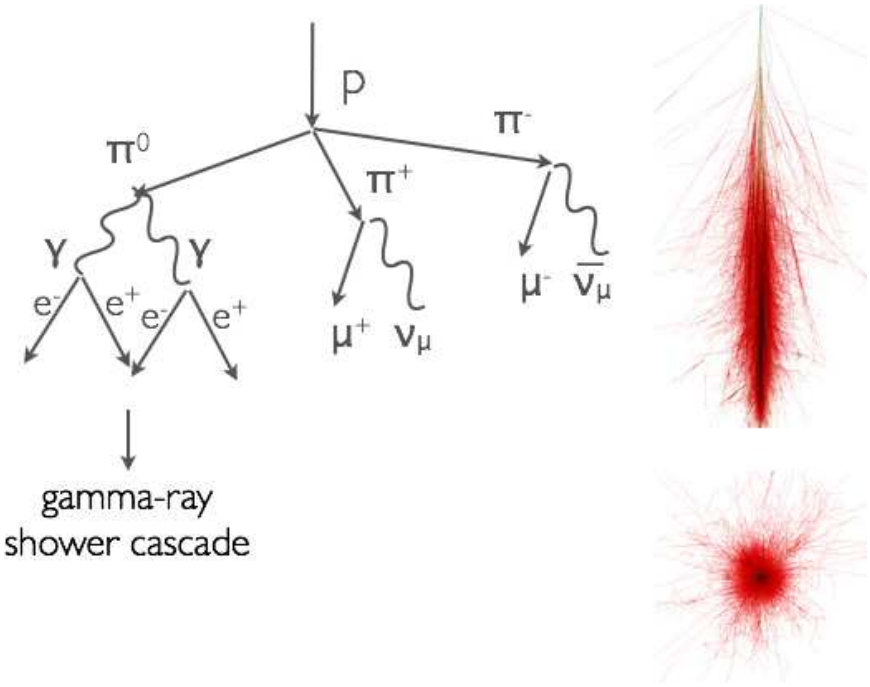

Figure 3.3. Development of a cosmic-ray induced air shower. *Left:* Schematic of a cosmic-ray shower development in a simplified view. *Right:* CORSIKA shower image of a 1 TeV proton, longitudinal and ground projections (reprinted with permission from Schmidt (2011)).

light from these muons arrives earlier than the Cherenkov light produced by the secondary gamma-ray shower cascade. The time spread of the Cherenkov light pulse is longer than one originally initiated by a gamma ray as a result. However the Cherenkov image parameters such as length and width are distinguishable enough between a gamma-ray cascade image and a cosmic-ray cascade image that the timing information does not provide additional discrimination in the analysis.

3.2 Cherenkov radiation

When a charged particle travels slowly through a dielectric medium, it temporarily polarizes the surrounding atoms as it is passing through. The resultant polarization is symmetric around the temporary position of the charged particle and no radiation is emitted. If however the charged particle is travelling faster than the speed of light in the dielectric medium, the resultant dipole field is asymmetric along the direction of the

charged particle track. The wavefronts produced by this field adds up coherently and form a cone wave at an angle θ_c from the particle direction of propagation (Jelley, 1958). This phenomenon is first observed by P. A. Cherenkov in 1934.

The Cherenkov angle θ_c is derived from the geometry of Figure 3.4:

$$cos\,\theta_c = \frac{c}{nv} \tag{3.1}$$

where n is the refractive index of the medium and v is the particle's velocity.

The energy threshold for Cherenkov radiation is dependent on the refractive index of the medium. Since the particle velocity is required to be greater than c/n to produce Cherenkov radiation, the Lorentz factor can be rewritten as:

$$\gamma \geq (1 - \frac{v^2}{c^2})^{-1/2} \geq (1 - \frac{1}{n^2})^{-1/2}$$

For example, at sea level in standard atmosphere, the refractive index of air is ($n = 1.0003$), the energy threshold for Cherenkov radiation by an electron is then $E = \gamma mc^2 = 21\,\mathrm{MeV}$, and the Cherenkov angle θ_c is 1.3° (from equation 3.1) (Longair, 2004).

The radiation output derived by Frank and Tamm in 1937 imposes no cut-off in frequency (Jelley, 1958). In reality however, Cherenkov radiation is restricted due to the dispersion of the medium. In X-rays the index of refraction is less than or equal to 1 depending on the medium. Therefore no Cherenkov radiation is in the X-ray waveband. The infrared waveband is mostly absorbed and scattered in the atmosphere, but the near ultraviolet and visible wavebands are transmitted in the atmosphere.

The main scattering processes in the atmosphere are Rayleigh and Mie scattering. Rayleigh scattering is the elastic scattering of light by particles much smaller than the wavelength of the light. The incoming photon interacts with the particle and induces a dipole moment. The resultant dipole radiation has a different angular distribution but the

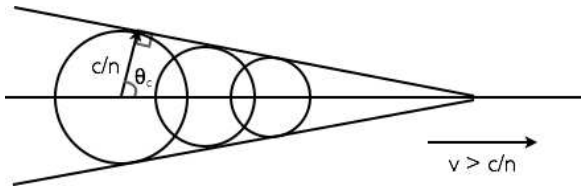

Figure 3.4. Huygens' construction of the Cherenkov wavefront.

energy of the exit photon remains the same as the initial photon. This is explored further in Chapter 4 *Distant Laser* where we measure the Rayleigh scattered light from a laser and compare it to simulation. For particles bigger than the wavelength of the light, it is described by Mie scattering, which is a solution to the Maxwell's equations of scattering by objects such as spheres and cylinders. Since Mie scattering is dependent on the shape and size of the scatterer, the atmospheric composition, including aerosols such as dirt and other impurities which may be time dependent, is needed to accurately predict Mie scattering of the atmosphere. These are taken care of in Monte Carlo simulations of gamma-ray showers, and are used in conjunction with data to accurately analyze Cherenkov images observed by the ground-based telescopes.

The number of Cherenkov photons emitted per unit path per unit wavelength goes as $1/\lambda^2$ (see equation 3.2). The Cherenkov radiation peaks in ultraviolet after including effects from atmospheric absorption and scattering processes.

$$\frac{dN^2}{dl\,d\lambda} = \frac{2\pi\alpha z^2}{\lambda^2}(1 - \frac{1}{\beta^2 n^2(\lambda)}) \tag{3.2}$$

The charged particles produced from VHE gamma-ray shower cascade are energetic enough to be travelling faster than the speed of light in the medium and produce Cherenkov radiation, which allows us to observe VHE gamma-ray sources from the ground. As the charged particles travel through the atmosphere, the index of refraction increases as the charged particles get closer to the ground. Combining with multiple Coulomb scattering of the charged particles, this results in a focusing effect of a blurred Cherenkov ring with radius $\sim 120\,\mathrm{m}$. For more details on the lateral and longitudinal distributions of the Cherenkov light from gamma-ray induced showers, see Hillas (1982a,b), or the gamma-ray astrophysics review by Aharonian et al. (2008).

The VERITAS array has four telescopes situated approximately 100 m apart from each other at the corners of a parallelogram to maximize the detection area while maintaining multitelescope coincidence in detecting the Cherenkov radiation. The VERITAS array is described in more details in the following section.

3.3 The VERITAS array

The Very Energetic Radiation Imaging Telescope Array System (VERITAS) is an array of four 12 m diameter reflector telescopes situated at the Fred Lawrence Whipple Observatory on Mount Hopkins near Tucson, Arizona. The array is sensitive from $\sim 100\,\mathrm{GeV}$ to more than 30 TeV gamma rays. The angular resolution of the array is 0.1° at 1 TeV (68%

containment). VERITAS can detect a 1% Crab Nebula flux source at 5 standard deviations (σ) above the night sky background in less than 30 hours using the common VERITAS data analysis and under the current layout as shown in Figure 3.5. Prior to the summer of 2009, the array layout was asymmetric and requires about 50 hours for a $5\,\sigma$ detection of a 1% Crab Nebula flux source. Detailed technical information of the array is presented in Holder et al. (2006) and Perkins et al. (2009). The $5\,\sigma$ detection criterion arises from multiple $3\,\sigma$ detection claims before the firm establishment of the ground-based gamma-ray astronomy field. Those $3\,\sigma$ results are questionable due to the lack of careful treatment of systematics of the hardware and analysis software. To avoid having disputable detections, the criterion is raised to $5\,\sigma$ where even with a lack of understanding of systematics, a $5\,\sigma$ result is unlikely due to background noise.

Each telescope has a total mirror area of $\sim 110\,\mathrm{m}^2$, with peak reflectivity at 320 nm

Figure 3.5. Aerial view of the VERITAS array on Mount Hopkins, Arizona. Top left insert shows a closeup picture of the 3.5° FOV camera on each telescope.

exceeding 90 %. Each telescope camera has 499 photomultiplier tubes (PMT) arranged in a hexagonal lattice covering a field of view (FOV) of 3.5° (see insert in Figure 3.5). The PMTs are read out via a 500 MHz flash-ADC (FADC) system.

3.3.1 Triggering system

There are 3 levels of triggering systems for an event to be recorded by the telescope array data acquisition system. The first level (L1) involves individual PMTs of each telescope; if a PMT output is above a preset threshold, it passes the L1 trigger. The threshold is determined by looking at the night sky background and cosmic-ray trigger rates (see Figure 3.6). This threshold is checked monthly and updated accordingly; the current threshold is

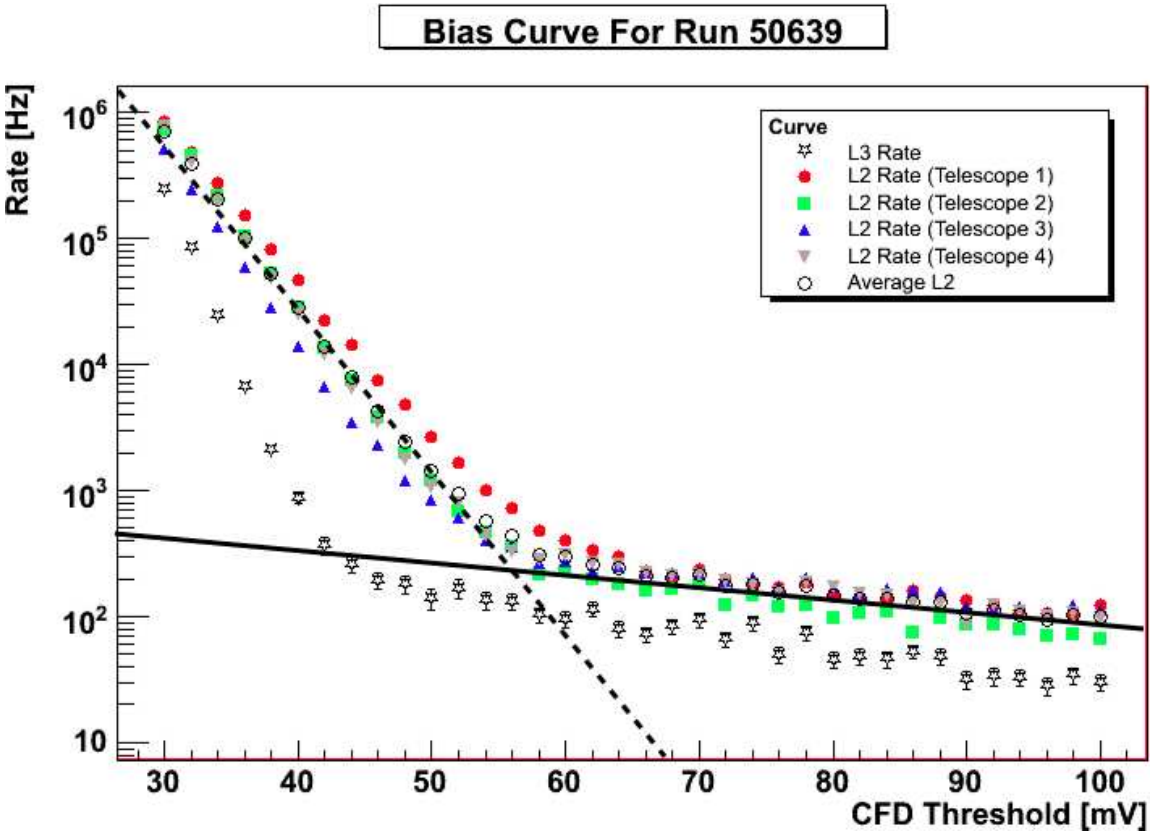

Figure 3.6. Trigger rate as a function of PMT trigger threshold (CFD threshold). The dashed line indicates the night sky background, the solid line represents the Cherenkov radiation.

50 mV. The second level (L2) trigger involves the individual camera; if three neighboring PMTs pass the L1 trigger, the event is flagged and passes on to the third level (L3) trigger. The L3 trigger involves the entire array of telescopes; if there are at least two telescopes triggering the L2 within 50 ns, then the event is flagged as a possible gamma-ray event and is recorded. See Figure 3.7 for an example of an event passing all three triggers.

3.3.2 Calibration techniques

Calibration of the VERITAS telescopes is done via measurements of individual elements (Hanna, 2008). Routinely the mirrors and PMTs of the telescopes are replaced to maintain steady performance in overall mirror reflectivity and quantum efficiency of the PMTs. Batches of mirrors and PMTs remain in the laboratory for testing to ensure they are up to specification and to provide detailed measurement of reflectivity and efficiency vital to the analysis of VERITAS data. In addition, a nitrogen laser with 3.5 ns pulse width at 337 nm is used to calibrate the performance each telescope camera. The laser provides uniform flashes

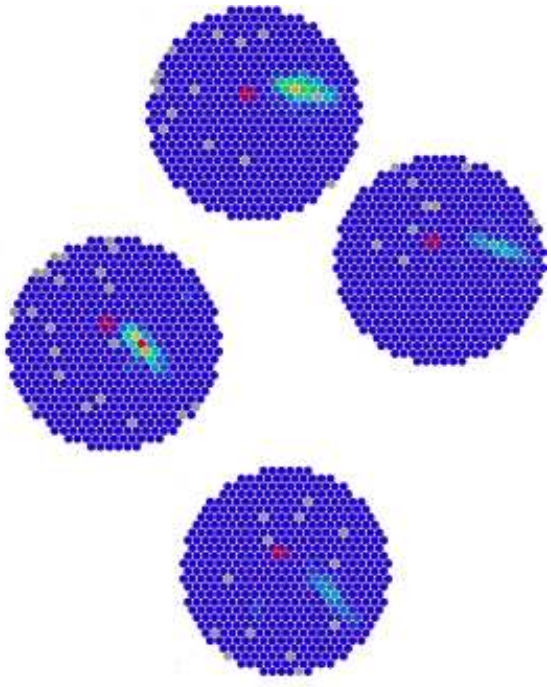

Figure 3.7. An example of an event passing all three triggers, where there are more than two camera images with three neighboring pixels above CFD threshold.

of light to each camera via optical fibers and diffusers. At the beginning of each observation night, a 5-minute laser run is taken to record the response of each individual PMT for each camera such that individual PMT gains and timing information can be determined to compensate for a uniform performance across the entire camera. These laser data are then incorporated into the analysis for the data taken in the same night.

A second identical laser has been used to explore the possibility of absolute calibration of the telescopes. The details are described in the following chapter *Distant laser* (Chapter 4).

CHAPTER 4

DISTANT LASER

A more direct approach for calibration of the telescopes using a known light source was first proposed and tested by Shepherd et al. (2005), inspired by ultra high energy cosmic-ray experiments. Using the scattered light from a calibrated laser pulse, the detector response from the telescopes can be compared to simulation to determine the efficiency and properties of each detector.

As a laser shot travels upward through the atmosphere, the laser light is attenuated via Rayleigh and Mie scattering from the particles in the atmosphere. In Rayleigh scattering, the incident photon polarizes the molecules, creating a dipole. The resultant dipole radiation has the same frequency as the incident photon but the propagation direction is redistributed. The angular distribution of the Rayleigh scattered light is described by the phase function

$$P_{Ray}(\theta) = \frac{3}{4}(1 + cos^2\theta) \tag{4.1}$$

where θ is the angle between the original propagation direction and the scattered direction. The phase function is defined as the ratio of energy scattered per unit solid angle in θ to the average energy scattered per unit solid angle in all directions, and the integral of the phase function is normalized to 1 (McCartney, 1976).

The Mie scattering theory is the solution of Maxwell equations for interaction between an electromagnetic wave and a spherical particle. The angular distribution is not in a general analytical form but can be approximated as strongly beamed in the forward direction with minimum at 90° angle with respect to the original propagation direction. Mie scattering is dependent on the size and shape of the scatterers, which are usually approximated since the actual distribution of aerosols is, in general, not known. Additional development in scattering by nonspherical particles can be found in van de Hulst (1957) and Kerker (1969), but are beyond the scope of this work.

Rayleigh scattering can be simulated accurately while Mie scattering, due to its dependence on the aerosol conditions and properties, is usually estimated. Since aerosol layer

is typically close to the ground due to its makeup of larger/heavier molecules, multiple measurements over a range of altitudes throughout the observing season are necessary to monitor atmospheric changes and to monitor the telescopes performances by looking above the aerosol layer. If the telescopes are pointing at high elevation (the highest line in Figure 4.1), Rayleigh scattering would dominate after attenuation from the aerosol layer. If the telescopes are pointed at lower elevation, the scattered laser light would have gone through a longer distance in the aerosol layer and attenuated more via Mie scattering than at the higher elevation.

4.1 Laser setup and data acquisition

A 300 μJ nitrogen laser with 4 ns pulse width and 337 nm wavelength is mounted on a movable rack with flexible beam collimation and intensity adjustment (see Figure 4.1). The laser is fired pointing at zenith $\sim$ 1.2 km away from the VERITAS telescope array. The array is aimed at a range of elevation from 20° to 60°, which translates to a range of altitude between 0.5 km and 2.2 km. Both the laser and the array of telescopes are externally triggered by GPS pulsers such that each recorded event contains an image of the laser shot. The FADC (PMT read-out system) recording window is set to 244 samples, or 488 nanoseconds, instead of the normal read-out window of 24 samples. This is to maximize the recording time of the scattered laser light moving across the camera, which has a range of speed from 3.5 to 12.5°/μs depending on the elevation.

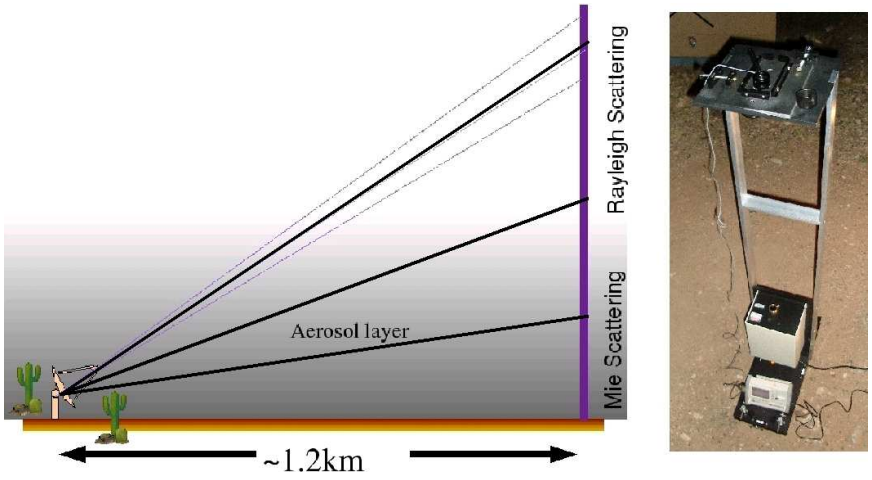

Figure 4.1. Cartoon demonstration of laser setup and a picture of the laser.

The geometry of the distant laser setup is shown in Figure 4.2. As the telescope points higher in elevation, the vertical distance covered within the camera's 3.5° of FOV increases based on the geometry of the setup. Therefore the duration of the laser pulse increases with the elevation of telescope pointing. Figure 4.3 shows the laser pulse recorded by the telescope data acquisition at different elevations. At 20° elevation the pulse width is $\sim$ 30 samples (60 ns) and at 60° elevation the pulse width is $\sim$ 100 samples (200 ns). To alleviate the problem of having fixed window width for data acquisition and the increasing pulse widths, the pixels are configured to read out at different times such that all recorded events from any elevation have a vertical line of triggered pixels spanning the entire camera.

The laser pulse width seen by a pixel, neglecting the intrinsic pulse duration of the laser (4 ns), can be calculated as follows:

$$d\tau = \frac{\theta_p + \phi}{d\theta/dt} \tag{4.2}$$

where θ_p is the angular pixel spacing, ϕ is the angular extent of the telescope as seen by the laser beam, and $d\theta/dt$ is the angular speed of the laser beam, which can be calculated as the following:

$$\begin{aligned} \frac{dt}{d\theta} &= \frac{d}{d\theta}\left(\frac{h+d}{c}\right) \\ h &= D\tan\theta \\ d &= \frac{D}{\cos\theta} \\ \frac{d\theta}{dt} &= \frac{c}{D}\,\frac{\cos^2\theta}{1+\sin\theta} \end{aligned} \tag{4.3}$$

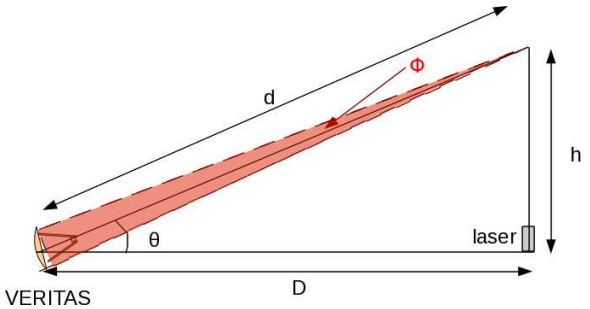

Figure 4.2. Geometry of the distant laser setup. The laser a distance D away from the telescope and the telescope is pointing at θ in elevation. ϕ is the angular extent of the telescope seen by the laser beam.

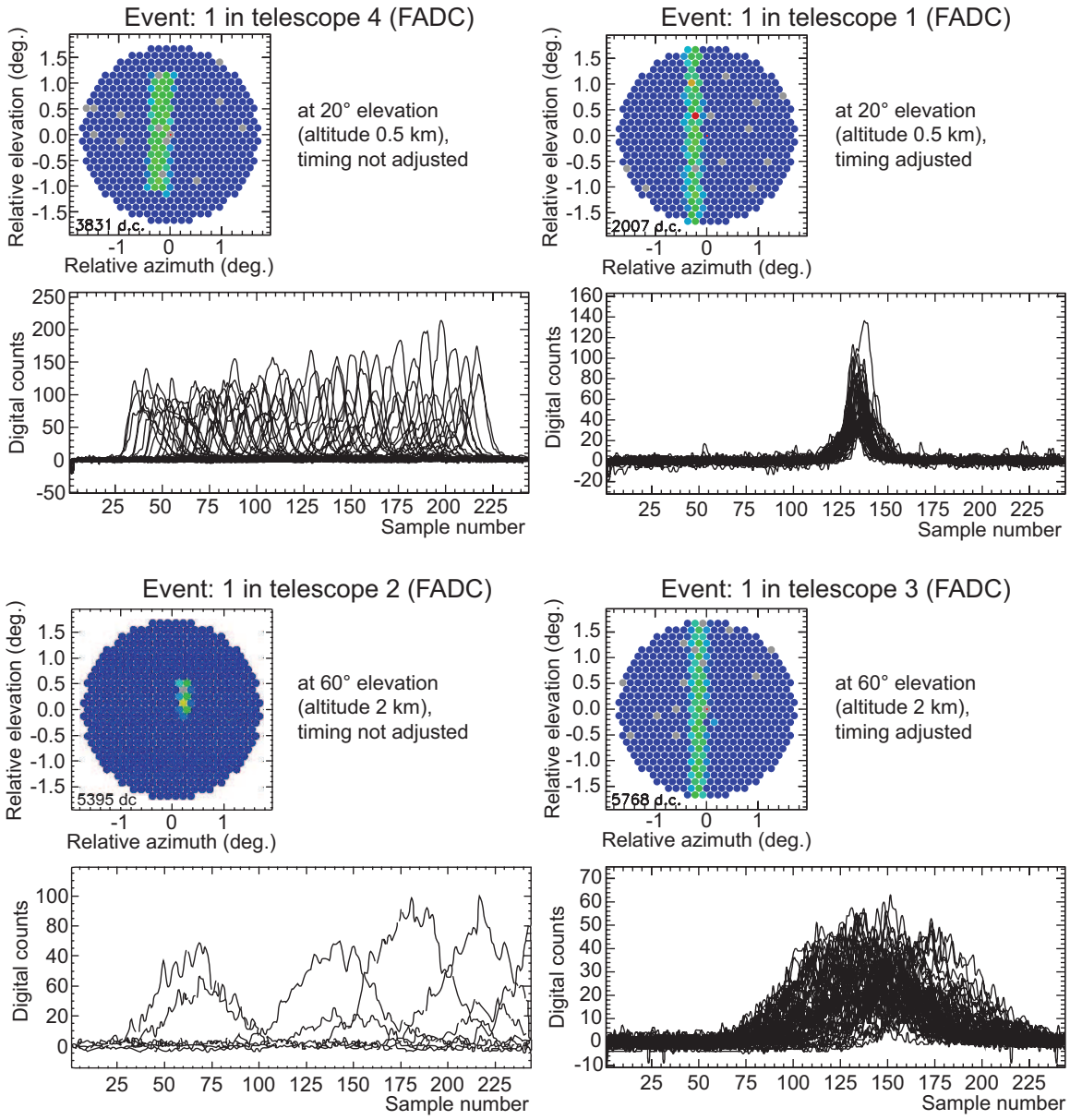

Figure 4.3. Sample FADC traces of a distant laser event at different elevation pointings. At higher elevation, the number of pixels triggered is reduced and the width of the pulse is lengthened due to geometrical effects. With timing adjustments, the scattered laser light can be captured with the entire length of the camera.

For the distant laser setup with the VERITAS telescopes, which are 12 m in diameter and each pixel has an angular size of 0.15°, the pulse width as a function of telescope elevation is expressed in equation 4.4 and shown graphically in Figure 4.4.

$$\begin{aligned} d\tau &= \frac{\theta_p + \phi}{d\theta/dt} \\ &= (0.15^\circ + \frac{12\,\mathrm{m}\,\cos\theta}{D})\frac{D}{c}\,\frac{1+\sin\theta}{\cos^2\theta} \end{aligned} \tag{4.4}$$

This calculation agrees with what has been observed in the data and is used as a reference to determine how high in elevation and how far the laser can be for the distant laser test.

4.2 Analysis and simulation

4.2.1 Analysis algorithm

The laser analysis algorithm is modified from the regular data analysis described in the following chapter *Analysis Technique* (Chapter 5). The FADC trace is convolved with a fixed 125-sample wide window (250 ns equivalent). The location of the integration window is determined by going through all possible integration and finding the maximum signal. If the true integration window falls outside of the FADC trace (see bottom panel of Figure 4.5 for example), the trace is considered truncated and discarded from the analysis. If the trace passed the integration window check, the background to be subtracted from the integrated

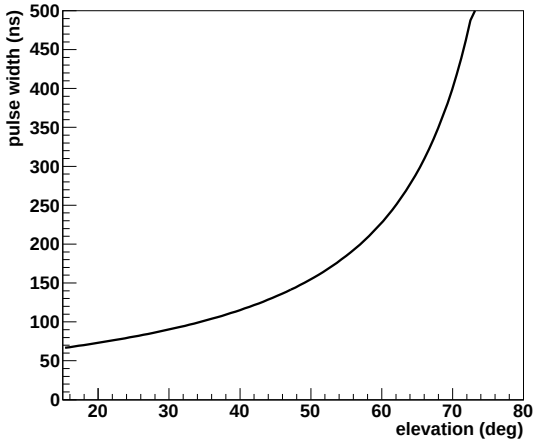

Figure 4.4. FADC signal pulse width as a function of telescope elevation pointing; laser is situated at 1200 m away.

sum is estimated by averaging the signal outside the integration window. This background signal is also normalized to the width of the integration window since the background would be 119-sample wide compared to the 125-sample integration window.

4.2.2 Simulation

The Rayleigh scattering simulation written by N. Shepherd follows closely the work of Bucholtz (1995), which calculated Rayleigh scattering cross sections and optical depths for 1962 U.S. Standard Atmosphere. In the 1962 U.S. Standard Atmosphere at sea level, the molecular number density $N_s = 2.54743 \times 10^{25}\,\mathrm{m}^{-3}$, temperature $T_s = 15^\circ\,\mathrm{C}$, and pressure $P_s = 1013.25\,\mathrm{mbars}$. The standard air index of refraction n_s is calculated by Peck & Reeder (1972):

$$(n_s - 1) \times 10^8 = \frac{5791817}{238.0185 - \lambda^{-2}} + \frac{167909}{57.362 - \lambda^{-2}} \tag{4.5}$$

For the laser light wavelength 337 nm, the index of refraction $n_s = 1.00287$ assuming standard atmosphere at sea level.

The total Rayleigh scattering cross section is given by

$$\sigma_{Ray} = \frac{24\pi^3}{\lambda^4 N_s^2}\left(\frac{n_s^2 - 1}{n_s^2 + 2}\right)^2 \frac{6 + 3\rho}{6 - 7\rho} \tag{4.6}$$

where λ is the wavelength and ρ is the depolarization factor which accounts for air molecule anisotropy since an air molecule is not isotropically spherical particles.

The extinction coefficient due to Rayleigh scattering, assuming an ideal gas, is then calculated as follows:

$$\begin{aligned} \beta(P,T) &= \sigma_{Ray} N(z) \\ &= \sigma_{Ray} \frac{P(z)}{T(z)} \frac{T_s}{P_s} N_s \end{aligned} \tag{4.7}$$

The temperature is approximated as a linear function of altitude (z) since the laser measurements are within the first few kilometers of the atmosphere above ground. $T(z) = T_0 + az$ where T_0 is the ground temperature and a is a constant temperature gradient which is 9 K/km. The pressure, as a function of altitude, is computed using the ideal gas law $P(z)V = N(z)kT(z)$.

Instead of the typical formula (equation 4.1) to describe the angular distribution of Rayleigh scattered light, a more accurate formula for the phase function given by Chandrasekhar which accounts for molecular anisotropy (Bucholtz, 1995) is used in our simulation

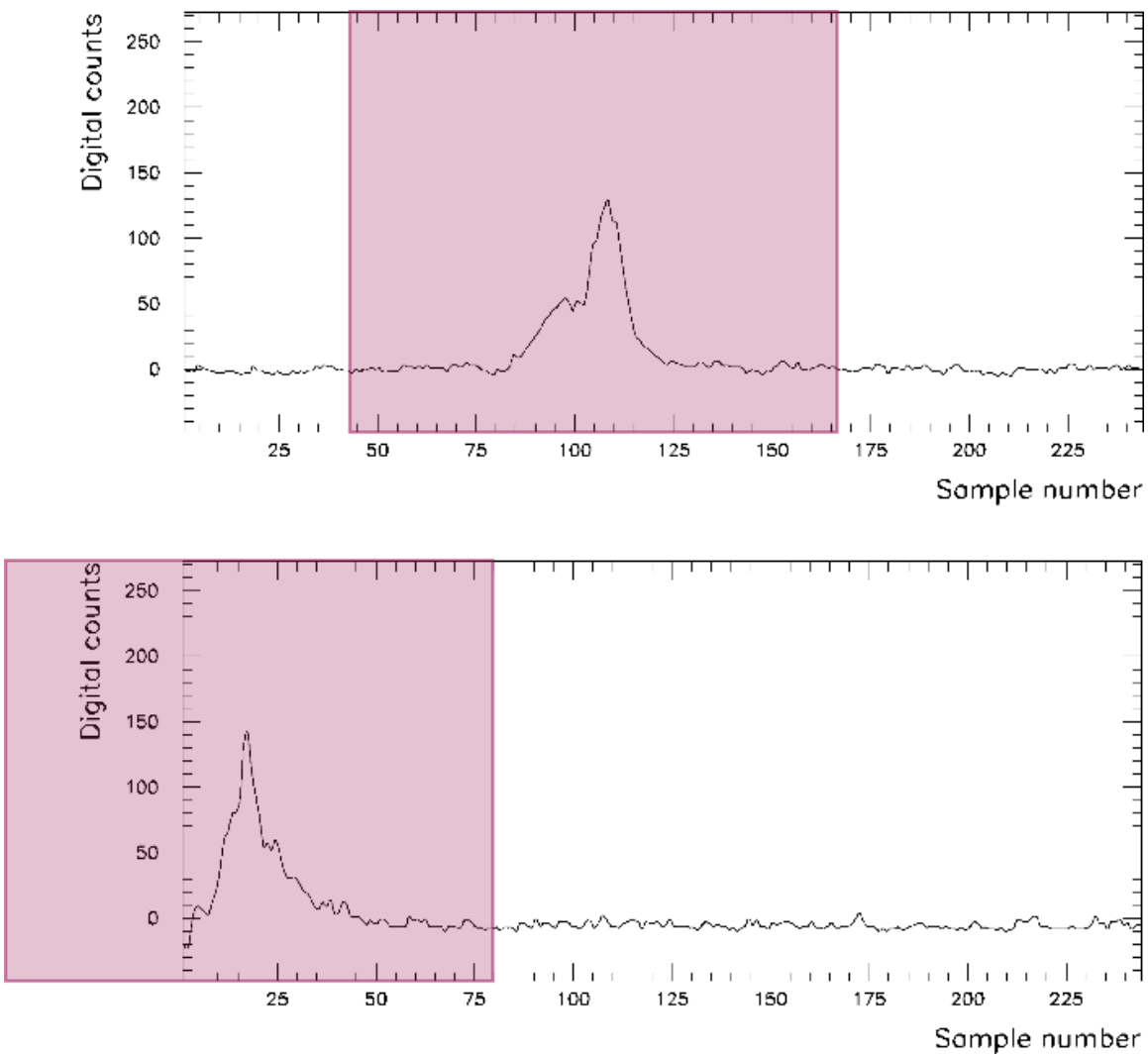

Figure 4.5. Sample FADC traces of a distant laser event. *Top:* FADC trace of a distant laser event from a single pixel passing analysis. *Bottom:* A similar FADC trace with the pixel signal considered truncated. The pink shaded region represents the 125-sample wide integration window.

instead. Figure 4.6 shows both the Chandrasekhar formula (equation 4.8) and the typical formula (equation 4.1) for the angular distribution.

$$P_{Ray}(\theta) = \frac{3}{4(1+2\gamma)}[(1+3\gamma)+(1-\gamma)\cos^2\theta]$$
$$\gamma = \frac{\rho}{2-\rho} \tag{4.8}$$

The GrISU(tah) software package (Duke & LeBohec, 2011) described in section 5.1 includes algorithms that simulate the detector response of the VERITAS array when a file containing photon arrival information is inputted. Utilizing the detector response simulation and photons generated by the Rayleigh scattering code developed by Shepherd (2005), the simulated data are run through the analysis algorithm described above for comparison with real data.

Mie scattering is not accounted for in the simulation, and should show up as discrepancy between simulation and data. Photons scattered from lower elevation pass through a longer

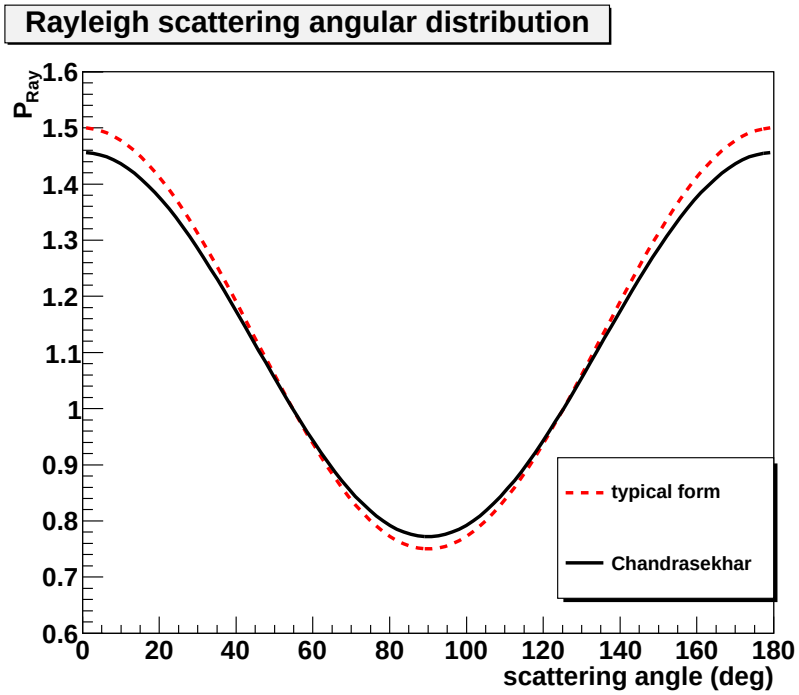

Figure 4.6. Angular distribution of Rayleigh scattered light, the typical formula (equation 4.1) and the Chandrasekhar formula (equation 4.8) which takes into account molecular anisotropy.

distance in the aerosol layer than photons scattered from higher elevation. Therefore with Mie scattering unaccounted for, the lower elevation data should appear dimmer than the higher elevation data.

4.3 Data and results

Three sets of data were taken in October 2007, February 2008, and December 2008. The infrequency of data taking is due to the time needed and complexity of the experiment setup requiring experts on hand, particularly during the earlier tests. For the earlier data taken in October 2007 and February 2008, the timing adjustments were only done for elevations 50° and above due to software issues. Only 3 telescopes were available for the December 2008 dataset. Temperature and pressure during data taking were also recorded for all three datasets. See Table 4.1 for conditions during data taking. The laser intensity was accidentally not measured for the December 2008 dataset.

4.3.1 Lightcones measurements

Lightcones are installed in front of each camera to shield the PMTs from ambient stray light and increase photon collection efficiencies by reducing the dead space between pixels. On Oct 21, 2006, a series of five distant laser runs were taken with and without the lightcones on the cameras to test the efficiencies of the lightcones. The laser was 3.47 km away and the telescopes were pointing at 20° in elevation. Throughout the five measurements (called runs from now on), the lightcones were taken off/on one telescope at a time. Table 4.2 details the settings for each run. Unfortunately, data from run 31832 are corrupted and only four runs are available for analysis. Telescopes 3 and 4 were still in construction phase at that time.

The analysis was inconclusive at first, with little change in the signal sum whether the

Table 4.1. Atmospheric conditions and distant laser intensity of each data set.

Date	Temperature [F]	Atm. Pressure [mbar]	Avg. Laser intensity [μJ]
2007-10-19	57.9	1018	6.77 ± 0.09
2008-02-14	56.2	1010	4.97 ± 0.13
2008-12-10	35.0	1023	N/A

Table 4.2. Run-by-run lightcones configuration and measurements. The average signal per pixel per event is normalized by the laser intensity, which flucuated by less than 5%. Only two telescopes were available in 2006; the other two were still in construction.

run number	T1 cones	T1 average signal per pixel [dc/pix/evt/laser intensity]	T2 cones	T2 average signal per pixel [dc/pix/evt/laser intensity]
31831	on	36.56 ± 0.65	on	30.56 ± 0.53
31832	on	N/A	off	N/A
31833	off	43.10 ± 0.09	off	32.81 ± 0.06
31834	off	32.71 ± 0.06	on	29.00 ± 0.05
31835	on	33.27 ± 0.05	on	33.01 ± 0.05

lightcones were on or off of the camera. In an attempt to reduce the analysis systematics, only pixels that contained the laser pulse more than 85% of the time in all four runs are used, which corresponds to 10 pixels in T1 and 11 pixels in T2. The intensity of the laser was measured before and after each run's data taking and fluctuated by no more than 5%. Between run 31833 and 31834 T1 lightcones were off in both runs but the signal sum showed a 27% drop. The background signal appears to be constant throughout all four runs, but it should be noted that each run was taken roughly 30 minutes apart due to the time needed to maneuver the lightcones on and off the camera. The camera system is recommended to have 1 hour of warm-up before data taking so it is unclear the effect of having the camera turned on and off for the lightcones maneuver even though the camera has gone through the 1 hour warm-up period at the beginning. The temperatures recorded for each run are observed to have decreased by $\sim 3°$C over the duration of the entire dataset, from 12.3°C at the beginning to 8.8°C at the end of the measurements. It is not clear the effects of the temperature change in combination with the lack of electronics warm-up. Given the results and the caveats of the setup, the lightcone efficiency study dataset is inconclusive.

4.3.2 Camera rotation

From the first dataset (Oct 2007), telescope 4 (T4) camera images of distant laser events appear tilted from a casual examination by eye (see Figure 4.7). Using the standard analysis routine which does a moment analysis of the image and output ellipsoidal parameters, the angle between the camera vertical axis and the image major axis (ϕ) is measured for all three datasets. A total of 19 runs is used and each data run contains several hundred laser

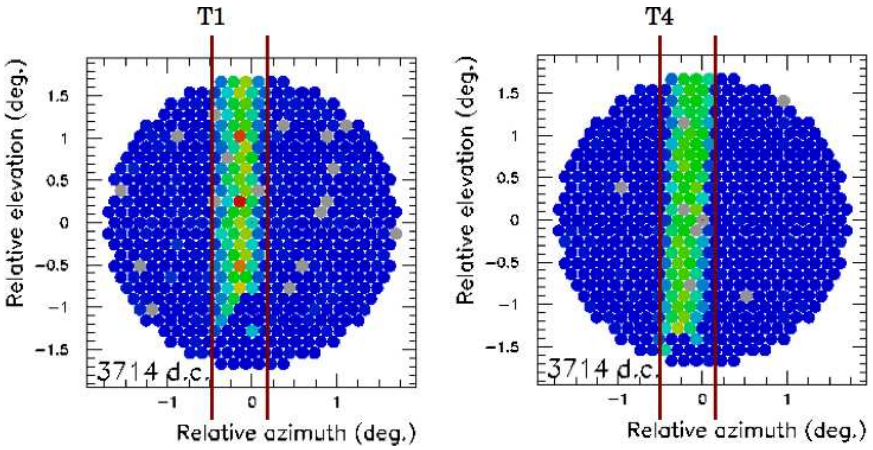

Figure 4.7. Side-by-side comparison of camera images from a distant laser event in telescopes 1 and 4. Red vertical lines are added as a guide.

events. The angle ϕ is averaged for each data run and the RMS spread of the ϕ distribution is used to calculate the weighted average of ϕ for each dataset. The rotation comparison is made relative within each dataset in case the laser was not firing at the same angle, since between each dataset the laser was put away and had to be rebalanced each time it was set up. Table 4.3 shows the weighted averages for each telescope in each dataset.

Rotation measurements using other techniques such as a plumb line and the pointing monitor have provided more precise rotation measurements. In May 2009, camera clockwise rotation is measured by pointing monitors mounted on each telescope. T1, T2, and T3 are measured to be less than 1.2° while T4 is 3.1°. The uncertainty of this measurement is 0.2°. While the distant laser data indicated the existence of camera rotation and appear to be

Table 4.3. Relative camera rotation measurements. The weighted averages of each dataset, calculated from data taken in different elevations, are presented here.

dataset	T1	T2	T3	T4
2007-10-19	0.8 ± 0.3	2.0 ± 0.8	-0.2 ± 0.3	3.3 ± 0.3
2008-02-14	0.2 ± 0.1	1.5 ± 0.2	-0.1 ± 0.1	2.7 ± 0.4
2008-12-10	-0.1 ± 0.1	-1.5 ± 0.1	-0.1 ± 0.1	N/A

consistent with the plumb line measurements, a more robust algorithm is needed to provide precise rotation angle calculation.

During the construction of T4, an accident involving a broken joint weld in the structure could be the cause of the camera rotation. In addition to the rotation, T4 was also observed to have pointing hysteresis. Additional welding performed in 2010 appears to have remedied the problems.

4.3.3 Relative calibration

Within each dataset, linear image brightness density (LIBD) comparison between telescopes can show whether or not the telescopes have comparable efficiencies. LIBD is defined by the signal sum of the pixels passing analysis divided by the length of the image. The error bar shown in Figure 4.8 represents the RMS of the LIBD distribution within each run divided by the laser intensity. The LIBD is in units of photoelectrons per degree per joule (pe/deg/μJ), except for 2008-12-10 dataset where the laser intensity was not measured and therefore only the image signal/length is shown. The length of the image is converted to degrees from the known angular size of the camera pixel, and the signal sum is converted from digital counts (dc) to photoelectrons (pe) due to known differences in each camera's performance. The dc/pe ratio is extracted from the daily diagnostics of the standard laser run. The respective ratios used are listed in Table 4.4. Even with the known differences in camera performance accounted for, the LIBD of each telescope is still significantly different from each other as shown in Figure 4.8.

T1 is the prototype of the array and its decreased performance in earlier dataset can be due to older PMTs and mirrors. These components are now routinely replaced, as mentioned earlier in *Calibration Techniques* (3.3.2). T2 consistently has the lowest efficiency of the entire array, with the most recent measurement in late 2008 $\sim 20\%$ lower. The reason is unknown as relative calibration by examining mirror reflectivities and PMT efficiencies did not indicate anything unusual.

The optical efficiency of the telescopes can also be measured by looking at muon images. When a muon passes through the center of the telescope, with a parallel trajectory to the optical axis of the telescope, the resulting image of the muon's Cherenkov light is a ring. If the muon does not impact at the center of the telescope, an arc would be seen instead. These images are fitted with a ring and the Cherenkov angle of the muon is derived from the ring radii. The number of photons in the ring can then be derived from the muon's

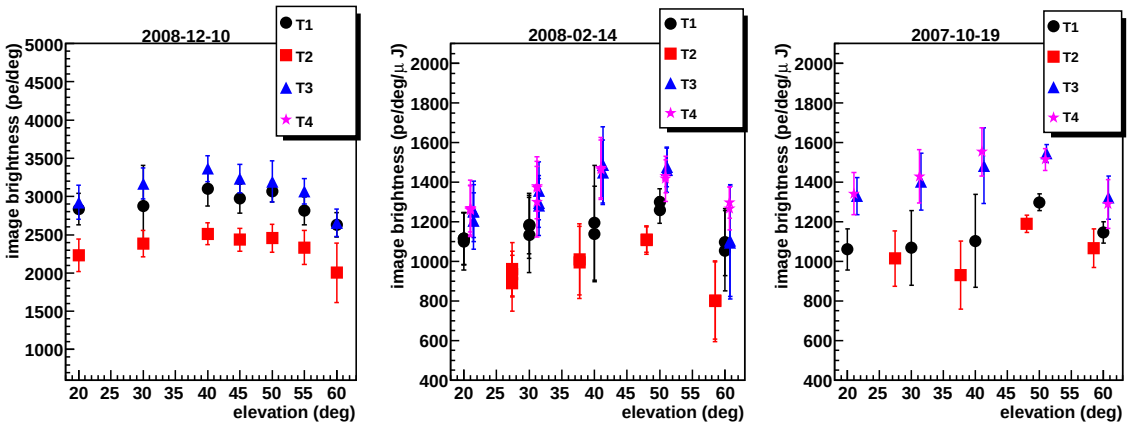

Figure 4.8. Linear image brightness density (LIBD) recorded by each telescope for each dataset. Conversion from signal sum (dc) to photoelectrons (pe) is done based on the standard laser analysis provided by the daily diagnostics. The 2008-12-10 dataset did not have the laser intensity measurement and the image signal/length is presented instead. Also the 2008-12-10 dataset is taken with an improved data acquisition software setup, which decreased the fluctuation of the measured image brightness.

Table 4.4. Corresponding standard laser run number and the dc/pe ratio used for each distant laser data set.

Date	Std. laser run number	T1 [dc/pe]	T2 [dc/pe]	T3 [dc/pe]	T4 [dc/pe]
2007-10-19	37296	5.072	5.116	4.258	4.209
2008-02-14	39400	4.752	4.877	4.010	4.100
2008-12-10	43483	4.665	4.482	4.551	4.420

Cherenkov angle (e.g., see equations 3.1 and 3.2) and compared to the signal measured by the telescopes (Hanna, 2008). Muon analysis in 2008 showed that T2 was 20% less and T4 was 10% less than the rest of the array. In 2007, when there were only 3 telescopes, muon analysis showed that T3 was 11-15% higher than T1 and T2 while both T1 and T2 were comparable. The muon 2007 and 2008 results are comparable to what was seen by the distant laser measurements.

4.3.4 Absolute calibration

Since the laser intensity measurement is available for 2007-10-19 and 2008-02-14 data sets only, Figure 4.9 shows the telescope-by-telescope comparison of the two nights. Both nights have comparable LIBD with laser intensity normalized, suggesting little change in the local atmosphere and the telescopes between the two nights.

Figure 4.10 shows the LIBD as a function of telescope pointing elevation for data and simulation. The overall shape of the LIBD is different between data and simulation. At high elevation, the data match the simulation, while at low elevation, the simulation overpredicts the LIBD observed. A plausible explanation is that at low elevation the scattered light travels a longer distance inside the aerosol layer and undergoes more Mie scattering, lowering the light intensity reaching the telescopes. This can be confirmed by taking data throughout the year with different atmospheric conditions and detailed atmospheric modelling. The VERITAS array and the distant laser setup have undergone recent changes and improvements; new measurements are planned and underway.

By comparing data at high elevation and the density of Rayleigh scattered light reaching the telescopes from simulation, we can estimate the effective light collection area of individual telescopes. For example, the recorded LIBD at 60° elevation for one telescope is $(3.93 \pm 0.18) \times 10^4\,\mathrm{dc\,deg^{-1}}$ per event, and there were $(525 \pm 1)\,\mathrm{photons\,m^{-2}deg^{-1}}$ per simulated event at the same elevation. Therefore the ratio of how many digital counts per photon for the telescope's light collecting area is $(74.8 \pm 3.4)\,\mathrm{dc\,m^2\ photon^{-1}}$. Single photoelectron measurement derived from the nightly flatfielding laser runs (Hanna, 2008) is 5.1 dc/photon. Combined with the light collecting ratio, the effective light collection area of a telescope is $(14.7 \pm 0.7)\,\mathrm{m^2}$.

The effective light collection area can also be approximated by using individual elements' measurements. The VERITAS telescopes each have a mirror area of $\sim 110\,\mathrm{m^2}$ (shadowing effect from telescope physical structures are not accounted for), quantum efficiency at laser wavelength is measured to be 0.18, mirror reflectivities at laser wavelength is 0.92, and camera efficiency is 0.81. These measurements yield an effective collection area of $15\,\mathrm{m^2}$, which is comparable to the area derived from the distant laser measurement. The uncertainties of these measurements are not found in documentation so the effective collection area from this calculation is only an estimate.

Regular distant laser runs can help monitor the local atmosphere and the performance of the array. However, since the relocation of T1 to improve array sensitivities, new software

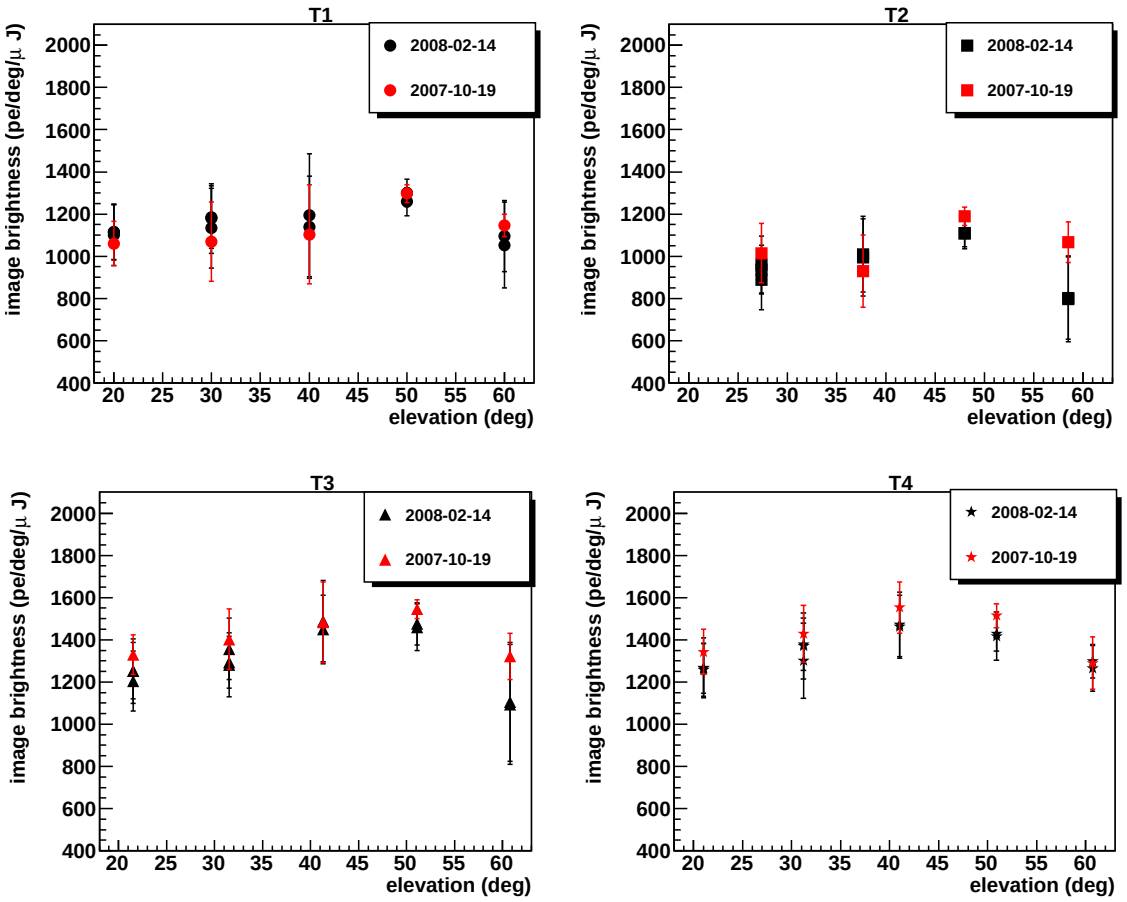

Figure 4.9. Telescope-by-telescope comparison of the linear image brightness density measured on two different nights; laser intensity has been normalized. Both nights are comparable to each other, suggesting similar atmospheric conditions and minimal changes in the telescopes on both nights.

settings for the distant laser measurements have not been functional. While there are other monitoring systems such as the pointing monitors and the FIR detectors, the distant laser is a valuable tool to provide a known light source for calibration of the telescopes and should be incorporated into the new array setup.

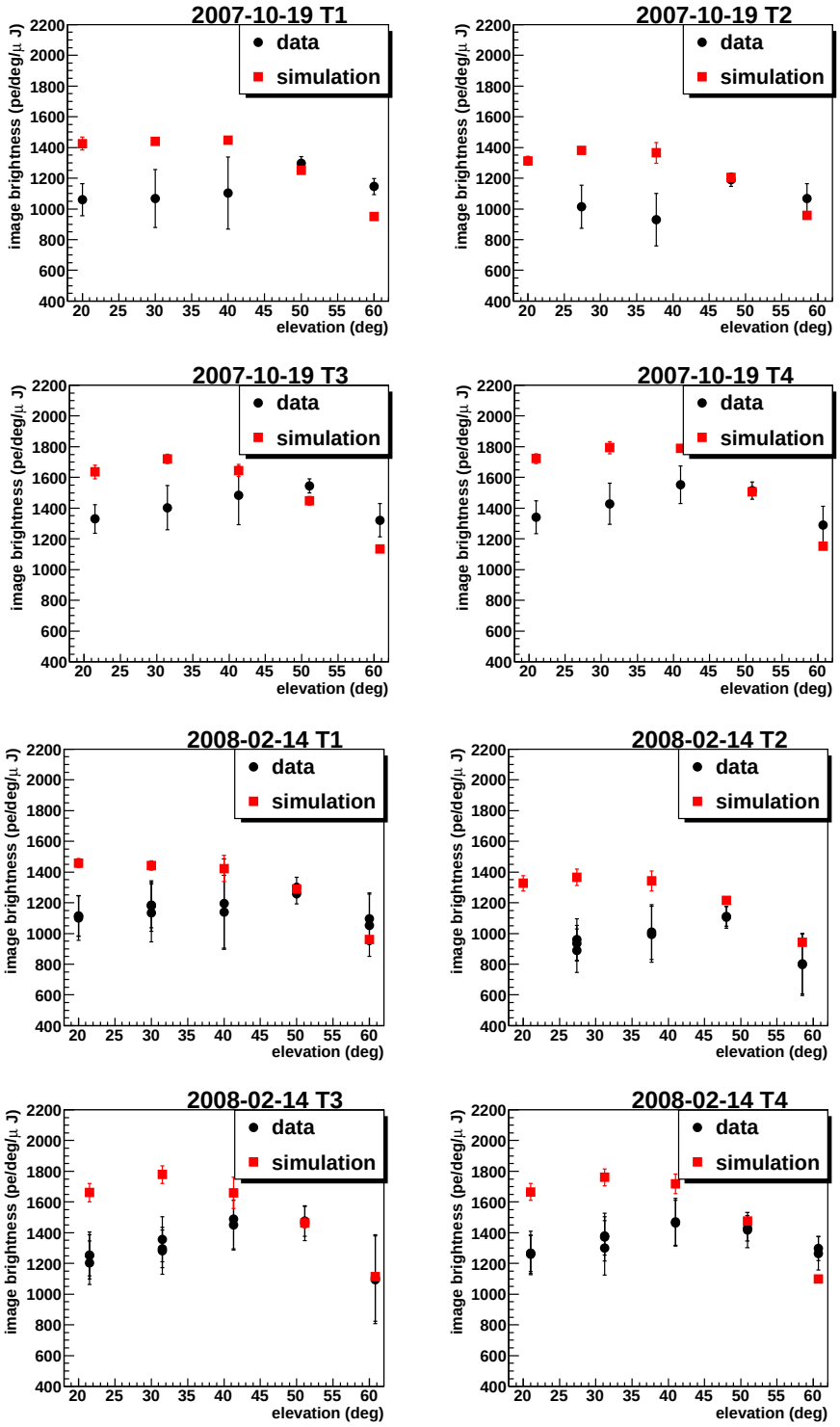

Figure 4.10. Distant laser linear image brightness density comparison between data and simulation. Data and simulations are well-matched above 50° elevation. The discrepancy at the lower elevations could be due to additional scattering not accounted for in the Rayleigh simulation.

CHAPTER 5

ANALYSIS TECHNIQUE

Over 99.9% of the data recorded are originated from cosmic rays. The distinction between cosmic-ray and gamma-ray events (explained in section 3.1 *Extensive Air Shower*) are made in the analysis algorithms from the images. Shower images recorded by the camera of each telescope can be parametrized to distinguish gamma-ray induced shower from cosmic-ray induced showers (for example see Figure 5.1). This is first detailed by Hillas (1985) who used parameters such as width, length, and orientation of the Cherenkov images to discriminate gamma-ray showers from hadronic showers. Additional parameters have been developed since then to improve the distinction even further. In our current analysis, all images are first run through a cleaning algorithm in which only pixels above a predetermined signal sum threshold are retained. Moment analysis is then applied to the cleaned images in order to extract ellipsoidal parameters such as width, length, centroid location, number of pixels passing cleaning, and the digital output sum of the image for example. Events are selected as gamma-ray-like if at least three camera images pass these cuts.

Figure 5.1 shows the distributions of these image parameters and how they differ between gamma-ray events and cosmic-ray events. These plots are generated from data of the gamma-ray standard candle source, the Crab Nebula, which is a very strong gamma-ray source. The off-source regions contain cosmic-ray events only since there are no gamma-ray source in those regions and any events passing cleaning and loose cuts on the image parameters will be cosmic-ray events. The loose cuts are not optimized to generate maximum signal but are determined by the mean and RMS of image parameters' histograms with no cuts applied. These cuts cover a broader range but still eliminate enough background that the Crab Nebula gamma-ray signal will be dominant in the ON region. Based on these parameters, cuts are optimized to generate the maximum statistical significance on the gamma-ray source region and then tested on a different set of data for validation before being used in everyday data analysis. Table 5.1 listed a sample of cuts optimized for data

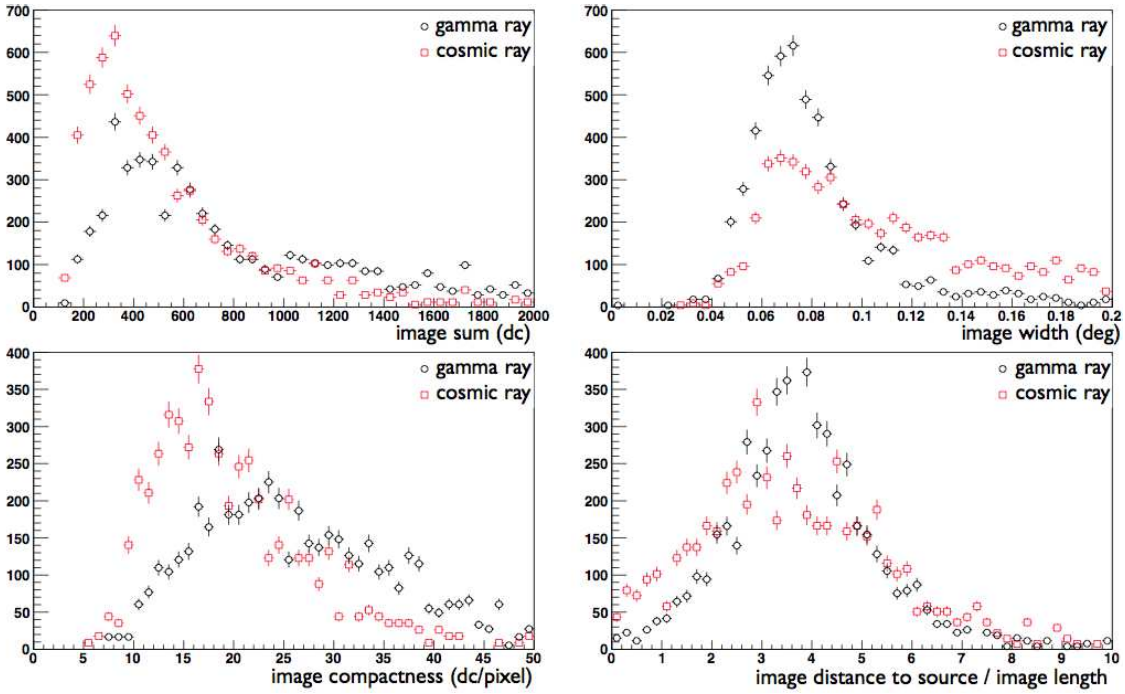

Figure 5.1. Image parameter distributions for gamma-ray events (black open circle) versus cosmic-ray events (red square). See Table 5.1 for optimized cuts applied in analysis to clean out cosmic-ray images.

taken in 2009. During the application of these cuts, corrections are applied based on the elevation and zenith angle of the telescopes pointing and the reconstructed energy of the event.

5.1 GrISU(tah) package

The entire GrISU(tah) package (Duke & LeBohec, 2011) is maintained chiefly by Charlie Duke at Grinnell College and Stephan LeBohec at University of Utah and utilizes algorithms developed by half a dozen or so people within the Whipple/VERITAS collaboration to simulate particle shower development and the corresponding detector response, and to analyze data obtained with the VERITAS array.

Table 5.1. Table of cuts optimized for a 10% Crab Nebula flux source and a 1% Crab Nebula flux source for the 2009 observing season. θ^2 is the distance squared between the image centroid and the source location.

Description	10% Crab Nebula flux	1% Crab Nebula flux
maximum θ^2	0.0085°	0.0085°
minimum number of pixels passing cleaning per image	4	4
minimum signal sum per image	500.	500.
image width	$0.045^\circ - 0.09^\circ$	$0.04^\circ - 0.09^\circ$
minimum image compactness	15	20
image distance to source / image length	1.8 - 8.0	1.8 - 8.0

5.1.1 Calibration

For the analysis of VERITAS data, the nightly laser run described in section 3.3.2 (*The VERITAS Array: Calibration Techniques*) is first analyzed to obtain the gain and timing corrections for each individual pixel of each camera. Then the signal trace baseline is subtracted from the signal and the nightsky background noise is estimated for each run from the events triggered by the GPS clock of the array (pedestal events). The variance of each signal trace is calculated and the mean pedestal standard deviation is obtained for each telescope.

5.1.2 Gamma-ray shower reconstruction

First the image is passed through a cleaning algorithm which uses each telescope's own pedestal standard deviation. The cleaning algorithm first selects only pixels with signal sum at least 5.5× the pedestal standard deviation (picture threshold), or pixels with the signal sum at least 2.5× the pedestal standard deviation that are also bordering a pixel that passes the picture threshold (boundary threshold). After this first cleaning, the algorithm performs one more pass to remove isolated pixels that do not have at least one neighbor passing the first cleaning. See Figure 5.2 for a sample image and signal trace passing cleaning thresholds.

Each shower image is then parametrized as described previously into width, length, number of triggered pixels, etc. The shower direction is reconstructed from the intersection

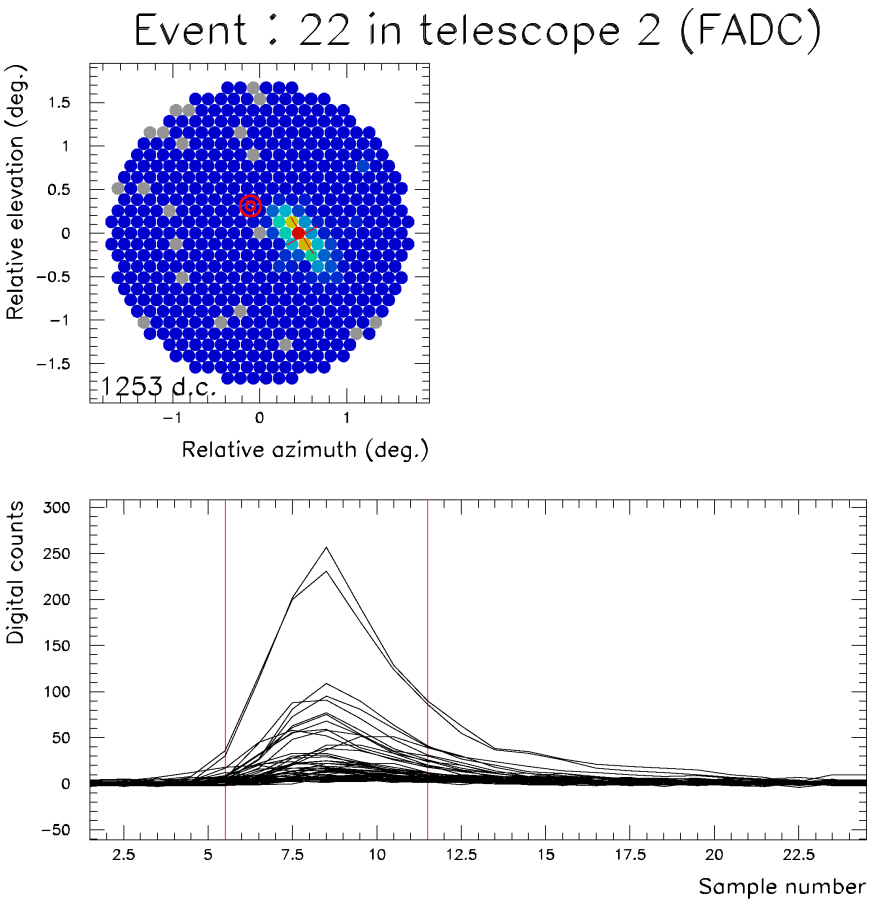

Figure 5.2. A typical camera image and signal trace of pixels passing the analysis' cleaning thresholds. The signal sum window is indicated by the vertical red lines in the trace window. Background is already subtracted and the gain/timing information of each pixel has been applied to correct for any non-uniform performance in any pixels.

of the images major axis from a pair of images (see Figure 5.3). Pairs of images must contain more than 3 pixels, an image length/width ratio of greater than 1.1, and a centroid less than 1.7° from the camera center for source position reconstruction. The following quality factors, for each image (W_{img}) and image pair (W_{pair}), are applied to the image pair reconstruction.

$$\begin{aligned} W_{img} &= (\frac{\text{length}}{\text{width}} - 1) \times \sqrt{\text{sum} - 70} \\ W_{pair}(T_i, T_j) &= W_{img}(T_i) \times W_{img}(T_j) \times (\sin(\phi_i - \phi_j) - 0.1) \end{aligned} \tag{5.1}$$

Events are then selected as gamma ray-like if at least three camera images pass selection cuts optimized for a 10% Crab Nebula flux source, or cuts optimized for 1% Crab Nebula

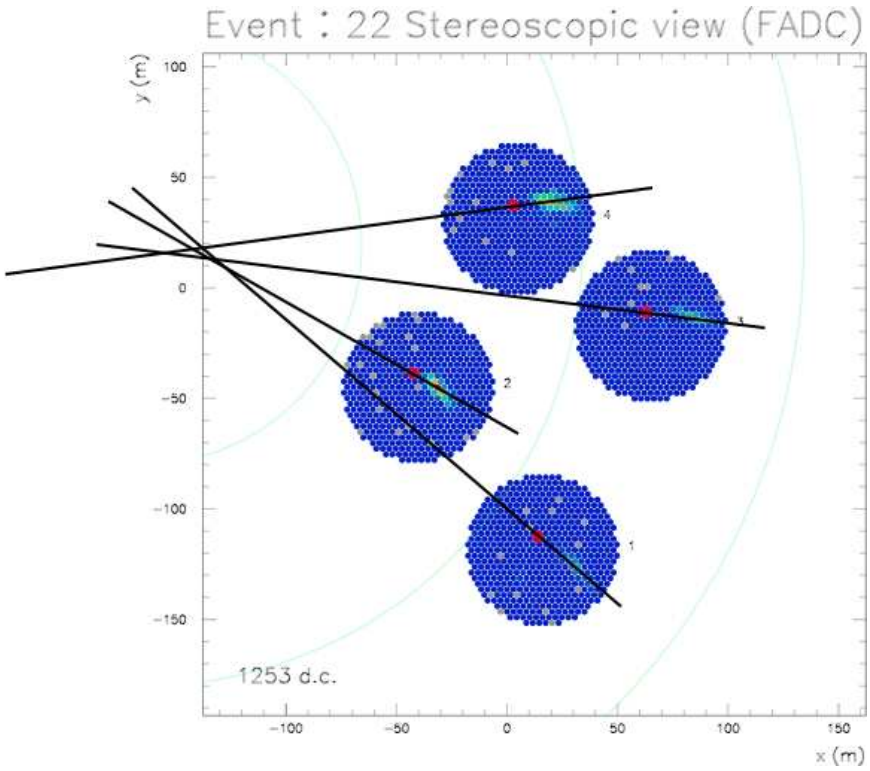

Figure 5.3. Stereoscopic reconstruction of shower impact point on the plane perpendicular to telescope pointing using the intersection of image major axes.

flux source if the source is known to be weak. The selection cuts include the number of pixels in the camera image, the digital sum of the image, image width and compactness, and distance between the image centroid and the camera center. See Table 5.1 for cuts details.

The number of gamma rays coming from the observed region is calculated by

$$N_s = N_{on} - \alpha N_{off} \tag{5.2}$$

where α is the normalization accounting for time duration difference between the source region (ON) and the background region (OFF). The number of gamma ray-like counts in the ON and OFF regions are governed by counting statistics. Therefore the standard deviation of the ON and OFF counts, assuming Poisson distribution, are:

$$\begin{aligned} \sigma_{on} &= \sqrt{N_{on}} \\ \sigma_{off} &= \alpha\sqrt{N_{off}} \\ \sigma_s &= \sqrt{\sigma_{on}^2 + \sigma_{off}^2} = \sqrt{N_{on} + \alpha^2 N_{off}} \end{aligned} \tag{5.3}$$

The significance of the gamma-ray signal is defined by the signal count (N_s) and its standard deviation.

$$S = \frac{N_s}{\sigma_s} = \frac{N_{on} - \alpha N_{off}}{\sqrt{N_{on} + \alpha^2 N_{off}}} \tag{5.4}$$

This is a quick and approximate way to calculate the significance of the signal. However, as pointed out by Li & Ma (1983), Monte Carlo simulation shows that this formula tends to over/underestimate the significance when α deviates from 1. Their paper then continued to describe the maximum likelihood ratio test where the null hypothesis (no gamma-ray signal excess) is tested and they derived the goodness of fit which is the significance of the observed signal. In their Monte Carlo simulation, the formula derived from this method is the most consistent to the expected values and can be applied to a variety of α values in general. In our analysis software, the Li & Ma formula 17 derived from the maximum likelihood method is used and is reiterated below:

$$S = \sqrt{2}\left(N_{on}\ln\left[\frac{1+\alpha}{\alpha}\left(\frac{N_{on}}{N_{on}+N_{off}}\right)\right] + N_{off}\ln\left[(1+\alpha)\left(\frac{N_{off}}{N_{on}+N_{off}}\right)\right]\right)^{1/2} \tag{5.5}$$

5.1.3 Background methods

At the beginning of the gamma-ray astronomy era, data were taken by tracking the source at the center of the camera (ON run). Immediately after, a background run (OFF

run) was taken with the same duration but tracking at a position within the same range of zenith and azimuth angles. Both the ON and OFF runs were then processed by image parametrization and reconstruction technique similar to the description in the previous sections 5.1.1 and 5.1.2. The gamma-ray event counts from the ON/OFF runs were then used in the analysis to determine the significance of the gamma-ray signal.

The disadvantage of determining background counts by taking a run with similar duration is time consumption. To analyze 30 minutes of on source data, it requires 60 minutes of observation because an additional 30 minutes is spent on a background run with similar zenith and azimuth tracking. Berge et al. (2007) presented an innovative way of background modelling that is currently being used in most pointed observations. Their methods use the same observation run for both the source and background estimation by taking advantage of the source being off centered in the camera's field of view. The two main background methods currently used for the analysis of the VERITAS data are the reflected regions and the ring background. Figure 5.4 shows graphically how the background is estimated using the same observation run.

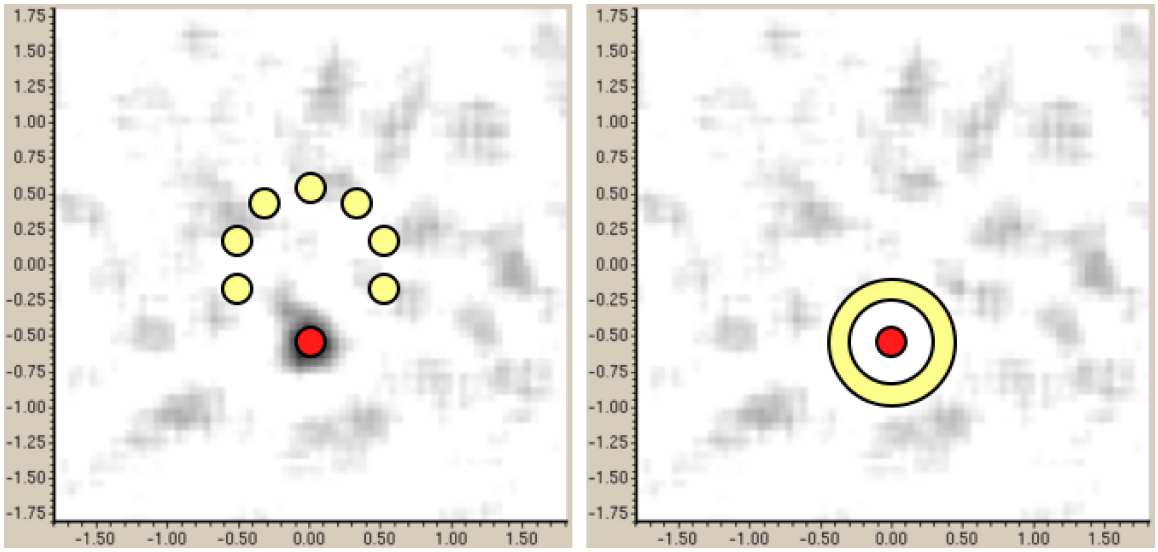

Figure 5.4. Background estimation methods available for GrISU(tah) data analysis: reflected regions (left) and ring background (right). Each shows the camera's field of view with a gamma-ray source offset by 0.5° from the center. The ON region is represented by a red circle, and the OFF regions are represented by yellow circles/ring.

For both of these background methods, the ON region is defined to be a circular area with radius typically around 0.1° centered around the source (θ in the cuts Table 5.1). Hence these background methods are optimal for point source observation and nonideal for extended source or survey purpose where the position of the gamma-ray object is unknown.

The ring background method estimates gamma-ray background by taking a ring-shaped OFF region with the ON region at the center. Care must be taken in setting the ring radius. The camera response degrades radially from the camera center and is also affected by the zenith and azimuth angles of the telescope pointing. These effects are taken into account and a camera acceptance map is produced before calculating the excess and significance of the gamma-ray object (Figure 5.5). If the ring is too close to the source, the source signal may contaminate the background estimate (see Figure 5.5 for a map of camera acceptance). The ring area used to estimate the background is split into sections (typically 16) and the 2 sections with the highest and lowest count rates are disregarded to avoid accidentally counting the gamma-ray source as background when generating a map of the observed region.

The reflected regions method uses multiple circular regions the same size and shape as the ON region and arranges them in a mirrored way to estimate the gamma-ray background. The OFF region counts are corrected with a radial acceptance function to reduce systematics

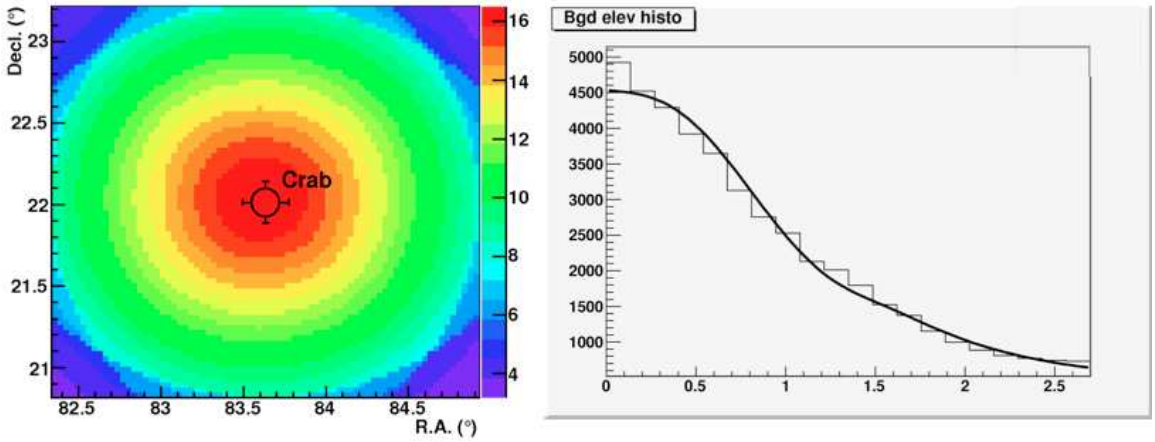

Figure 5.5. Camera acceptance and background fitting of the GrISU analysis. *Left:* Map of camera acceptance for the gamma-ray source Crab Nebula. *Right:* Histogram of background events as a function of radial distance and its polynomial fit.

(see Figure 5.5). To avoid counting the gamma-ray source or any bright stars as background during map generation, the OFF regions are compared to their immediate surrounding area of a ring radius proportional to the θ^2 cut. Any OFF regions containing event counts more than 3.5 standard deviations from its ring background is disregarded to avoid over/underestimating the background.

5.2 Analysis of the Crab Nebula

The Crab Nebula is a pulsar wind nebula located at right ascension (RA) $05^h34^m31.9^s$ and declination (δ) $22°00'52''$, approximately 2 kpc away. It has been detected in many wavelengths from radio to VHE gamma rays. Polarization was observed in radio, optical, and X-ray which suggested the presence of synchrotron-emitting electrons. A radio pulsar, PSR 0531, was found near the center of the nebula and is believed to be the source of relativistic electrons. VHE gamma rays were first predicted from the Compton synchrotron model (Gould, 1965) in which gamma rays are produced via inverse Compton scattering of relativistic electrons accelerated by the pulsar with the synchrotron photons from the said electrons. It was not until 20 years later that strong evidence for TeV gamma-ray emission from the Crab Nebula was presented by the Whipple collaboration (Weekes et al., 1989). The source was detected at a statistical significance of $9\,\sigma$ above the cosmic-ray background, without evidence for variability. Since then the Crab Nebula became the standard candle in TeV gamma-ray astronomy due to its strong and stable emission.

Despite the presence of a pulsar, pulsed gamma rays were not observed by ground-based gamma-ray telescopes until 2008 by the MAGIC 17 m telescope with a special low energy trigger. Aliu et al. (2008) reported pulsed emission above 25 GeV at a significance of $6.4\,\sigma$ with a small excess above 60 GeV at $3.4\,\sigma$. VERITAS Collaboration et al. (2011) reported pulsed gamma rays detected above 100 GeV by the VERITAS telescopes at $6.0\,\sigma$ and a photon energy spectrum between 100 GeV and 400 GeV. The spectrum observed by VERITAS, combined with the Fermi spectrum, showed that a broken power-law is a better fit than an exponential cut-off and this resultant spectral shape cannot be explained by current pulsar models.

5.2.1 Flaring activity from the Crab Nebula

In September 2010, increased gamma-ray flux from the nebula was detected by the gamma-ray satellite AGILE, which was then confirmed by the Fermi satellite. Tavani et al.

(2011) reported a peak flux of 3 times the average Crab Nebula flux at a statistical significance of $4.8\,\sigma$ between 100 MeV and 10 GeV for 2 days in September 2010. Additionally, they also reported a peak flux of 4 times the average Crab Nebula flux at $6.2\,\sigma$ for 1 day in October 2007. No variation in the gamma-ray pulsar timing was observed in either flare. The observed time scale and luminosity of flare constrained the gamma-ray production region close to the pulsar.

Abdo et al. (2011a) reported gamma-ray flaring activity above 100 MeV in September 2010 and in February 2009. For the February 2009 flare, the flare lasted 16 days, with a gamma-ray flux 3.8 ± 0.5 times above the average Crab Nebula flux. This increase in flux is at a statistical significance of over $8\,\sigma$ when compared to the average flux observed by Fermi. The September 2010 flare lasted 4 days around the same period AGILE reported a gamma-ray flare. The observed flux was 5.5 times above the average flux and the flux increase is at a significance of over $10\,\sigma$ compared to the average flux. No variation in the pulsar timing is observed, confirming the report by AGILE.

No flux variability was detected in radio, infrared, X-rays, and VHE gamma rays (Espinoza et al., 2010; Kanbach et al., 2010; Ferrigno et al., 2010b; Evangelista et al., 2010; Shaposhnikov et al., 2010; Mariotti, 2010b; Ong, 2010), and no glitch is detected in the radio timing of the pulsar (Espinoza et al., 2010). A feature approximately 3 arcseconds east of the pulsar was observed to be $\sim 10\,\%$ brighter following the gamma-ray flare in X-ray and optical (Tennant et al., 2010; Ferrigno et al., 2010a; Horns et al., 2010; Caraveo et al., 2010). This type of brightening has been observed previously and it is unclear whether it is associated with the gamma-ray flare (Horns et al., 2010; Tennant et al., 2010).

The VERITAS data and analysis chain have been validated by reproducing the Crab spectrum. VERITAS observes the Crab Nebula every year to ensure stable performance of the array and study its systematics. The following section details the GrISU(tah) analysis on the Crab Nebula data from VERITAS.

5.2.2 Observations from 2007 to 2010

Table 5.2 displays the result using the GrISU(tah) analysis package (version 2009Sep01) for data taken toward the Crab Nebula between 2007 and 2010. Since the VERITAS array shuts down in the Summer due to monsoon season, each observation season denotes Fall of that year and the Spring of the following year (e.g., 2007 season is from Fall 2007 to Spring 2008).

Table 5.2. Results of the Crab Nebula observation from 2007 to 2010.

Observation Season	Gamma rate [γ/min]	Background rate [event/min]	Sensitivity [$\sigma/\sqrt{hr}$]
2007-2008	4.16 ± 0.11	0.20 ± 0.01	27.0
2008-2009	4.33 ± 0.21	0.24 ± 0.02	27.0
2009-2010	5.42 ± 0.08	0.25 ± 0.01	30.9
2010-2011	7.01 ± 0.17	0.48 ± 0.02	33.4

T1 was relocated in the Summer of 2009 to improve sensitivity due to its subprime location as a prototype for the array configuration. The previous configuration was asymmetrical, with T1 and T4 only 35 m apart. Figure 3.5 showed the aerial view of the reconfigured array, with each telescope at a minimal distance of 80 m apart. With the relocation of T1, the array collection area was increased and cosmic-ray background rejection was improved, the sensitivity of the array was improved by 30%. Sensitivity can also be quoted in terms of how many hours of observation are required for a $5\,\sigma$ detection of a 1% Crab Nebula flux source. Before the T1 move, VERITAS can detect a 1% Crab flux source at a $5\,\sigma$ level in under 50 hours; after the T1 move it takes less than 30 hours (Perkins et al., 2009). Using the GrISU(tah) analysis package, before the T1 move it required ~ 60 hours of observation for a 1% Crab Nebula flux source to be detected at $5\,\sigma$; after the T1 move it takes $\sim$ 40 hours. The difference in sensitivity between the VERITAS standard analysis package (VEGAS) and the GrISU(tah) analysis is probably due to the differences in image parametrization and algorithms. However, all results presented are compatible with a secondary analysis other than GrISU(tah).

5.2.3 Spectral reconstruction

To reconstruct the spectrum of a gamma-ray source, simulations are needed to account for how gamma-ray photons interact in the atmosphere and the subsequent detector response in order to extract an accurate flux of the gamma-ray source from the data output. Both the data analysis and the simulations are done in the GrISU(tah) package. The simulated detector response of a gamma-ray shower is passed through the same analysis algorithm as the data. This is needed in order to derive the flux of a source by calculating the effective collection area and the energy of an event based on parameters of the images.

The number of gamma-ray events detected can be represented by the following:

$$N_{gamma}(E_{est}) = \int_E P(E_{est}, E) A_0 \phi(E) dE$$
$$\phi(E) = \phi_0 E^{-\Gamma} \tag{5.6}$$

where $P(E_{est}, E)$ is the probability of a gamma ray with true energy E is detected with a reconstructed energy E_{est}; A_0 is the area which the gamma-ray photons impacted within, and is perpendicular to the optical axis of the telescope; $\phi(E)$ is the differential energy spectrum of the gamma-ray source, and is described by a power-law distribution with flux normalization ϕ_0 and spectral index Γ. To reconstruct the gamma-ray source spectrum $\phi(E)$ from data N_{gamma}, the probability function and the effective area are in matrix forms and these are filled by Monte Carlo simulations of gamma-ray showers at different zenith and azimuth angles. The algorithm used is first developed for the analysis of the Whipple 10 m data which is detailed by Hillas et al. (1998).

Figure 5.6 shows the residue of the GrISU(tah) analysis reconstructed energy and the true energy of a gamma-ray simulated event at zenith angles ranging from 10° to 45° in increments of 5°. The azimuth angle is not distinguished in this Figure. The reconstruction deviates by more than 10% below 150 GeV and above 10 TeV. Therefore, spectral reconstruction is only performed within this energy range, which varies depending on how large the zenith angle of the observation is since a larger zenith angle corresponds to a higher energy threshold. For example, if the dataset contains a sizeable observation time at 45° zenith angle, the spectral reconstruction should begin at 400 GeV.

Besides zenith angle dependence, the simulations are also produced for azimuth angles from 0° to 348° at increments of 12°. This is due to the intensity variation (ranges from 0.25 to 0.65 Gauss) of Earth's magnetic field (NOAA/NGDC & CIRES) affecting the charged particles' path in the electromagnetic cascade, resulting in changes in the Cherenkov image parameters based on the azimuth direction.

To ensure the data are simulated properly, image parameters are compared by using loose cuts to obtain gamma ray-like images without over-constraining the parameters such that the simulation will inevitably resemble the data. Figure 5.7 shows some of the image parameters used for selecting gamma-ray-like events. The image parameter distributions of the simulation are compatible with the data.

Figure 5.8 shows the Crab spectrum measured from 2007 to 2010 using the GrISU(tah) analysis package, with other VHE ground-based array published results for comparison (Hillas et al., 1998; Aharonian et al., 2000, 2006b; Albert et al., 2008b). The power-law

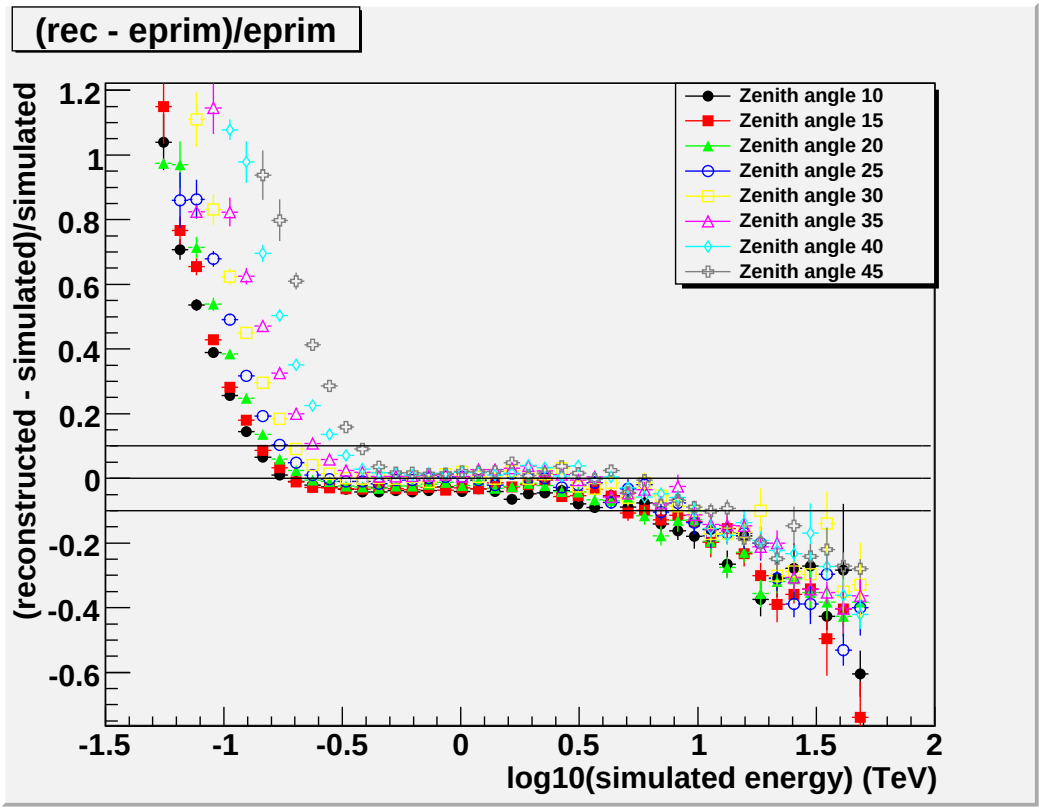

Figure 5.6. Energy difference between algorithm reconstruction and simulation as a function of the simulated energy.

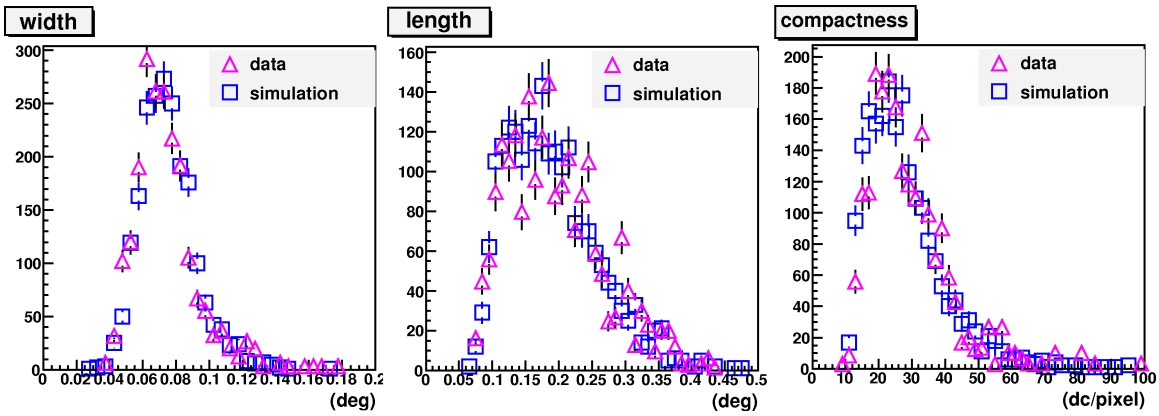

Figure 5.7. Comparison of the image parameters (width, length, and compactness) between simulation and data. All three distributions are compatible between the simulation and data.

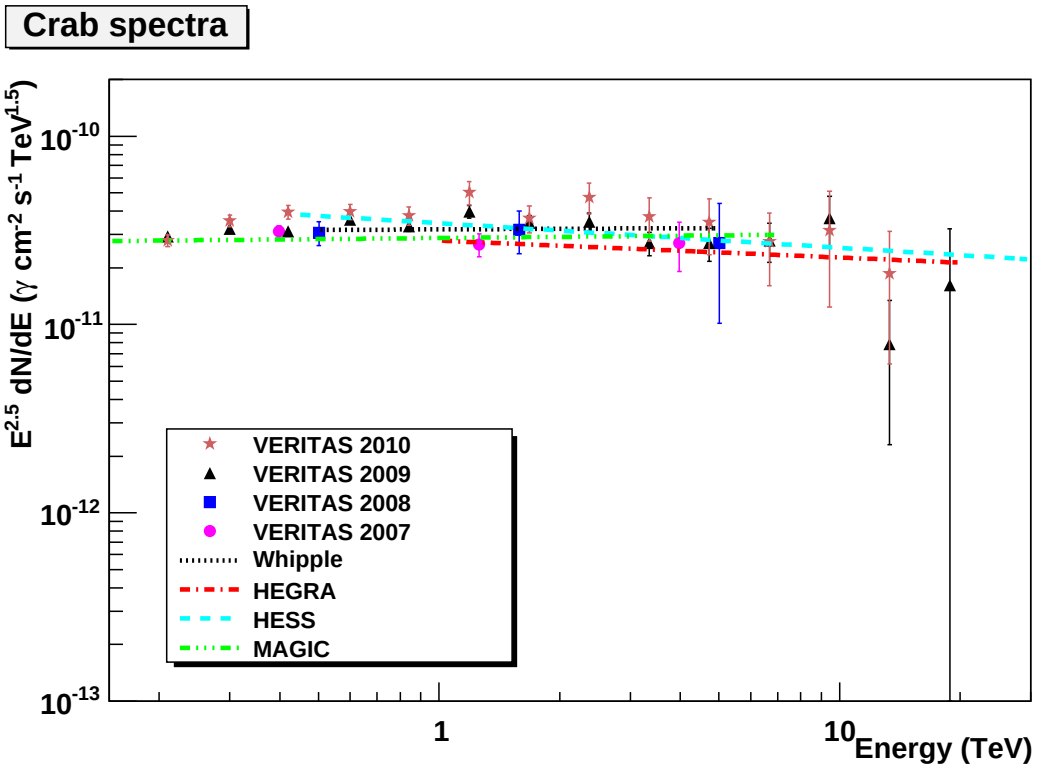

Figure 5.8. Crab spectra measured by the VERITAS array from 2007 to 2009 using the GrISU(tah) analysis package. Spectra from other VHE ground-based arrays are also plotted to show agreement (Hillas et al., 1998; Aharonian et al., 2000, 2006b; Albert et al., 2008b). The differential flux (y-axis) is multiplied by the energy to the 2.5 power in order to show case differences in different spectra and the VERITAS data points.

fit parameters of the GrISU(tah)-produced spectra and the other array spectra are listed in Table 5.3 and they are compatible with each other. It should be noted that for 2007 only 18 20-minute observation (runs) were available for analysis, in 2008 only 5 runs, and in 2010 14 runs, while in 2009 there were 50 runs. Therefore the 2009 spectral fit has much smaller error bars due to higher statistics. This analysis shows that the GrISU(tah) analysis consistently detects the Crab Nebula and reflects the sensitivity improvement due to relocation of T1 and better optical alignment in 2009.

The spectral reconstruction of the Crab Nebula showed a $1.6\,\sigma$ difference between the 2009 and 2010 integral flux, while all the other consecutive year integral flux comparisons were less than $1\,\sigma$. Between 2007 and 2009, the integral flux changed by $1.9\,\sigma$. While

Table 5.3. Power-law fit of the form $\Phi = \Phi_0(E/1\,\mathrm{TeV})^{-\Gamma}$ obtained from the GrISU(tah) analysis of 2007-2010 Crab Nebula data. Only data points that are at least $1.5\,\sigma$ away from zero are fitted.

Observation Year	Flux normalization Φ_0 $[10^{-11}$ cm^{-2} s^{-1} TeV$^{-1}]$	Spectral index Γ	χ^2/ndf	Integral flux above 250 GeV $[10^{-11}$ cm^{-2} s$^{-1}]$
2007	2.71 ± 0.11	2.60 ± 0.03	32.5/9	15.6 ± 0.7
2008	2.88 ± 0.23	2.61 ± 0.07	7.1/9	16.7 ± 1.6
2009	3.29 ± 0.08	2.47 ± 0.02	17.7/10	17.2 ± 0.5
2010	3.77 ± 0.16	2.40 ± 0.04	16.4/10	18.8 ± 0.9

the integral flux is not significantly incompatible, there has been an ongoing investigation for this increase in spectral reconstruction of the Crab Nebula which is evident in other analysis packages as well. Checks have been made to ensure this is not due to improvements or code fixes done in the software algorithm. Currently the simulation configuration file is under scrutiny to ensure the performance inputs of different detector components are indeed correct when being used in simulation.

5.3 Light curve production

The time evolution of the flux measured from a source is important for detecting flares, calculating the timescale of the flux change, and in correlation study with other wavelengths. Light curve can be produced with different timing binning (e.g., daily, monthly etc.). However, not every bin contains enough photon statistics for a $5\,\sigma$ detection. Using simulations of an assumed spectrum and similar telescope points, the effective collection area of the array can be deduced and we can convert gamma-ray count rates to integral flux as a function of time.

5.3.1 Simulation

Suppose you have simulated N_{Sim} showers over an area A_{Sim} with a minimal energy E_{Sim}. The energy distribution is a power law. The index of the integral spectrum is Γ.

The number of showers simulated with an energy greater than E is

$$N(E) = N_{Sim}(\frac{E}{E_{Sim}})^{-\Gamma} \tag{5.7}$$

Taking the derivative and dropping the minus sign:

$$\frac{dN}{dE}(E) = N_{Sim}\frac{\Gamma}{E_{Sim}}(\frac{E}{E_{Sim}})^{-\Gamma-1} \tag{5.8}$$

With $A(E)$ the effective collection area of gamma rays at the analysis level, the number of simulated events passing the analysis is:

$$n_{Cut} = \frac{1}{A_{Sim}}\int_{E_{Sim}}^{\infty} A(E)\frac{dN}{dE}(E)dE \tag{5.9}$$

This assumes A_{Sim} was chosen large enough and E_{Sim} small enough so truncation effects can be neglected. This also assumes simulations were done up to sufficiently high energies so the result is not sensitive to high energy cut-off value. Together with equation 5.8, we have:

$$n_{Cut} = \frac{\Gamma \cdot N_{Sim}}{E_{Sim} \cdot A_{Sim}}\int_{E_{Sim}}^{\infty} A(E)(\frac{E}{E_{Sim}})^{-\Gamma-1}dE \tag{5.10}$$

and

$$\int_{E_{Sim}}^{\infty} A(E)(\frac{E}{E_{Sim}})^{-\Gamma-1}dE = \frac{n_{Cut} \cdot E_{Sim} \cdot A_{Sim}}{\Gamma \cdot N_{Sim}} \tag{5.11}$$

5.3.2 Signal

The observed source is assumed to have an integral spectrum (number of gamma rays per unit area and per unit time) which can be written as:

$$\phi(E) = \Phi_{Sim}(\frac{E}{E_{Sim}})^{-\Gamma} \tag{5.12}$$

where we have used the lowest simulated energy as the reference energy.

Taking the derivative and dropping the minus sign:

$$\frac{d\phi}{dE}(E) = \Phi_{Sim}\frac{\Gamma}{E_{Sim}}(\frac{E}{E_{Sim}})^{-\Gamma-1} \tag{5.13}$$

When the source was observed, an event rate f was recorded.

$$\begin{aligned} f &= \int_{E_{Sim}}^{\infty} A(E)\frac{d\phi}{dE}(E)dE \\ &= \frac{\Phi_{Sim} \cdot \Gamma}{E_{Sim}}\int_{E_{Sim}}^{\infty} A(E)(\frac{E}{E_{Sim}})^{-\Gamma-1}dE \end{aligned} \tag{5.14}$$

Using equation 5.11 and hence assuming the source spectrum has the same spectral index as the simulated data, we get

$$f = \frac{\Phi_{Sim} \cdot n_{Cut} \cdot A_{Sim}}{N_{Sim}} \tag{5.15}$$

So, not surprisingly, the integral flux above energy E_{Sim} is $\Phi_{Sim} = \frac{f}{\epsilon \cdot A_{Sim}}$ where A_{Sim} is the area over which gamma rays were simulated and ϵ is the fraction of simulated gamma-ray

showers that resulted in events which passed the analysis. The integral flux above an energy E then is

$$\Phi(E) = \frac{f}{\epsilon \cdot A_{Sim}} (\frac{E}{E_{Sim}})^{-\Gamma} \tag{5.16}$$

5.3.3 Statistical error bars

The variance $\delta\Phi^2(E)$ of $\Phi(E)$ is:

$$\delta\Phi^2(E) = \delta f^2 (\frac{N_{Sim}}{n_{Cut} \cdot A_{Sim}})^2 + \delta n_{Cut}^2 (\frac{f \cdot N_{Sim}}{A_{Sim} \cdot n_{Cut}^2})^2 \tag{5.17}$$

where δf^2 is the variance of the rate (the square of the statistical error calculated with the Li & Ma formula) and δn_{Cut}^2 is the variance of n_{Cut} which results from a binomial distribution so here $\delta n_{Cut}^2 = N_{Sim}\epsilon(1-\epsilon)$.

5.3.4 If assumed spectrum differs from simulation

In some cases we may have simulated gamma rays with a power law energy distribution of index Γ_{Sim} while the source is assumed to have a power law spectrum of index Γ. The same calculation as above can be applied but ϵ should not be taken equal to the ratio $\frac{n_{Cut}}{N_{Sim}}$ any more. Instead, we have

$$\epsilon = \frac{\tilde{n}_{Cut}}{\tilde{N}_{Sim}} \tag{5.18}$$

Each simulated event must be given a weight $w(E)$ so the source spectrum is recovered in the simulations.

$$w(E) = (\frac{E}{E_{Sim}})^{\Gamma_{Sim}-\Gamma} \tag{5.19}$$

Then, $\tilde{n}_{Cut}$ is obtained as the sum of the $w(E)$ for each simulated event passing the cut while for $\tilde{N}_{Sim}$:

$$\begin{aligned}
\tilde{N}_{Sim} &= \int_{E_{Sim}}^{\infty} w(E) \frac{dN}{dE} dE \\
&= \int_{E_{Sim}}^{\infty} (\frac{E}{E_{Sim}})^{\Gamma_{Sim}-\Gamma} N_{Sim} \frac{\Gamma_{Sim}}{E_{Sim}} (\frac{E}{E_{Sim}})^{-\Gamma_{Sim}-1} dE \\
&= N_{Sim} \frac{\Gamma_{Sim}}{E_{Sim}} \int_{E_{Sim}}^{\infty} (\frac{E}{E_{Sim}})^{-\Gamma-1} dE \\
&= N_{Sim} \frac{\Gamma_{Sim}}{\Gamma}
\end{aligned} \tag{5.20}$$

The simulation statistical error is then complicated to compute. So one should check the statistical error is strongly dominated by the signal statistics in the case $\Gamma_{Sim} = \Gamma$.

5.4 Upper/lower flux limits calculation

In case of a nondetection, usually a flux upper limit is derived from the observations. The upper/lower limit calculation presented below is derived in Helene (1983).

Given a measured signal count of $\bar{x}$, a Gaussian is assumed for the probability density function of the signal count x:

$$g(x) = \frac{N}{\sqrt{2\pi}\sigma} e^{-(x-\bar{x})^2/2\sigma^2} \tag{5.21}$$

where $\bar{x}$ is the excess measured ($N_{ON} - \alpha N_{OFF}$), and $\sigma = \sqrt{N_{ON} + \alpha^2 N_{OFF}}$ (Li & Ma formula 4 Li & Ma (1983)) is the standard deviation.

The probability density function g(x) is normalized:

$$\begin{aligned}
\int_0^\infty g(x)dx &= 1 \\
\frac{N}{\sqrt{2\pi}\sigma} \int_0^\infty e^{-(x-\bar{x})^2/2\sigma^2} dx &= 1 \\
\frac{1}{N} &= \frac{1}{\sqrt{2\pi}\sigma} \int_0^\infty e^{-(x-\bar{x})^2/2\sigma^2} dx \\
&= \frac{1}{\sqrt{2\pi}} \int_{-\bar{x}/\sigma}^\infty e^{-y^2/2} dy \\
N &= \frac{1}{I(-\bar{x}/\sigma)} \\
I(z) &= \frac{1}{\sqrt{2\pi}} \int_z^\infty e^{-t^2/2} dt
\end{aligned} \tag{5.22}$$

where I(z) is a form of the error function.

The probability of x greater than a given value A is

$$\begin{aligned}
P &= \int_A^\infty g(x)dx \\
&= \frac{N}{\sqrt{2\pi}\sigma} \int_A^\infty e^{-(x-\bar{x})^2/2\sigma^2} dx \\
&= \frac{N}{\sqrt{2\pi}} \int_{(A-\bar{x})/\sigma}^\infty e^{-y^2/2} dy \\
&= NI(\frac{A-\bar{x}}{\sigma}) \\
P &= I(\frac{A-\bar{x}}{\sigma}) / I(\frac{\bar{x}}{\sigma})
\end{aligned} \tag{5.23}$$

For 99% confidence upper/lower limit A, $P = 0.01/0.99$.

CHAPTER 6

M87 VHE OBSERVATIONS

VHE emission from M 87 was first reported by the HEGRA collaboration from their $1998-1999$ observations with an array of 5 telescopes (Aharonian et al., 2003). From their 83.4 hours of observation, an excess of photons above 730 GeV with a statistical significance of 4.1 standard deviation (σ) from the background was measured. The photon excess was reported to be a point-like source at position RA $12^h30^m54.4^s \pm 6.9^s_{stat} \pm 1.7^s_{syst}$ dec $12°24'17'' \pm 1.7'_{stat} \pm 0.4'_{syst}$, which is consistent with the M 87 nucleus position. However, extended emission could not be excluded due to low statistics. No significant variability was apparent in the dataset. Spectral analysis showed the data can be fitted well with a power law $\mathrm{dN/dE} \sim \mathrm{E}^{-\Gamma}$ with $\Gamma = 2.9 \pm 0.8_{stat} \pm 0.08_{syst}$. The integral flux above 730 GeV was measured to be $(9.6 \pm 2.3) \times 10^{-13}\gamma\mathrm{cm}^{-2}\mathrm{s}^{-1}$, corresponding to $3.3 \pm 0.8\%$ of the Crab Nebula flux.

The Whipple 10 m telescope observed M 87 from 2000 to 2003 for a total of 39 hours (Le Bohec et al., 2004). No significant excess was detected and a 99% confidence level (C.L.) upper limit for integral flux above 400 GeV was reported to be $6.9 \times 10^{-12} cm^{-2} s^{-1}$, corresponding to $\sim 8\%$ of the Crab Nebula flux.

In 2006, H.E.S.S., an array of four telescopes, confirmed VHE emission of M 87 from 89 hours of observations taken between 2003 and 2006 (Aharonian et al., 2006a). A statistical significance of $13\,\sigma$ photon excess was observed at the position RA $12^h30^m47.2^s \pm 1.4^s_{stat}$ dec $12°23'51'' \pm 19''_{stat}$, which is consistent with the M 87 nucleus position, and was reported to be point-like with a 99.9% C.L. upper limit of $3'$ on the source extension using a Gaussian profile fit. Additionally, flux variability in time scales of days was observed in their 2005 dataset when M 87 appeared to be in a flaring state. The discovery of burst-like behavior from M 87 established a size constraint on the VHE emission region due to the light crossing time. Since information cannot propagate faster than the speed of light, the variability time scale gives an upper limit on how large the emission region can be. The size limit in turn constrains the environment parameters in the modelling of VHE photon production.

Large-scale production models such as dark matter annihilation (Baltz et al., 2000) and the interacting cosmic-ray proton scenario (Pfrommer & Enßlin, 2003) which predict steady gamma-ray emission are unlikely as the major contributor of VHE photon production. Other potential particle acceleration sites such as the extended kiloparsec jet and the brightest jet feature knot A are also excluded from the size constraint. The two remaining candidates are the knot HST-1 and the nucleus. While there is no lower size limit for the knot HST-1 to be excluded as a potential site, an unrealistically small opening angle is required for the energy transfer between the nucleus and the VHE gamma-ray production zone. Given the VHE emission size constraint is $5 \times 10^{15} \delta$ cm, and the distance between the knot HST-1 and the nucleus is 0.86 arcseconds (2×10^{20} cm projected), the energy from the nucleus need to be channeled within $1.5 \times 10^{-3} \delta$ degree. This leads to the conclusion of Aharonian et al. (2006a) that the nucleus is the more likely origin for VHE emission production.

Figure 6.1 shows the observed yearly average VHE flux from M 87 since 1998 from different experiments, and the grey region highlights the range of flux levels during flaring episodes. VERITAS has been observing M 87 since 2007 when the array was commissioned and recorded two of the three VHE gamma-ray flares observed since 2005. Starting in 2008, the three major atmospheric Cherenkov arrays, H.E.S.S., MAGIC, and VERITAS have been involved in a joint campaign to ensure at least one instrument is monitoring M 87 when it is observable. Only VERITAS data are shown for 2009 and 2010 in Figure 6.1 as the other data are not publicly available yet. The details of the VERITAS observations are described in the subsections below.

6.1 VERITAS observations

6.1.1 2007 observation

VERITAS first observed M 87 in 2007 with a 3-telescope array while still in its construction phase (Acciari et al., 2008). From ~ 51 hours of observations with zenith angle ranging from 19° to 35°, 44 hours of the observation time passed the quality selection cut. An excess of 259 photons, at a statistical significance of $5.9\,\sigma$ above the background, was detected from a point-like source at position RA $12^h30^m46^s \pm 4^s_{stat} \pm 6^s_{sysm}$ dec $12°23'21'' \pm 50''_{stat} \pm 1'30''_{sysm}$, which is consistent with the M 87 position. A 99% C.L. upper limit of $4.5'$ on the source size was established from this dataset. The average integral flux above 250 GeV was $(3.47 \pm 0.71) \times 10^{-12}\,\gamma\,\mathrm{cm}^{-2}\,\mathrm{s}^{-1}$, corresponding to 1.9% of the Crab Nebula flux. A constant flux fit to the 2007 light curve (top panel of Figure 6.2) yielded χ^2/dof (degree of freedom)

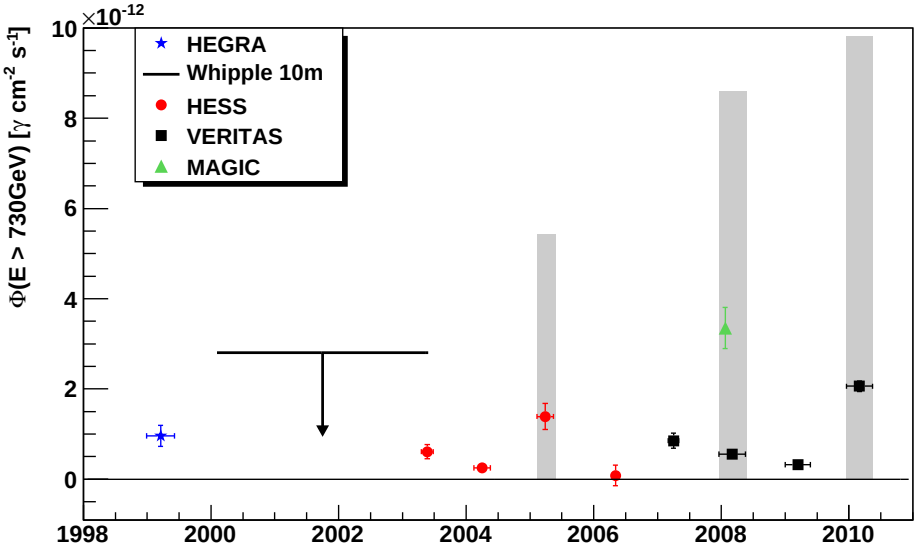

Figure 6.1. Average VHE flux and upper limit reported by different IACT observatories since 1998 (Aharonian et al., 2003; Le Bohec et al., 2004; Aharonian et al., 2006a; Acciari et al., 2008; Albert et al., 2008a; Acciari et al., 2010). The VHE gamma-ray flux is given for energies greater than 730 GeV to match the original flux scale used in the HEGRA paper. Note that M 87 is observed no more than 6 months each year and only under dark conditions (i.e., moon-less, cloud-less nights). Therefore there may be more flaring episodes than is observed. The duration of observation is indicated by error bars in the x-axis. The 99% confidence level flux upper limit is derived from 4 years of Whipple 10 m observation between 2000 and 2003. The range of varying flux during the year of an flaring episode is highlighted by the grey region to give a more accurate picture of the flux level of M 87.

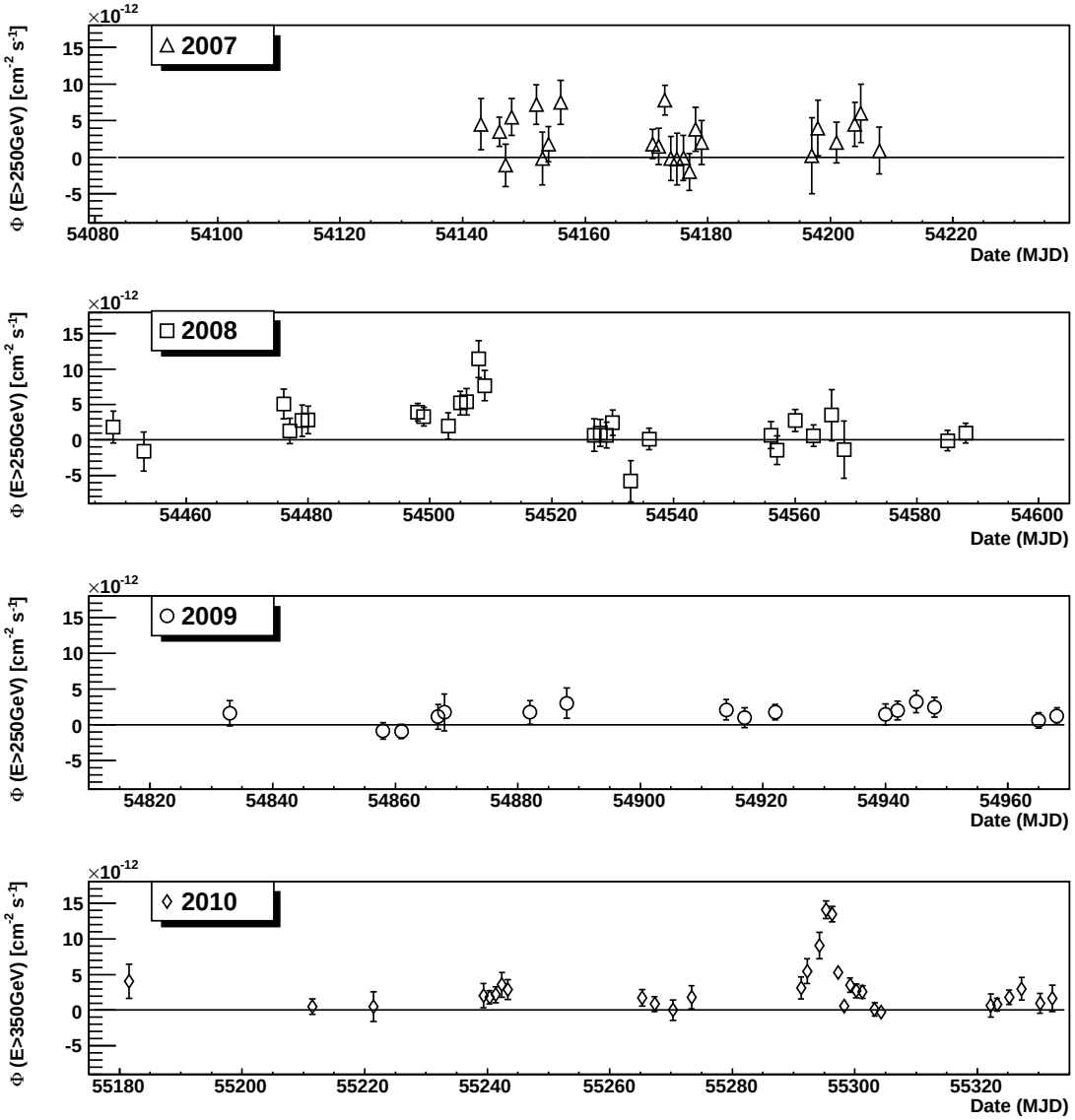

Figure 6.2. M 87 nightly flux recorded by VERITAS between 2007 and 2010. The vertical axis represents the integral flux above 350 GeV and its scale is kept the same for all four panels. The horizontal axis displays the modified Julian date (MJD) of the observations. All panels start on December 10th and end on May 19th. Larger error bars and fluctuations seen in the 2007 data are due to reduced sensitivities from having a 3-telescope only array.

of 24.3/22, corresponding to a probability of 33.2% that the flux was constant throughout this dataset. No significant variability was found within this dataset.

6.1.2 2008 observation

Between December 2007 and May 2008, M 87 was observed with a complete VERITAS array of 4 telescopes for over 43 hours. After eliminating observations in poor weather and those with unstable trigger rates, 37 hours of good quality live time with a range of zenith angles from 19° to 41° remained. An excess of 450 photons was observed at the M 87 position with a statistical significance of $7.2\,\sigma$. The average integral flux above 250 GeV was $(2.74 \pm 0.61) \times 10^{-12}\,\gamma\,\mathrm{cm}^{-2}\,\mathrm{s}^{-1}$, corresponding to 1.8% of the Crab Nebula flux. The 2008 VERITAS light curve is shown in the second panel of Figure 6.2 assuming a power-law spectral index of 2.50. The χ^2/dof of a constant flux fit to the entire dataset was 52.4/26, rejecting the constant flux hypothesis at 99.9% C.L. Flaring flux up to $11.4 \times 10^{-12}\,\gamma\,\mathrm{cm}^{-2}\,\mathrm{s}^{-1}$, equivalent to 8% of the Crab Nebula flux, was observed on February 12 2008 (MJD 54508). The details of the 2008 flare are discussed in the following section 6.2 *Flaring episodes*.

6.1.3 2009 observation

Between January and May 2009, M 87 was observed for over 27 hours at a range of zenith angles from 19° to 38°. 81% of the 2009 dataset was taken with an array of 4 telescopes and 19% was taken with a 3-telescope array. After eliminating observations in poor weather and those with unstable trigger rates, 19 hours of good quality live time remained in the 2009 dataset. An excess of 134 photons was detected at the M 87 position with a statistical significance of $4.2\,\sigma$. The χ^2/dof of a constant flux fit to the entire dataset was 23.1/18 with a corresponding probability of 18.7%. No significant variability was observed in the 2009 dataset. The average integral flux above 250 GeV was $(1.59 \pm 0.39) \times 10^{-12}\,\gamma\,\mathrm{cm}^{-2}\,\mathrm{s}^{-1}$ assuming a power-law spectral index of 2.50. This corresponds to 1.1% of the Crab Nebula flux and is consistent with the reported Fermi-LAT spectrum (Abdo et al., 2009b).

6.1.4 2010 observation

Between December 2009 and May 2010, M 87 was observed for 53 hours at a range of zenith angles from 19° to 40°, with low elevation excursions during the flare nights of April 9th through 11th when M 87 was observed until it reached a zenith angle greater than 60°. Most of the data were taken with a 4-telescope array with less than 5% of the data

taken with a 3-telescope array. After eliminating observations taken in poor weather and those with unstable trigger rates, 45 hours of good quality live time remained. An excess of 628 photons was detected at the M 87 position with a statistical significance of $25.6\,\sigma$. The average flux above 350 GeV is $(5.44 \pm 0.30) \times 10^{-12}\,\gamma\,\mathrm{cm}^{-2}\,\mathrm{s}^{-1}$, corresponding to 5% of the Crab Nebula flux. The χ^2/dof of a constant flux fit is 269.4/29, corresponding to a probability of $\sim 10^{-40}$ that the flux was constant throughout this dataset. Flaring flux up to $27.1 \times 10^{-12}\,\gamma\,\mathrm{cm}^{-2}\,\mathrm{s}^{-1}$, equivalent to 20% of the Crab Nebula flux was observed for several days in April 2010. Details of this flare are presented in the following section 6.2 *Flaring episodes*.

6.2 Flaring episodes observed by VERITAS

6.2.1 2008 February flare

On 2008 Feb 9 (MJD 54505), M 87 was detected with a statistical significance of exceeding $4\,\sigma$ after just 2 hours of observation while it took about 20 hours of observation to reach the same statistical significance when no flaring activity occurred in 2009. The peak flux of the VERITAS dataset occurred on the night of 2008 Feb 12 (MJD 54508) at $(11.4 \pm 2.6) \times 10^{-12}\,\gamma\,\mathrm{cm}^{-2}\,\mathrm{s}^{-1}$ above 250 GeV, equivalent to 7.7% of the Crab Nebula flux. The 2008 flare period is defined by the nights that need to be removed from the whole dataset so the constant flux fit of the light curve reaches a χ^2/dof close to 1. The nights that meet the criteria for the flare period are 2008 Feb 9, 10, 12, and 13 (MJD $54505 - 54509$). The dataset is then further split into preflare and postflare period.

During the flare period, M 87 was observed for 5.4 hours of live time and was detected with a statistical significance of $7.4\,\sigma$. The flux above 250 GeV during the 5-day flare period was $(7.59 \pm 1.11) \times 10^{-12}\,\gamma\,\mathrm{cm}^{-2}\,\mathrm{s}^{-1}$, corresponding to 5.1% of the Crab Nebula flux. The 99% confidence interval, assuming a normal distribution, for the flux during the flare period (see horizontal-lined area between MJD 54505 and 54509 in Figure 6.3) is between $4.73 \times 10^{-12}\,\gamma\,\mathrm{cm}^{-2}\,\mathrm{s}^{-1}$ and $10.45 \times 10^{-12}\,\gamma\,\mathrm{cm}^{-2}\,\mathrm{s}^{-1}$.

Before the flare period (MJD $54448 - 54503$), Albert et al. (2008a) reported flaring activity up to 15% of the Crab Nebula flux starting Feb 1st (MJD 54497) and flux variability on time scale as short as one day with a statistical significance of $5.6\,\sigma$. But subsequent VERITAS observations, which included two nights immediately after the major flare observed by MAGIC, did not appear to be above the normal flux level. During this preflare period, M 87 was detected with a statistical significance of $5.0\,\sigma$ with 13.8 hours of live time

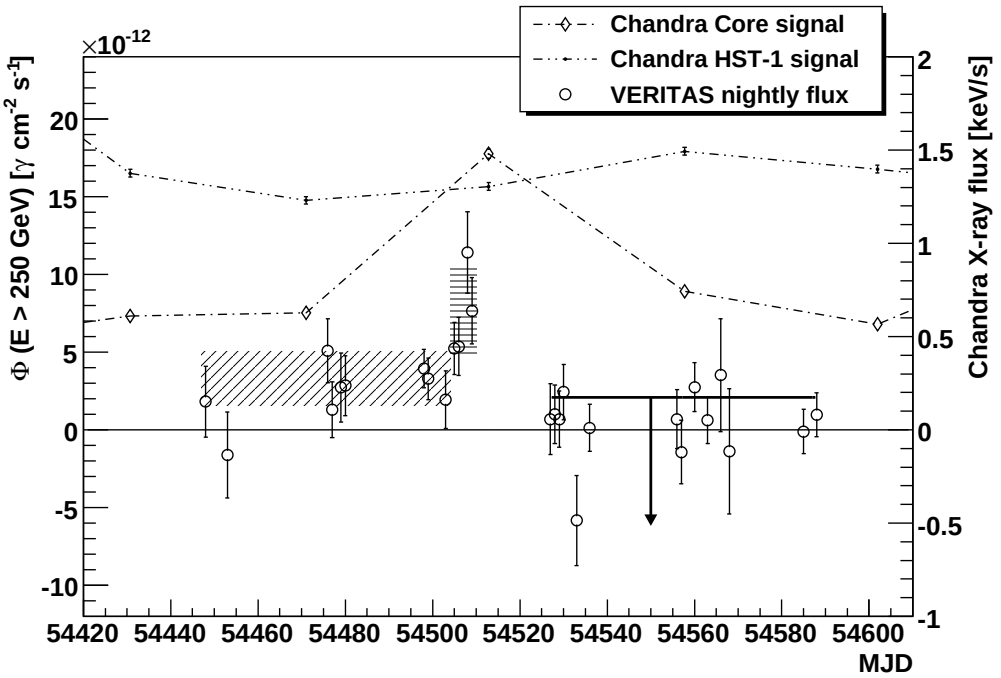

Figure 6.3. M 87 nightly flux recorded by VERITAS along with Chandra X-ray flux (Harris et al., 2009) from the core and from the HST-1 knot in 2008. The flare period (MJD 54505 – 54509, Feb 9 – 13) seen in VHE gamma rays coincides with a historically high state of the core in X-rays, while the HST-1 knot remains in a low X-ray flux state. The black slant-lined area shows the 99% confidence intervals of the preflare period; the black horizontal-lined area shows the 99% confidence intervals of the flare period; the black line with the arrow indicates the upper limit of the postflare period at 99% C.L. (Helene, 1983).

at a flux of $(3.30 \pm 0.68) \times 10^{-12}\,\gamma\,\mathrm{cm}^{-2}\,\mathrm{s}^{-1}$ above 250 GeV. The 99% confidence interval for the flux during the preflare period (see slant-lined area between MJD 54448 and 54503 in Figure 6.3) is between $1.55 \times 10^{-12}\,\gamma\,\mathrm{cm}^{-2}\,\mathrm{s}^{-1}$ and $5.05 \times 10^{-12}\,\gamma\,\mathrm{cm}^{-2}\,\mathrm{s}^{-1}$. M 87 was observed for an additional 17.2 hours of live time after the flare period and no significant photon excess was detected. The postflare dataset yielded a statistical significance of $1.5\,\sigma$ at the M 87 position. An upper limit of $2.1 \times 10^{-12}\,\gamma\,\mathrm{cm}^{-2}\,\mathrm{s}^{-1}$ at 99% C.L. (Helene, 1983) is established for the postflare period, corresponding to 1.4% of the Crab Nebula flux. Since M 87 was not detected after the flare even though the similar amount of observation yielded a detection before the flare, we calculated the C.L. with which we can report the postflare flux is lower than the preflare flux. This calculation is a continuation of the upper/lower flux limit derived in section 5.4 *Upper/lower flux limit calculation*.

6.2.2 Chance probability calculation

Given two integral flux measurements, the probability that measurement II is greater than measurement I corresponds to the confidence level for a statement on whether or not the difference between measurements I and II is a result of statistical fluctuations in the integral flux estimator.

Assuming a normal statistical probability density distribution for the integral flux estimator:

$$\begin{aligned} \frac{dP_I}{d\Phi_I} &= \frac{N_1}{\sqrt{2\pi}\sigma_{sI}} e^{-(\Phi_I - \bar{\phi_I})^2/2\sigma_{sI}^2} \\ \frac{dP_{II}}{d\Phi_{II}} &= \frac{N_2}{\sqrt{2\pi}\sigma_{sII}} e^{-(\Phi_{II} - \bar{\phi_{II}})^2/2\sigma_{sII}^2} \end{aligned} \tag{6.1}$$

where $\bar{\phi}$ is the central value of the integral flux, σ_s is one standard deviation of the integral flux, and $\int_{-\infty}^{\infty} dP/d\Phi\, d\Phi = 1$.

The probability of measurement II being greater than measurement I ($\Phi_{II} > \Phi_I$) can be calculated by integrating the product of the probability distribution of measurement I, and the probability distribution of measurement II in the range where $\Phi_{II} \geq \Phi_I$:

$$P = \int_{-\infty}^{\infty} \Big(\frac{dP_I}{d\Phi_I} \int_{\Phi_I}^{\infty} \frac{dP_{II}}{d\Phi_{II}}\, d\Phi_{II} \Big)\, d\Phi_I \tag{6.2}$$

This is shown graphically in Figure 6.4. Numerically, using trapezoidal rule:

$$P \simeq \sum_{i=-\infty}^{\infty} \{ \big(\frac{dP_I}{d\Phi_I}(i) + \frac{dP_I}{d\Phi_I}(i + \Delta i) \big) \frac{\Delta i}{2} \sum_{j=i}^{\infty} \big(\frac{dP_{II}}{d\Phi_{II}}(j) + \frac{dP_{II}}{d\Phi_{II}}(j + \Delta j) \big) \frac{\Delta j}{2} \} \tag{6.3}$$

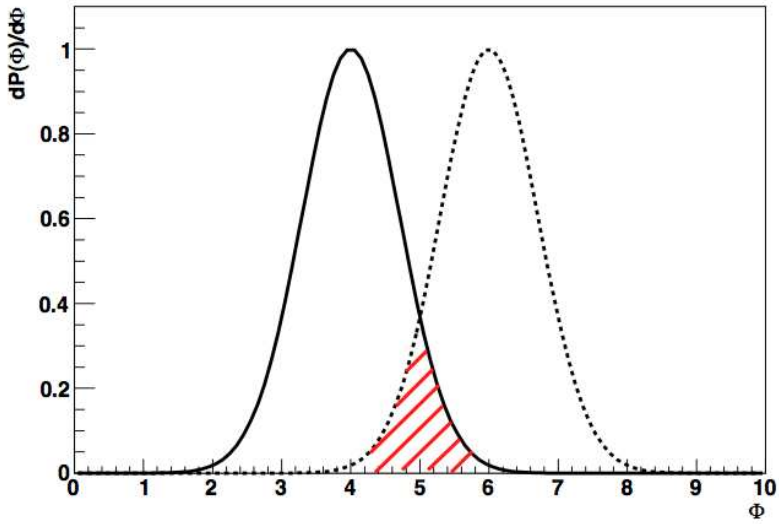

Figure 6.4. An example of two Gaussian probability distributions for the flux chance probability calculation. The chance probability of $\Phi_{II} \geq \Phi_I$ integral (equation 6.2) is the red-lined area between the two distribution.

6.2.2.1 Application to 2008 flare of M 87

Figure 6.5 shows the normal probability density distributions of the integral flux estimator during different periods on a graph. Table 6.1 shows the probabilities of the preflare, flare, and postflare fluxes are less than each other. The chance probabilities are calculated as described in equation 6.3.

The preflare flux is higher than the postflare flux at 99.8% C.L, suggesting that gamma rays could be attenuated after the flare by lower energy photons. An increase in less energetic photons can be due to interaction of the gamma-ray photon and/or of the same population of relativistic charged particles that produced the gamma-ray flare. For comparison, the flare flux is higher than the preflare flux at 99.95% C.L.

Price et al. (2011) searched for variability in the 2008 dataset presented here using a Haar wavelet analysis. Due to the uneven data sampling (no observations during full moon, bad weather etc.), the wavelet analysis yielded a 99.987% C.L, a statistical significance of 3.82, that the gamma-ray flux differed between the first half of the data and the second half.

The 2009 flux is compared to the pre/postflare flux in 2008 to see whether the gamma-ray

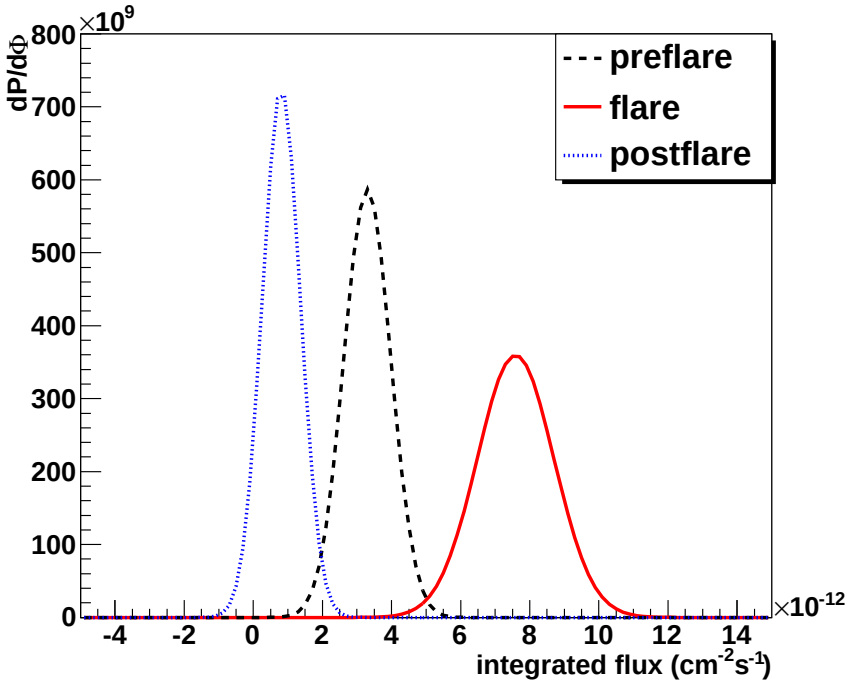

Figure 6.5. Integral flux above 250 GeV probability density distributions of M 87 in 2008 preflare, flare, and postflare periods.

Table 6.1. Chance probabilities of the difference in M 87 2008 flux measurements are due to statistical fluctuations.

period	chance probability (%) $<$ preflare flux	chance probability (%) $<$ postflare
preflare	—	0.23
flare	0.05	$\sim 10^{-6}$ (negligible)

flux level returns to preflare level. The 2009 flux is below the 2008 preflare flux at the 98.5% C.L., but above the 2008 postflare flux at the 87.6% C.L. No concrete conclusion can be drawn. All of the calculations were performed under the assumption of a constant power-law spectral index of 2.50.

6.2.3 2010 April flare

In February 2010, the MAGIC Collaboration reported increased M 87 activity with more than 10% of the Crab Nebula flux on February 9th (Mariotti, 2010a). At that time, VERITAS observations were hampered by bad weather conditions, but M 87 was detected at a normal state two nights after the MAGIC alert.

In April 2010, VERITAS recorded flaring activities in M 87 for several days (Ong & Mariotti, 2010). Figure 6.6 shows the nightly flux light curve. The flaring episode began with a flux increase during the nights of April 5th and 6th (MJD 55291 - 55292), reaching 10% of the Crab Nebula flux on April 8 (MJD 55294). The following 3 nights M 87 was observed for more than 5 hours each night. The average flux from April 9th and 10th (MJD 55295 - 55296) is 15% of the Crab Nebula flux, and the average from April 11th (MJD 55297) is 5%. VERITAS continued to monitor M 87 for 2 hours each night from April 12 to 15 when the flux level returned to a few percent of the Crab Nebula flux. Figure 6.7 shows the detailed run-by-run flux recorded by VERITAS around the flare. Each run is a 20-minute duration observation.

Since the 2010 flare observation is much more intense than the 2008 flare observation, the wavelet analysis described by (Price et al., 2011) can be utilized to search the data for short timescale variability. A peak of $5.9\,\sigma$ is obtained for day-scale variability between April 10th and 11th. The wavelet analysis showed a confidence level of 99.999 % ($4.4\,\sigma$) for night-to-night variability in the entire dataset. Even shorter time scale variability was also investigated. Using data taken from April 9th and 10th (MJD 55295 and 55296) when maximal activity occurred, we searched for run-by-run variability within each night. On April 9th, 15 runs were taken in total and a constant flux fit yielded a χ^2/dof of 9.3/14 and a corresponding χ^2 probability of 80.9%. On April 10th, 21 runs were taken and the constant flux fit gave a χ^2/dof of 19.8/20 and a corresponding χ^2 probability of 47.2%. To further investigate variability within one night of observation, the wavelet analysis, described by Price et al. (2011), is applied to the April 9th and 10th datasets. The highest confidence level for the April 9th dataset, obtained for 80-minute time scale variability, is only 86.2 % ($1.5\,\sigma$).

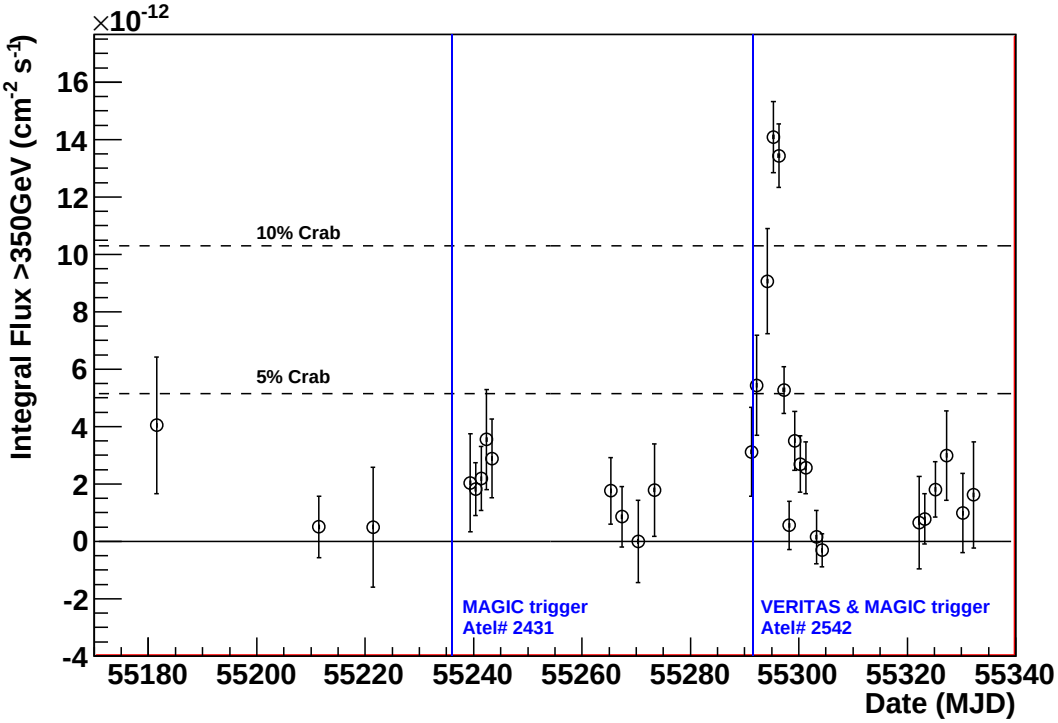

Figure 6.6. M 87 nightly flux recorded by VERITAS in 2010. Clear evidence of flaring activity is seen during a few nights in April 2010 (MJD 55291 - 55298). Trigger alerts sent by MAGIC on February 10th (MJD 55237) (Mariotti, 2010a) and by VERITAS and MAGIC on April 9th (MJD 55295) (Ong & Mariotti, 2010) are indicated by vertical lines. The average flux of each flare night exceeds 10% of the Crab Nebula flux, but individual 20-min observations during the flare nights reach 20% of the Crab Nebula flux (shown in Figure 6.7). A constant power-law spectral index of -2.5 is assumed for the flux calculation of the light curve.

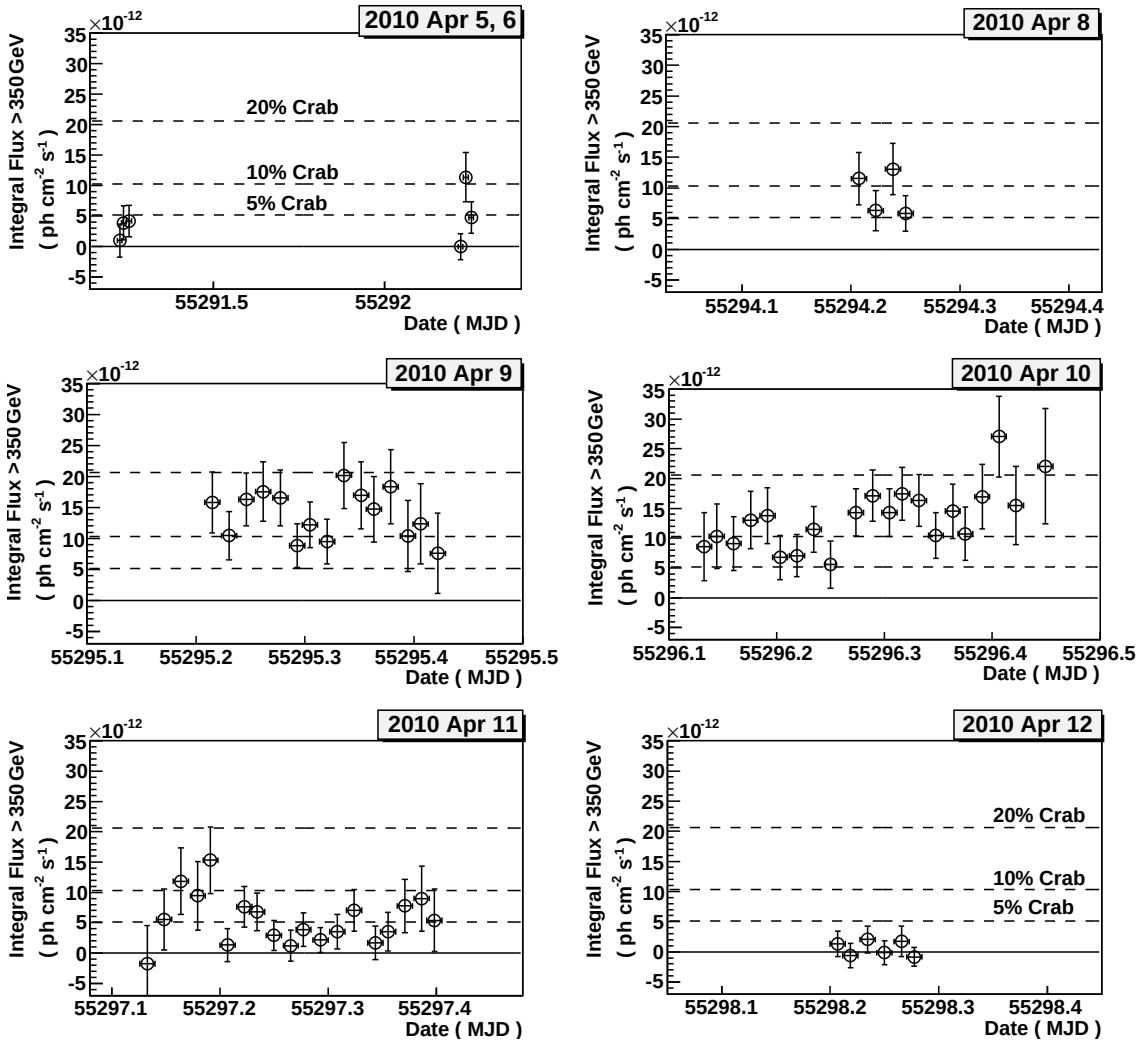

Figure 6.7. VERITAS run-by-run light curve (20-minute runs) of M 87 during the flare period between April 5 and April 12 (MJD 55291 - 55298). The flux scale is the same for all 6 panels, and dashed lines indicating 5%, 10%, and 20% of the Crab Nebula flux are included. Observations during the strong flare were conducted up to high zenith angles which reduces the sensitivity/statistics. Therefore the data points taken at the end of April 10th and the beginning of April 11th have larger error bars. A constant power-law spectral index of -2.5 is assumed for the flux calculation of the light curve.

The highest confidence level for the April 10th dataset is 97.5 % (2.2 σ), for 160-minute time scale variability. This search for intranight variability remains inconclusive.

To give a definitive timescale of the flare in order to constrain the size of the VHE emission region, an exponential function of the form $\Phi = p_0\, e^{(t-55290)/p_1}$ is used to define the time scales of the flare. For the days leading to the maximum flux (between MJD 55291 and 55295, April 5th and 9th), the minimal χ^2/dof of 0.3/2 is obtained for $p_1 = 2.87$ days. The error bars of the parameters p_0 and p_1 are determined by finding the parameter ranges with χ^2 between $\chi^2_{\rm min}$ and $\chi^2_{\rm min} + 2.30$ where $\chi^2_{\rm min}$ is the smallest χ^2 value. The same χ^2 calculation is repeated for data from the peak flux and afterwards. The details are presented in Table 6.2. For the period between MJD 55296 and 55301 (April 10th and 15th), the exponential decay time is $1.12^{+0.31}_{-0.26}$ days. An even shorter decay time of $0.90^{+0.22}_{-0.15}$ days is obtained by restraining the fit to the period between MJD 55296 and 55298 (April 10th to 12th). To investigate the possibility of a second component of the flare between MJD 55299 and 55301, a constant-flux fit is applied to data points between MJD 55298 and 55304 (April 12th to 18th). The χ^2/dof of the constant-flux fit is 9.6/4 with a corresponding χ^2 probability of 0.05. While the constant-flux hypothesis does not result in a high confidence level, there is no compelling evidence to confirm a second separated component of the flare around MJD 55299 to 55301 (April 13th to 15th). Figure 6.8 shows the χ^2 minimization results on the April light curve.

This time constraint gives a new lower limit on the emission region size using the exponential decay time: $R \leq R_{var} = \delta c \Delta t = 2.3\delta \times 10^{15}\,{\rm cm} \approx 1.3\delta R_s$, where R_s is the Schwarzschild radius of the M 87 black hole and δ is the relativistic Doppler factor. The Schwarzschild radius is calculated from the black hole mass. Using a black hole mass of $6.2\times10^9 M_\odot$ (scaled from Gebhardt et al. (2011) to the distance used here), the Schwarzschild radius $R_s = 2GM_{BH}/c^2 \approx 1.8 \times 10^{15}\,{\rm cm}$. Since the M 87 jet is misaligned, the relativistic

Table 6.2. M 87 2010 April flare light curve time scale fitting parameters via χ^2 minimization (fit function $\Phi = p_0\, e^{(t-55290)/p_1}$).

period [MJD]	χ^2/dof	χ^2 probability	p_0 [cm^{-2} s^{-1}]	p_1 [days]
55291-55296	0.3/2	0.88	$2.20^{+1.86}_{-1.34} \times 10^{-12}$	$2.87^{+1.65}_{-0.99}$
55296-55304	23.7/6	6.0×10^{-4}	$3.61^{+17.64}_{-2.61} \times 10^{-9}$	-($1.12^{+0.31}_{-0.26}$)
55296-55298	2.1/1	0.15	$1.48^{+4.62}_{-1.32} \times 10^{-8}$	-($0.90^{+0.22}_{-0.15}$)

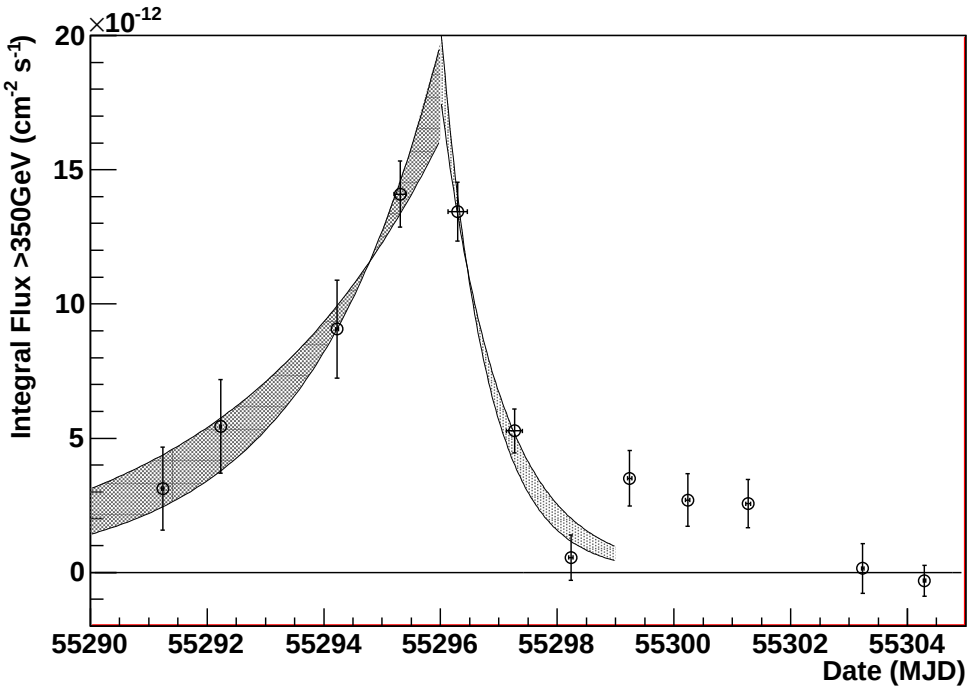

Figure 6.8. Fits to the M 87 2010 April flare light curve. The exponential time scale is $2.88^{+0.77}_{-0.60}$ days for rising flux and $0.88^{+0.15}_{-0.10}$ days for falling flux between MJD 55296 and 55298. The fit errors are shown as shaded regions.

Doppler factor δ is unlikely to be large, more likely on the order of 10 or less. This means the VHE emission region is very close to the central supermassive blackhole.

6.2.4 Spectral analysis

The differential energy spectrum of M 87 is consistent with a power-law distribution $dN/dE = \Phi_0(E/\mathrm{TeV})^{-\Gamma}$. Table 6.3 lists the flux normalization constant Φ_0 and the spectral index Γ observed by VERITAS, for each year's dataset and subset when flaring activity occurred. The spectral data points and fits are presented in Figure 6.9. We were not able to provide a spectrum for the 2009 data due to low photon statistics.

Detailed spectral study has been done in BL Lac objects, and in the case of Mrk 421 it has shown clear flux-index correlation (Krennrich et al., 2002). The Mrk 421 flux-index correlation can be interpreted as the high energy peak of the SED shifting to higher energies to explain the flare spectrum is harder than the non-flare spectrum.

Table 6.3. Power-law fit parameters of the VHE spectra of M 87 between 2007 and 2010.

Dataset	MJD date $[10^{-13}\,\mathrm{cm}^{-2}\,\mathrm{s}^{-1}\,\mathrm{TeV}^{-1}]$	Φ_0	Γ	χ^2/dof
2007 overall	54143 - 54208	7.4 ± 1.3	2.31 ± 0.17	3.0/4
2008 overall	54448 - 54588	5.2 ± 0.9	2.49 ± 0.19	3.1/4
2008 flare	54505 - 54509	15.9 ± 2.9	2.40 ± 0.21	3.9/4
2008 preflare	54448 - 54503	5.6 ± 1.5	2.49 ± 0.26	1.3/4
2010 overall	55181 - 55332	18.0 ± 0.9	2.32 ± 0.06	7.4/5
2010 rising	55291 - 55294	19.2 ± 4.2	2.60 ± 0.31	4.1/4
2010 peak	55295 - 55296	47.1 ± 2.9	2.19 ± 0.07	4.3/5
2010 falling	55297 - 55301	11.0 ± 1.6	2.62 ± 0.18	5.2/4

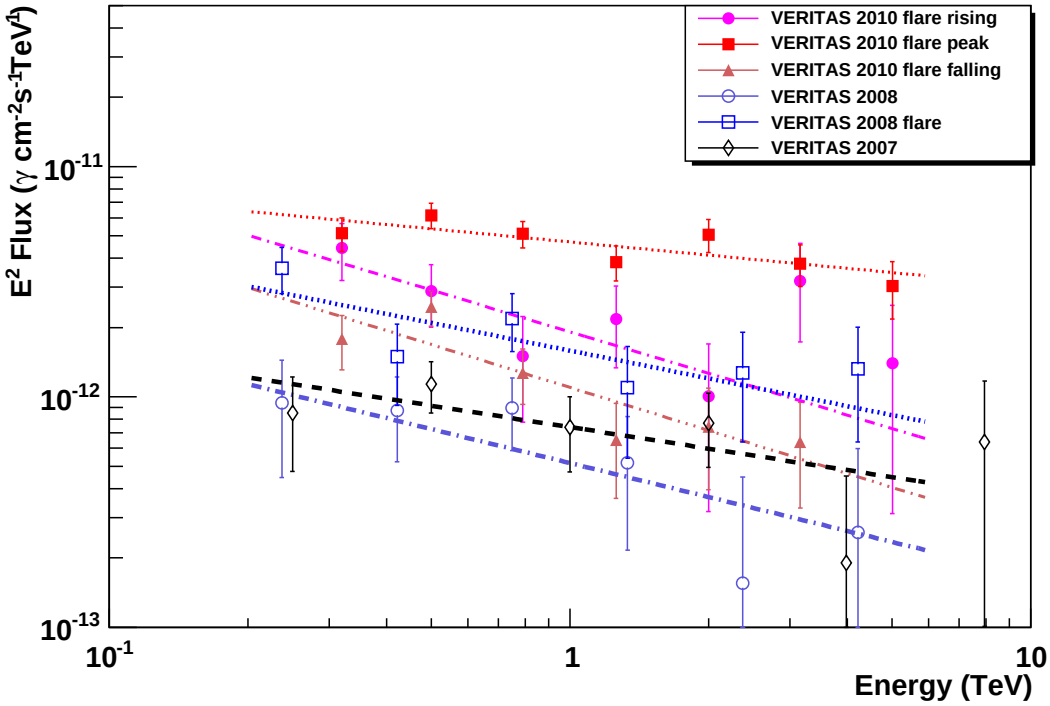

Figure 6.9. Spectral measurements of M 87 by the VERITAS array from 2007 to 2010. Flare periods spectra are analyzed separately from non-flare periods as shown in the legend. The flux is multiplied by energy squared (vertical axis) in order to highlight any differences between the datasets.

The same flux-index correlation study is detailed here. No significant difference in photon index or photon energy distribution is found between the flare and preflare states in 2008. For the 2010 data, the spectral indices of different periods are approximately $2\,\sigma$ away from each other. A constant fit to the spectral index (Γ) versus flux normalization(Φ_0) of the 2010 spectra yields a χ^2 probability of 0.045. A linear fit of the form $\Gamma = p_0 + p_1 \log_{10}\Phi_0$ yields a χ^2 probability of 0.669, with the parameter $p_1 = -0.72 \pm 0.30$, which is about $2.5\,\sigma$ away from zero. Although the fit suggests a possible correlation between the spectral index and log of the flux normalization, the data do not provide any definitive evidence for spectral variability during the 2010 flaring episode.

Figure 6.10 shows the spectral index plotted against flux normalization, including archival VHE gamma-ray spectra from 2004 onwards (Aharonian et al., 2006a; Acciari et al., 2008; Albert et al., 2008a; Acciari et al., 2009a, 2010). The measurement by HESS in 2005 is excluded from the fit due to possible contamination from the HST-1 flare which maybe of a different nature. Using all of the high/low-state spectra available since 2004, a constant-flux fit yields a χ^2 probability of 0.258, while a linear fit of the form $\Gamma = p_0 + p_1 \times \log 10\,\Phi_0$ yields a χ^2 probability of 0.515 with $p_1 = -0.268 \pm 0.134$. Evidence for spectral hardening is not significant when using all high/low state spectra since 2004.

The spectral data presented here provide constraints on the modelling of the type of particles being accelerated and the acceleration mechanisms which can produce the observed gamma rays. The current models and the spectral measurements are discussed in Chapter 8 *Modelling and Interpretation* where the gamma-ray spectra are combined with spectra from other wavelengths to compare with model predictions.

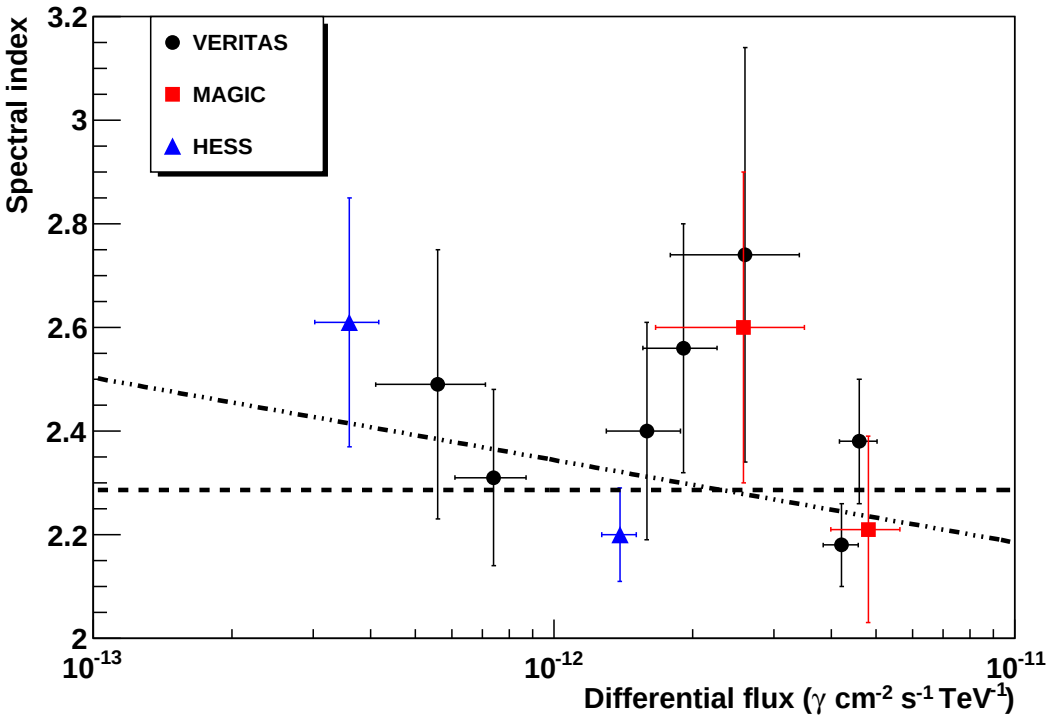

Figure 6.10. Spectral index vs. flux normalization constant using M 87 spectra measured by VERITAS and archival spectra from other experiments taken in 2004 onwards. The dashed line represents a constant fit with probability 0.258; the dashed-dotted line represents a linear fit of form $p_0 + p_1 \log_{10} x$ with probability 0.515.

CHAPTER 7

M 87 MULTIWAVELENGTH CAMPAIGN

Figure 7.1 displays the VHE gamma-ray flux yearly averages and upper limit reported since 1998 (Aharonian et al., 2003; Le Bohec et al., 2004; Aharonian et al., 2006a; Acciari et al., 2008; Albert et al., 2008a; Acciari et al., 2010), with shaded regions to indicate flaring activities, X-ray flux measured by the Chandra X-ray Observatory (Harris et al., 2009) and the All Sky Monitor onboard the Rossi X-ray Timing Explorer (ASM/RXTE). The ASM/RXTE light curve is averaged weekly for better presentation and the data is provided by the ASM/RXTE teams at MIT and at the RXTE SOF and GOF at NASA's GSFC. A discussion of the multiwavelength observations of M 87 in the context of VHE gamma-ray flares follows.

7.1 X-ray observations

7.1.1 Chandra X-ray Observatory

Figure 7.1 shows that for the 2005 flare detected by H.E.S.S., the HST-1 knot was at a historical maximum, while for the 2008 flare detected by VERITAS, it was the nucleus. The 2010 data from Chandra are not yet publicly available.

At the time of the 2008 flare detected by VERITAS, Chandra measured the nucleus X-ray flux at a historical maximum, at $4.1\,\sigma$ above the mean nucleus flux between 2000 and 2009, and exceeding the flux from the HST-1 knot (see Figure 6.3 and 7.1) (Harris et al., 2009). The peak nucleus X-ray flux measured by Chandra during the observation period of VERITAS was 2.3 times the average nucleus X-ray flux, with the average calculated excluding this flare data point, while the HST-1 knot X-ray flux during this period fluctuated $\pm 10\%$ from the average and is relatively steady when compared to the nucleus emission.

Figure 7.2 shows the light curves between 2007 and 2009 observed by VERITAS and the X-ray flux measured by Chandra for the nucleus and the knot HST-1, along with the fractional change per year (fpy) of the Chandra X-ray flux. Fpy is first presented in Harris et al. (2009) in order to analyze and compare time scales. The definition of fpy is repeated below (Harris et al., 2009).

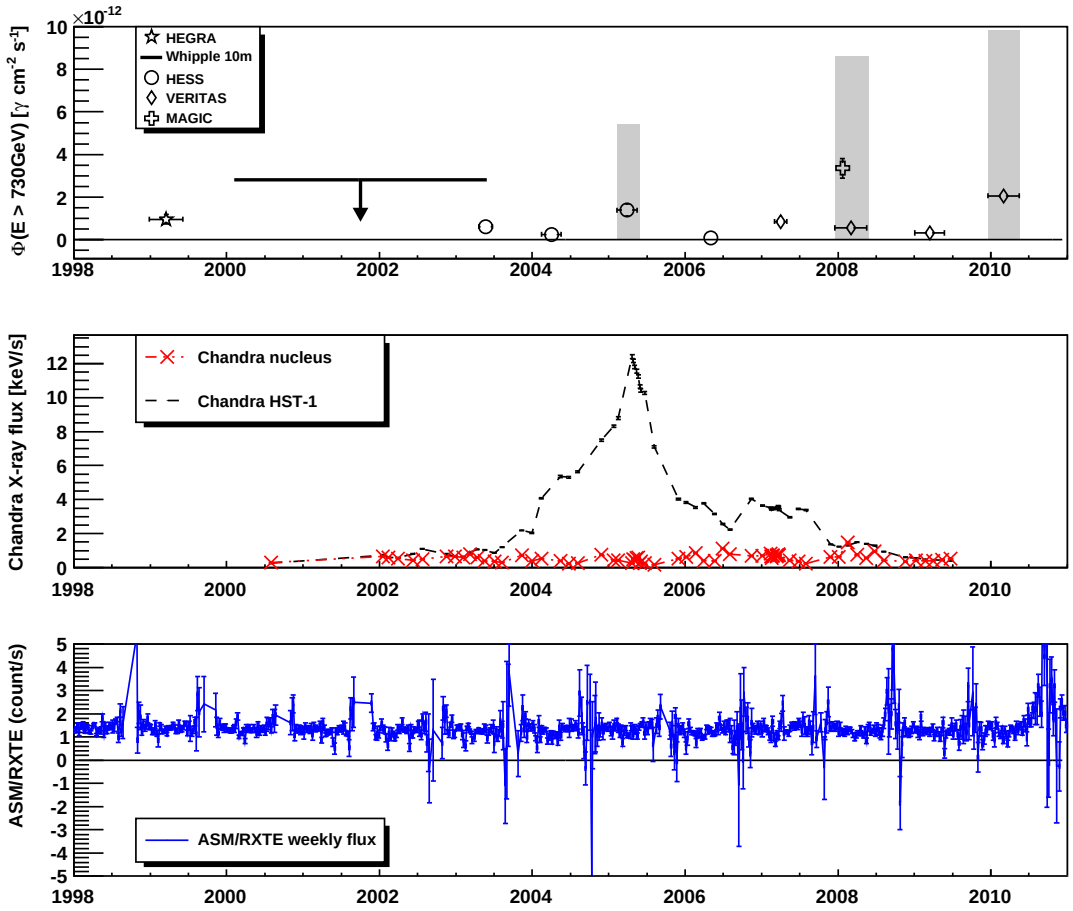

Figure 7.1. Twelve years of VHE gamma-ray flux (Aharonian et al., 2003, 2006a; Acciari et al., 2008; Albert et al., 2008a; Acciari et al., 2010) and X-ray flux (Harris et al., 2009) of M 87. The VHE gamma-ray flux is for energy >730 GeV due to the original flux scale used in the HEGRA paper. Grey areas represent the range of variable VHE fluxes observed that year to give a more accurate picture of the flux level of M 87. ASM/RXTE results provided by the ASM/RXTE teams at MIT and at the RXTE SOF and GOF at NASA's GSFC.

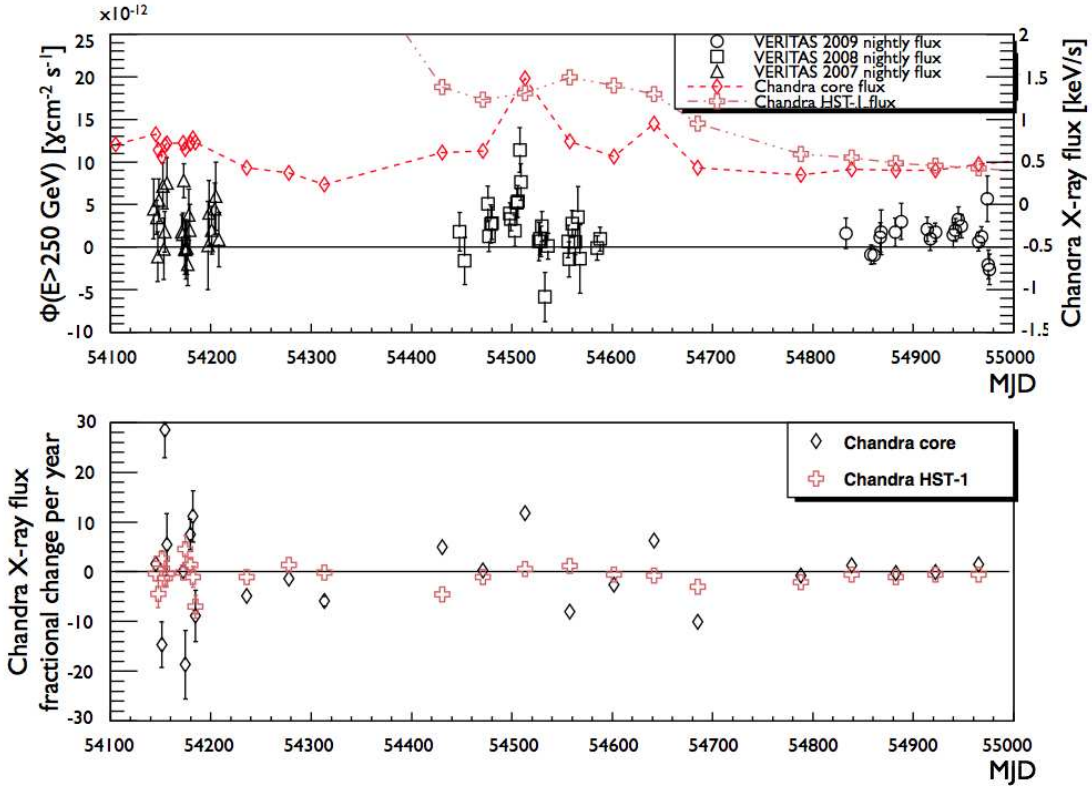

Figure 7.2. VERITAS nightly light curve and Chandra X-ray flux of M 87 between 2007 and 2009. *Upper panel:* VERITAS night-by-night VHE gamma-ray flux and Chandra X-ray flux from the nucleus and from the HST-1 knot of M 87 from 2007 to 2009 (Harris et al., 2009). *Lower panel:* Chandra X-ray flux fractional change per year, see text for definition (Harris et al., 2009).

$$\mathrm{fpy} = \frac{\mathrm{I_2 - I_1}}{\mathrm{I_i \Delta t}} \tag{7.1}$$

$$\sigma_{\mathrm{fpy}} = \frac{1}{\Delta t} \times \frac{I_j}{I_i} \times \sqrt{(\frac{\sigma_1}{I_1})^2 + (\frac{\sigma_2}{I_2})^2} \tag{7.2}$$

where I is the X-ray intensity measured by Chandra and Δt is the time between the two intensity measurements in units of year. If the X-ray intensity is increasing (i.e., $I_2 > I_1$), then $i = 1, j = 2$; if the X-ray intensity is decreasing ($I_2 < I_1$), then $i = 2, j = 1$.

Around the 2008 VHE gamma-ray flare period, the Chandra nucleus fpy is more variable than that of the Chandra HST-1 fpy measurement. The nucleus flux increased by over 100% when compared to the previous flux ($\delta I/I_1$) around the VHE gamma-ray flare, while the HST-1 flux increased by no more than 15% after the VHE gamma-ray flare.

When M 87 is observed to be stable in VHE gamma rays, the Chandra fpy for both the nucleus and HST-1 appear close to 0. The exception of large fpy observed in 2007 while the X-ray flux appeared to be stable and without a corresponding VHE gamma-ray flare. This may be due to the short amount of time between successive observations. Comparison of the flux level shows the nucleus varied by no more than 25% during the 2007 VHE gamma-ray observation period, and the HST-1 flux varied by less than 5%. During the 2009 observation period, Chandra took a flux measurement every 40 - 50 days. The HST-1 flux measured by Chandra was steadily declining at a rate of 5 - 10%. The nucleus flux, however, was mostly increasing by as much as 18%. The lack of VHE activity during this period suggests a possible association between VHE flares and significant changes in the X-ray flux such as the doubling of flux seen in 2008. Harris et al. (2009) suggested that variability in the nucleus may be characterized as "flickering" due to the large fpy observed with short sampling times, where as HST-1 flared at a much larger amplitude over a longer time scale (e.g., 2005 flare, Figure 7.1). A similar analysis of fpy is not performed for the 2005 flare due to contamination from the HST-1 flare in the Chandra data.

7.1.2 All Sky Monitor onboard the Rossi X-ray Timing Explorer

The All-Sky Monitor (ASM) on the Rossi X-ray Timing Explorer (RXTE) has provided daily monitoring of M 87 in the energy range $1.5 - 12$ keV since 1996 (Levine et al., 1996). M 87 has also been observed by the two pointed instruments onboard the RXTE, the Proportional Counter Array and the High Energy X-ray Timing Experiment. The pointed observations were taken between December 1997 and February 1998. Only thermal emission is detected from the intracluster medium of the Virgo Cluster, while upper limit

is established for the non-thermal emission from M 87 (Reynolds et al., 1999). The results used here are provided by the ASM/RXTE teams at MIT and at the RXTE SOF and GOF at NASA's GSFC.

Figure 7.3 shows the daily light curve from ASM/RXTE along with the VERITAS light curve between 2007 and 2010. Unlike Chandra, ASM/RXTE cannot resolve the M 87 jet. Figure 7.4 shows the daily flux measured by VERITAS versus ASM/RXTE between 2007 and 2010 and it does not show any correlation. It should also be noted that ASM/RXTE did not detect the HST-1 historical flare in 2005 reported by Chandra.

Various modulations of ASM/RXTE light curves have been reported previously by Wen et al. (2006) in their search for periodicities in ASM/RXTE data. These modulations are related to the satellite orbit around the Earth or the Earth's orbit around the Sun.

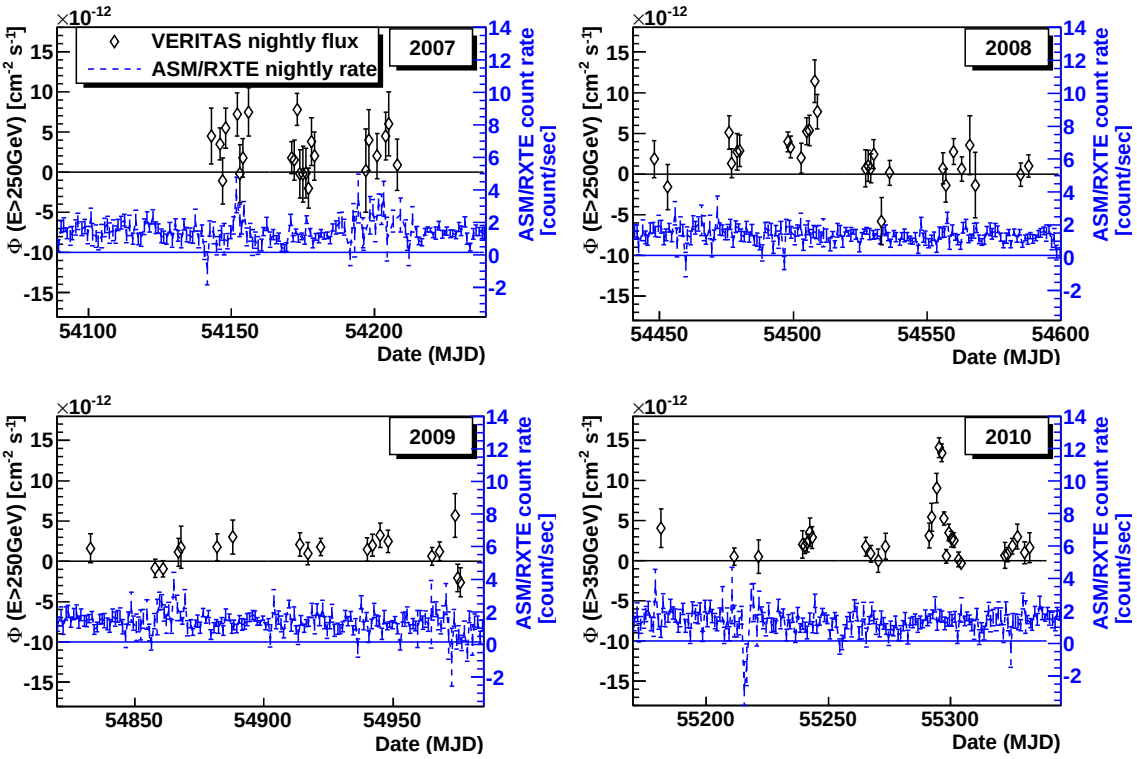

Figure 7.3. VERITAS and ASM/RXTE nightly light curve of M 87. Each panel represents an observing season for the VERITAS array. Both the VERITAS light curve of M 87 and the ASM/RXTE daily light curve are shown. No correlated activity appears between data from the ASM/RXTE and VERITAS.

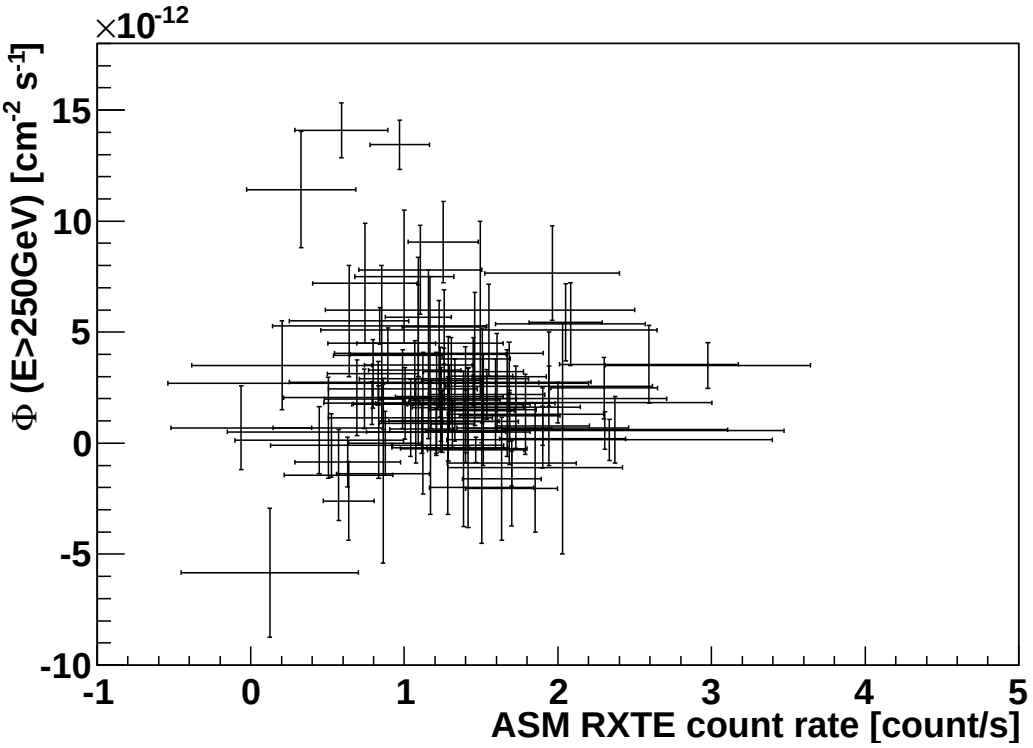

Figure 7.4. VERITAS versus ASM/RXTE nightly light curve of M 87. Each data point is the daily flux observed by VERITAS and ASM/RXTE from 2007 to 2010. No correlation is seen between X-ray (ASM) and VHE gamma rays (VERITAS).

Benlloch et al. (2001) also observed fluctuations of the ASM count rate in correlation with the angular distance to the Sun due to solar X-ray scattering off of the ASM collimators and onto the detectors. Figure 7.5 shows the M 87 ASM light curve summed weekly and each year between 1996 and 2010 is represented in a different color. In the second half of the year the count rates are erratic due to M 87 proximity to the Sun. The data are averaged into weekly bins (7-day) using the measurement uncertainty as the weight ($1/\sigma^2$).

$$w_i = \frac{1}{\sigma_i^2}$$
$$S = \frac{\sum w_i s_i}{\sum w_i}$$
$$\sigma = \frac{1}{\sqrt{\sum w_i}}$$

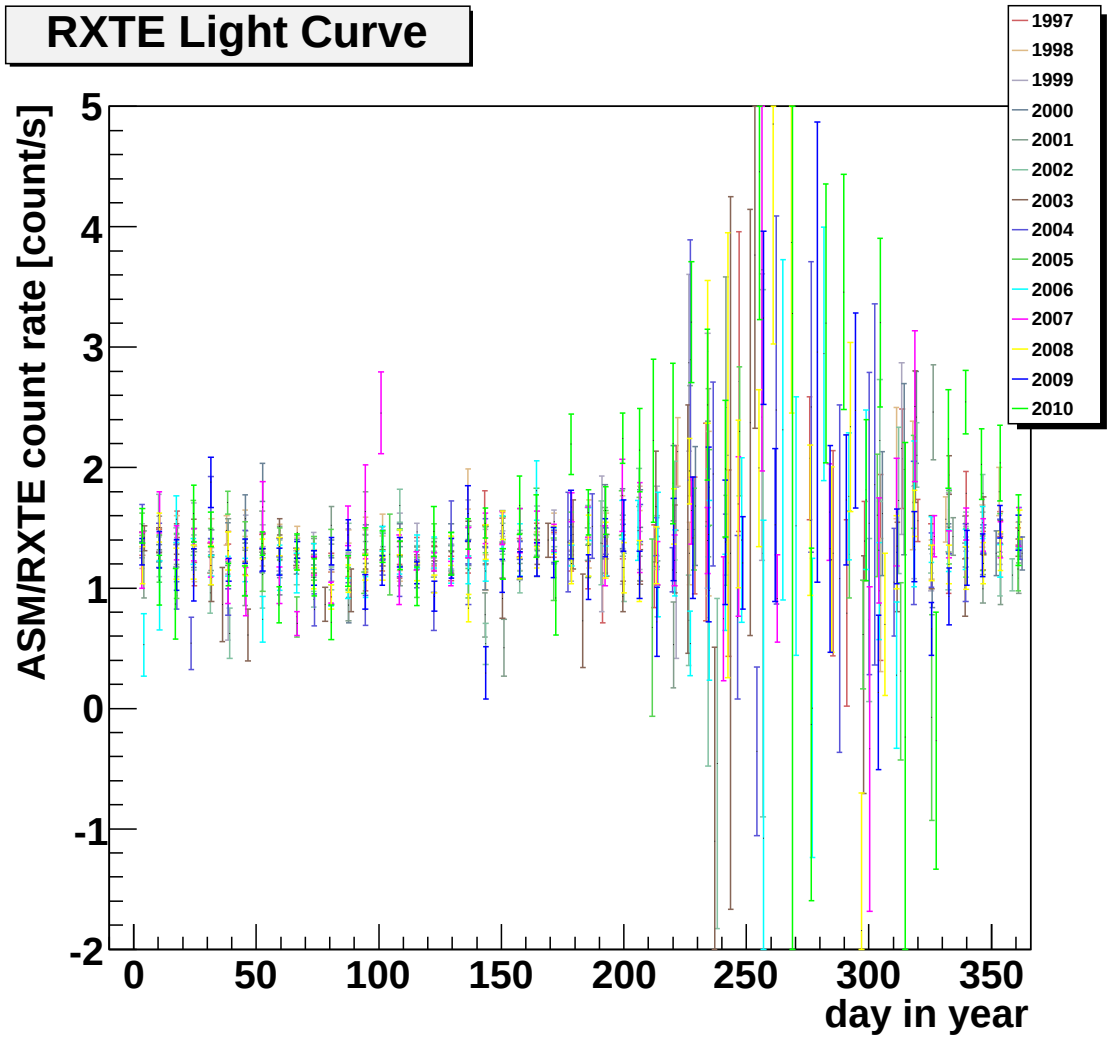

Figure 7.5. ASM/RXTE weekly count rate of M 87. Each year is represented by a different color. Erratic count rate is seen towards the second half of the year due to M 87 proximity to the Sun.

While no day-to-day correlated activity between ASM/RXTE data and VERITAS data is seen, a gamma/X-ray correlation on 6-month time scale (between January and June) is first presented by Acciari et al. (2008) using the 2007 VERITAS data and 10 years of archival VHE gamma-ray data. The 6-month average is selected to match TeV observation time frame and to minimize the effect of the annual modulation. In addition, data binning from year to year were kept consistent as to minimize the variability that could be induced by the sensitivity of the separation to the Sun. Acciari et al. (2008) fitted both linear and quadratic relations to a gamma-ray/X-ray flux plot similar to Figure 7.6 but with data up to 2007 only. Both fits have χ^2/dof less than 1. Shorter time scale correlation with 5-day interval binning of contemporaneous observations between VERITAS and ASM/RXTE was also tested by Acciari et al. (2008) and a positive correlation was found at 82% confidence level.

Figure 7.6 reproduces the year-scale correlation by taking all available VHE gamma-ray data from 1998 to 2010 and the first 5-month average of ASM/RXTE data (Aharonian et al., 2003; Götting, 2006; Aharonian et al., 2006a; Acciari et al., 2008, 2010). The 5-month average is calculated instead of the original 6-month average due to sensitivity to the ASM/RXTE count rate annual modulation caused by M 87 proximity to the Sun (private communication with C. C. Cheung, D. E. Harris, and L. Stawarz). The linear correlation, $p_0 \times (x - p_1)$, now has a χ^2/dof of 24/7 with the addition of 3 years of data. The quadratic fit, $p_0 \times (x - p_1)^2$, gives a χ^2/dof of 25/7. Both the HEGRA paper and the reanalysis point are presented in Figure 7.6 and the reanalysis data point is used in the fitting. The MAGIC 2008 flare data is excluded because only 14 days of observations were presented in Albert et al. (2008a). Even though the linear fit χ^2/dof is large, it should be noted that the fit parameter p_0, which represents the slope of VHE gamma rays versus ASM/RXTE X-ray photon counts, is $5.7\,\sigma$ away from 0. While this alone does not prove a correlation between VHE gamma rays and ASM/RXTE long-term X-ray monitoring, it is an indication of a possible long timescale correlation that is worth investigating.

The same year-scale correlation fitting procedure is repeated with the Chandra X-ray data. Since Chandra can resolve the HST-1 knot from the nucleus, both are presented in Figure 7.7 since both features had corresponding activities during VHE flares. The same linear and quadratic fits applied to the VHE gamma-ray flux versus Chandra nucleus flux gave a χ^2/dof of 21/5, while both fits to that of the Chandra HST-1 flux gave a χ^2/dof 24/5, see Table 7.1 for detailed results of the correlation fits. Since the 2005 flare data from

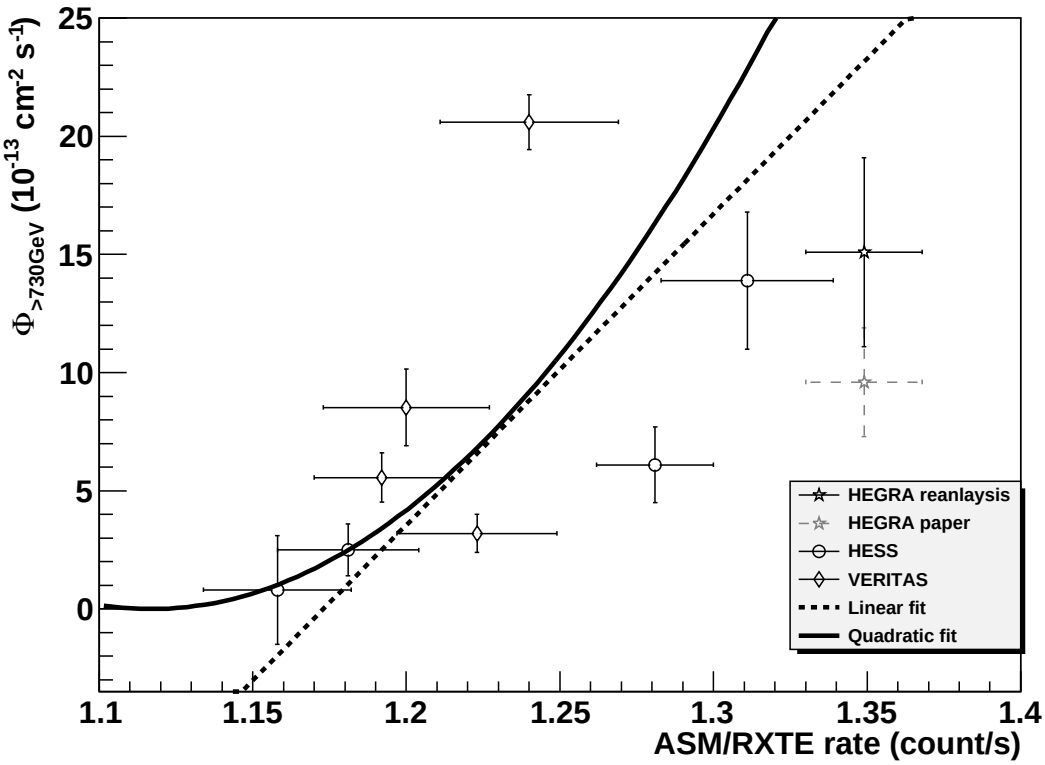

Figure 7.6. VHE gamma-ray flux (Aharonian et al., 2003; Götting, 2006; Aharonian et al., 2006a; Acciari et al., 2008, 2010) versus ASM/RXTE count rate averaged from the first 5 months of each year, along with linear and quadratic fits.

Chandra may have contamination from the HST-1 to the nucleus fluxes due to the historical maximum flare, the correlation fitting is repeated with the 2005 point excluded. Fitting the VHE gamma-ray flux versus Chandra HST-1 with either a linear or quadratic relations yielded zero results. The best fit is a constant where there is no correlation between VHE gamma-ray flux and Chandra HST-1 flux. Table 7.2 shows the detailed results of the linear and quadratic fit of VHE gamma-ray flux versus Chandra nucleus X-ray flux. The linear fit χ^2/dof is 6.27/4 and the quadratic fit χ^2/dof is 7.54/4, with the linear fit slope $2.99\,\sigma$ away from 0. This supports the claim that VHE gamma rays are from the nucleus region from contemporaneous flaring activities seen in 2008 between VHE gamma rays and Chandra X-ray from the nucleus.

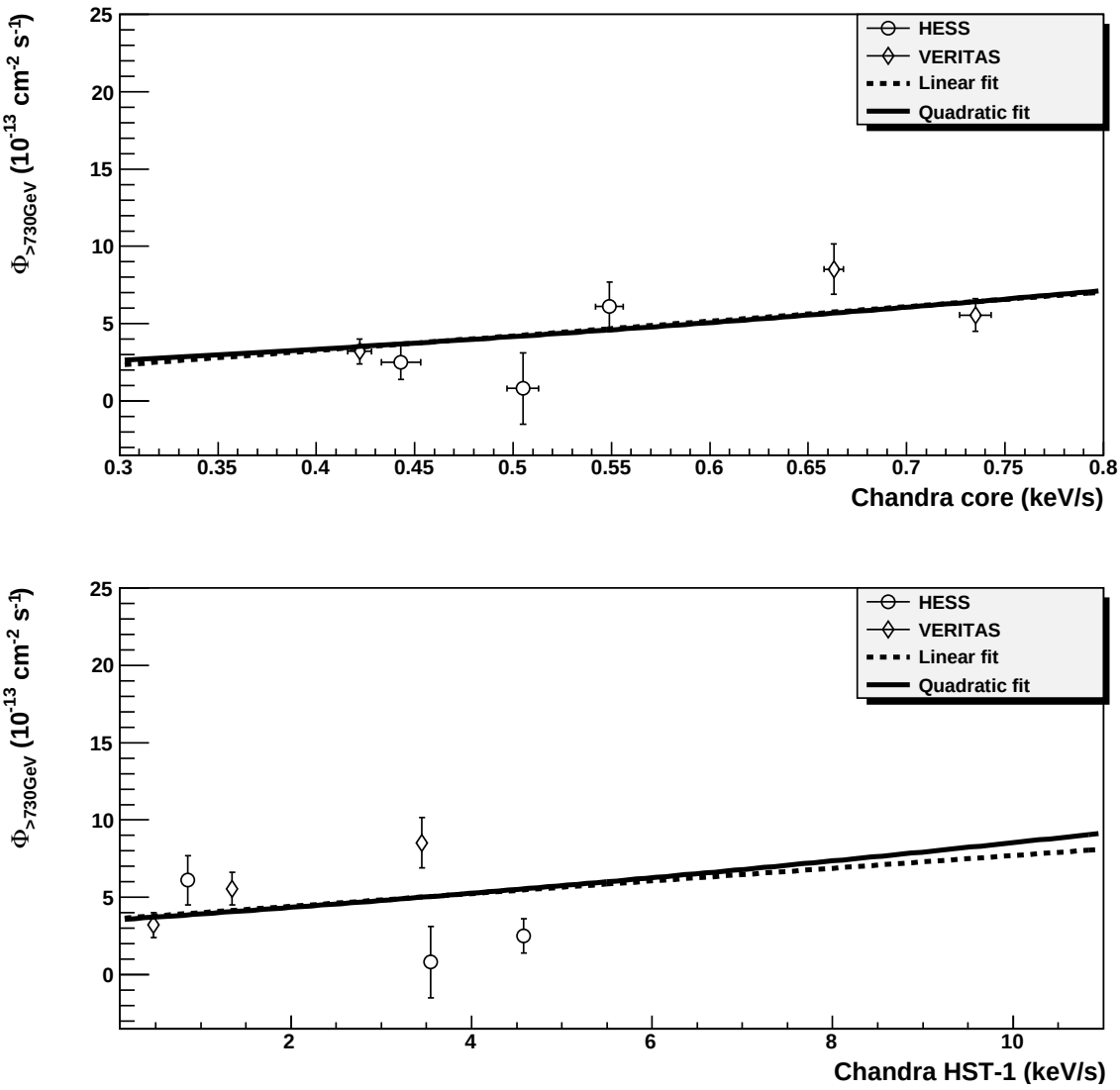

Figure 7.7. VHE gamma-ray flux (Aharonian et al., 2003; Götting, 2006; Aharonian et al., 2006a; Acciari et al., 2008, 2010) versus Chandra nucleus (upper panel) and HST-1 (lower panel) flux averaged from the first 5 months of each year, along with linear and quadratic fits.

Table 7.1. VHE gamma-ray/X-ray correlation fit parameters for linear ($p_0 \times (x - p_1)$) and quadratic ($p_0 \times (x - p_1)^2$).

X-ray	linear χ^2/dof	linear p_0	linear p_1
ASM/RXTE	24.2/7	131.60 ± 23.01	1.17 ± 0.01
Chandra nucleus	20.8/5	9.45 ± 3.75	0.05 ± 0.19
Chandra HST-1	23.9/5	0.41 ± 0.22	-8.77 ± 6.08
	quadratic χ^2/dof	quadratic p_0	quadratic p_1
ASM/RXTE	25.0/7	606.80 ± 268.20	-1.12 ± 0.03
Chandra nucleus	20.9/5	4.44 ± 3.60	0.47 ± 0.42
Chandra HST-1	23.2/5	0.01 ± 0.01	17.90 ± 10.00

Table 7.2. VHE gamma-ray/Chandra core X-ray correlation fit parameters for linear ($p_0 \times (x - p_1)$) and quadratic ($p_0 \times (x - p_1)^2$) but with HESS 2005 flare data point excluded due to possible contamination in Chandra data.

form	χ^2/dof	p_0	p_1
linear	6.27/4	11.36 ± 3.80	0.16 ± 0.13
quadratic	7.54/4	6.63 ± 4.48	0.26 ± 0.28

7.2 Other observations

In 2008, H.E.S.S., MAGIC, and VERITAS collaborated to provide the increased observation coverage of M 87 in coordination with Chandra X-ray observations. M 87 was observed for more than 50 nights and a total of 120 hours that resulted in the detection of flaring activity (Beilicke et al., 2008). This joint monitoring campaign coincided with the M 87 43 GHz movie project (Walker et al., 2009). M 87 was observed with the Very Large Baseline Array (VLBA) every three weeks in 2007 and more frequent observations in 2008 that coincided with the VHE flare timeline. Acciari et al. (2009a) showed the VHE flare coincided with a historical high X-ray flux from the nucleus observed by Chandra, and a continuous increase of 43 GHz radio flux from the nucleus (central region within 1.2 milli-arcseconds radius) up to two months following the VHE flare. The radio nucleus flux was up by 30% two months after the VHE flare when compared to the beginning of the flare, and up by 60% when compared to the 2007 average flux. The jet radio flux (region between 1.2 and 5.3 milli-arcseconds) appear constant throughout the two months during and after the VHE flare. Figure 7.8 shows the multiwavelength light curve from Acciari

et al. (2009a).

The chance probability of coincident VHE/X-ray/radio flares of this magnitude is less than 0.5% (Acciari et al., 2009a). The high-resolution imaging of radio telescopes, combined with VHE gamma-ray observations from ground-based instruments, have shown the first association between a VHE gamma-ray flare and an increase in radio flux coming from the jet collimation region that is less than $100\,R_s$ (Schwarzschild radius) from the black hole. Coupled with the VHE day-scale flaring size constraint from causality arguments (the VHE emitting region should be less than $5\delta R_S$ (Acciari et al., 2009a)), the relativistic Doppler factor δ is approximately 20.

This coincident multiwavelength coverage led to several modeling discussions of the joint VHE and radio light curves (see supplement of Acciari et al. (2009a)). In the next section 8 *Modelling and Interpretation*, these models are discussed in the context of the VERITAS observations and results.

After the launch of the *Fermi Gamma-ray Space Telescope* in the summer of 2008, Abdo et al. (2009b) reported the first 10-month observations of M 87 in the 200 MeV to over 30 GeV energy range. No variability was observed in the dataset which is taken between August 2008 and May 2009. Figure 7.2 shows that in 2009 both Chandra X-ray observations and VHE gamma-ray observation by VERITAS showed no variability in the M 87 light curves.

The joint multiwavelength monitoring campaign continues and in 2010 another flare was observed in VHE gamma rays (Ong & Mariotti, 2010). There were follow-up observations in MeV/GeV gamma rays, X-ray, optical, and radio, and the results are published in an upcoming joint publication (Abramowski et al., 2011).

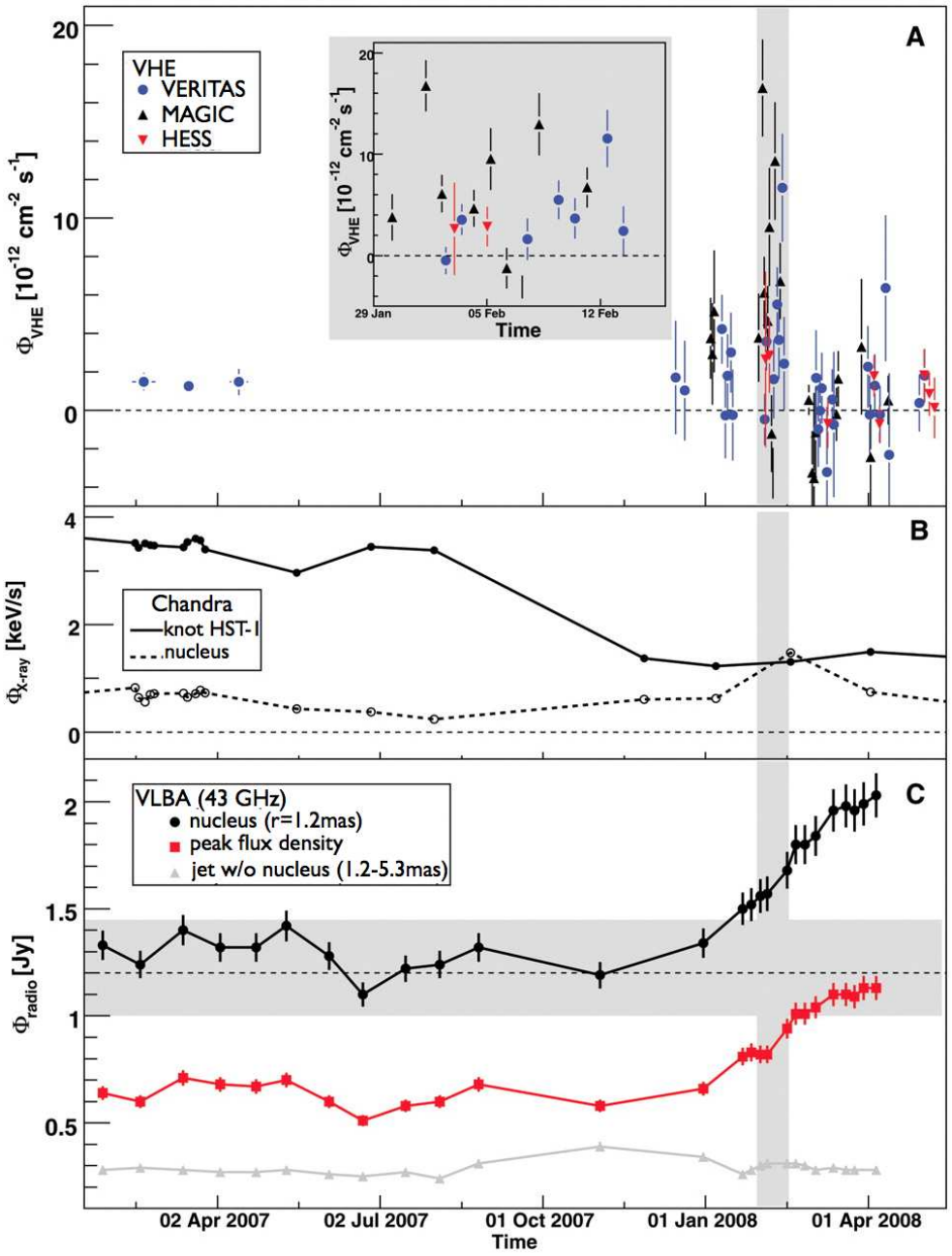

Figure 7.8. Multiwavelength light curves from 2007 to 2008 (Acciari et al., 2009a)(http://www.sciencemag.org/content/325/5939/444). Top panel (A) shows the VHE flux measured by VERITAS, MAGIC, and H.E.S.S., the inlay shows a close-up of the 2008 flare. The time frame of the inlay is shown in the grey region highlighted across all three panels. The middle panel (B) shows the X-ray flux from the nucleus and the HST-1 knot from Chandra, the the 2008 VHE flare coinciding the flux increase from the nucleus in X-ray. The bottom panel (C) shows the 43 GHz radio flux from the nucleus and the jet. The radio flux from the nucleus increases up to two months after the VHE flare when the radio monitoring project ended.

CHAPTER 8

MODELLING AND INTERPRETATION

Modeling of the particle acceleration yields several possible VHE emission origins. Even though the VHE gamma-ray technique cannot resolve individual features of M 87, the rapid variability observed (Aharonian et al., 2006a; Albert et al., 2008a; Acciari et al., 2009a, 2010) has constrained the size of the VHE emission region to $< 1.3\,\delta\,\mathrm{R_s}$ where δ is the relativistic Doppler factor and R_s the Schwarzschild radius of the M 87 black hole ($\mathrm{R}_s \sim 10^{15}$cm). Radio observations have shown evidence that charged particles are accelerated in the immediate vicinity of the black hole closer than $100\,R_s$ (Acciari et al., 2009a). Combining these radio observations with the size constraint from VHE data, we can in addition place a limit on the relativistic Doppler factor δ in the modelling of the spectral energy distribution. The compactness of the particle accelerators operating in the vicinity of the supermassive black hole and the absence of a significant cut-off in the spectrum imply that the particle acceleration mechanism is highly efficient.

8.1 Large-scale models

Baltz et al. (2000) modelled gamma-ray production in M 87 by dark matter particles annihilation. The resultant gamma-ray fluxes estimated by exploring the parameter space of the minimal supersymmetric standard model will be mostly below the $3\,\sigma$ detection limit estimated from sensitivity of this generation of IACTs (e.g., H.E.S.S. and VERITAS etc.). This sensitivity issue improves if the neutralino particles clump within the dark matter halo of M 87, since gamma-ray flux is proportional to the square of the neutralino density.

Biermann et al. (2000) traced back the then 14 published cosmic-ray events above 10^{20} eV, using their simple model of a magnetic Galactic wind that is analogous to the Solar wind, and found that all events originated from within 20° of the Virgo cluster, where M 87 resides. Pfrommer & Enßlin (2003) proposed a scenario where gamma rays are produced by pion decay from cosmic-ray proton interactions with the interstellar medium of M 87. The cosmic-ray interaction model predicts steady gamma-ray emission.

Based on the multiwavelength correlated activities and variability studies, the favored candidate for VHE emission is the small-scale (subarcsecond) jet region and large-scale models are unlikely the dominant processes for gamma-ray production in M 87.

8.2 Hadronic models

In the Synchrotron-Proton Blazar (SPB) model (Mücke & Protheroe, 2000), protons and electrons are accelerated together in a highly magnetized environment. The relativistic electrons then radiate synchrotron emission, and these photons are subsequently the target radiation field for proton-photon interactions which produce mesons and muons. The protons, mesons, and muons produce TeV emission via synchrotron radiation.

The SPB model is first demonstrated to be able to reproduce the double-humped feature in the SED of blazars by Mücke & Protheroe (2001). Using the SED of the blazar Markarian 501 during the 1997 flare, in particular the observed synchrotron radiation for the modelling of the target photon field, the TeV emission produced by the model is dominantly synchrotron emission of protons.

Protheroe et al. (2003) modelled radio to X-ray emission from the M 87 nucleus with the SPB model and predicted VHE gamma-ray flux that should be detectable by IACTs. Reimer et al. (2004) presented the SPB model in the context of VHE gamma-ray detection of M 87 by HEGRA. Figure 8.1 shows two hadronic model fits to nonsimultaneous archival data from before 2004, with data points from contemporaneous observations in 2009 spanning from radio to VHE gamma-ray wavelengths. The VERITAS spectra measured in 2007 nonflaring state and the 2010 peak flaring state are also shown to showcase how the VHE spectrum changes due to flaring activities. These hadronic model fits show steep drop-offs at TeV energies that are not compatible with observations.

8.3 Leptonic models

Several leptonic models involving synchrotron and inverse Compton (IC) radiation have been suggested, with the multicomponent emissions originating in the inner jet within the nucleus. Many of the leptonic models make use of the synchrotron self-Compton (SSC) process (Gould, 1979) where the photons from the electrons' synchrotron emissions gain energy by inverse Compton scattering off of the same population of electrons. These models are described briefly in the following paragraphs.

Abdo et al. (2009b) fitted a homogeneous one-zone SSC model using 2009 VLBA radio, Chandra X-ray, and *Fermi*-LAT measurements. No flaring activity was observed from M 87

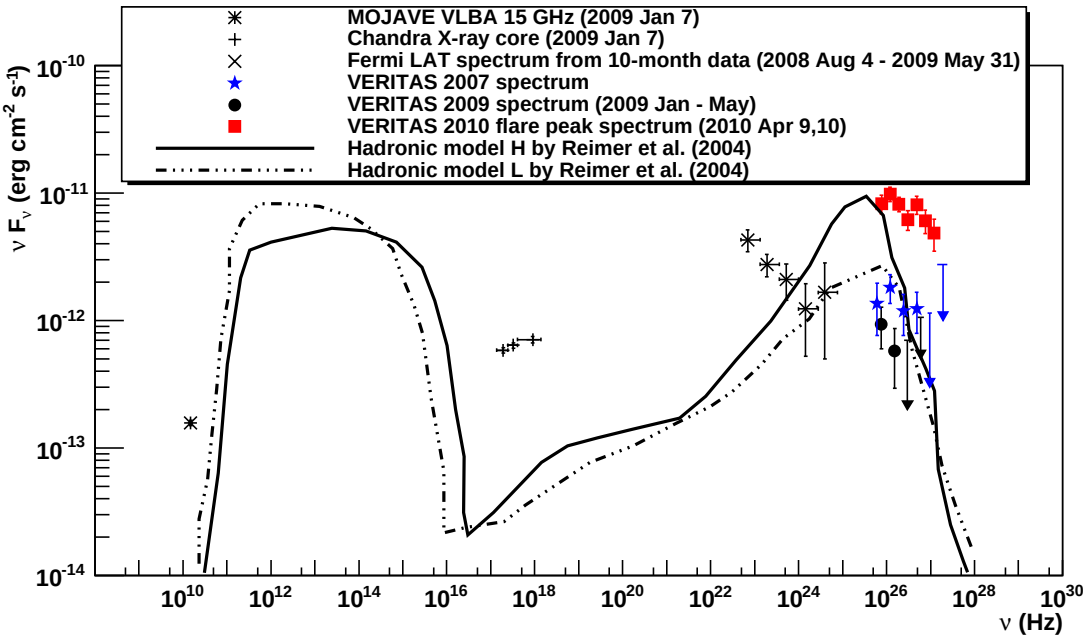

Figure 8.1. Spectral energy distribution from M 87 observations and the two model fits of the SPB model. The SPB model fits were performed on archival data from 2004 and earlier. Simultaneous multiwavelength observations in 2009 when M 87 is not flaring are shown as black points, along with nonflaring VHE spectrum in 2007 by VERITAS in blue stars, and the peak flaring VHE spectrum in 2010 by VERITAS in red squares to demonstrate the changes in spectrum due to flares. The upper limits shown in the VHE spectra are $2\,\sigma$ (95% confidence level).

at that time. Contemporaneous spectral measurement in the VHE range was difficult due to low statistics (Acciari et al., 2010), with upper limits for energies above 1 TeV. The 2009 contemporaneous measurements are shown in Figure 8.2 along with the SSC model fit by Abdo et al. (2009b). VERITAS spectral measurements of M 87 taken in 2007 when no flare was observed and in 2010 during the peak of the flare are also shown to demonstrate the different spectra due to flares.

The one-zone SSC model seems to underestimate the TeV flux. In order to fit the VHE data as well as the multiwavelength observations using a one-zone model, a low magnetic field and a very high Doppler factor would be required, as pointed out by Lenain et al. (2008) and Tavecchio & Ghisellini (2008). This is statistically unlikely given the observed angle between the jet axis and the line of sight of M 87. Therefore the synchrotron component is decoupled from the IC component and a few of these "two-zone" models are described below and are compared to data in Figure 8.3.

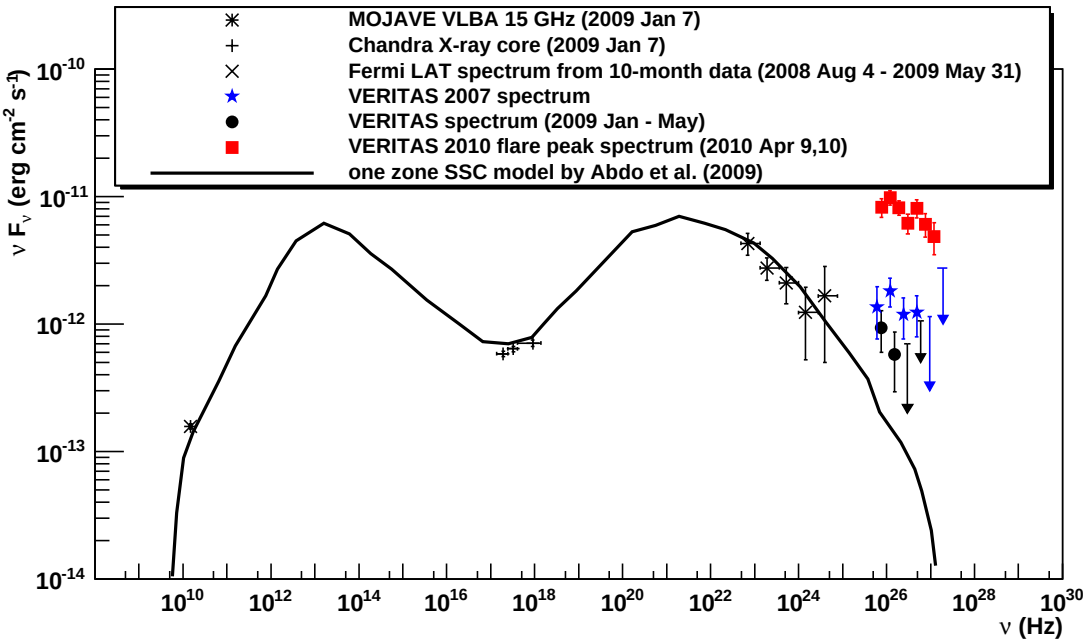

Figure 8.2. Spectral energy distribution from M 87 observations and the one-zone SSC model fit by Abdo et al. (2009b). The model fit is based on the 2009 data from VLBA, Chandra, and Fermi, and appears to underestimate the TeV flux taken within the same time period.

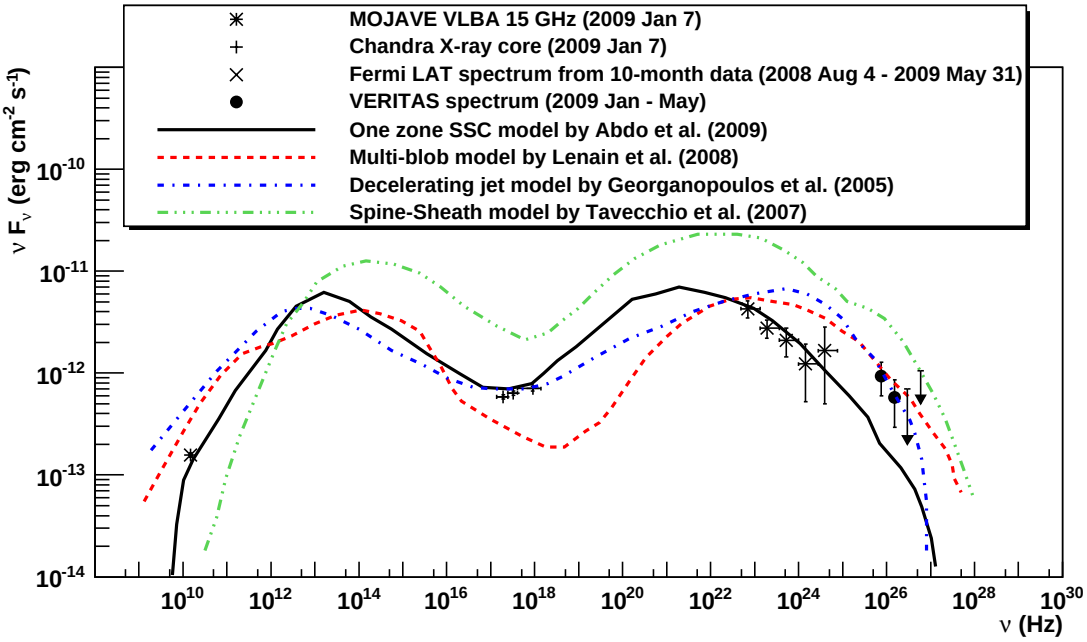

Figure 8.3. Spectral energy distribution from M 87 observations in comparison to leptonic models described in the text (Georganopoulos et al., 2005; Lenain et al., 2008; Tavecchio & Ghisellini, 2008).

Georganopoulos et al. (2005) proposed a decelerating jet scenario where over a distance of subparsec scale the jet decelerates. In the upstream where the flow is faster, the more energetic electrons inverse Compton scatter the photons produced via synchrotron emission of the less energetic electrons downstream.

Lenain et al. (2008) proposed a multiblob scenario in which VHE emission is produced via the SSC process inside several similar homogeneous compact components which contain more energetic electrons than the jet. The blobs are assumed to be located in the inner jet region within the jet, and are moving relativistically along the jet axis.

Lenain et al. (2008) presented solutions of the models that describe archival data in both flaring and nonflaring states of M 87. The multiblob scenario predicts radical change in X-rays that would correspond to flaring state observed in VHE gamma rays. So far all VHE flares are observed with a subsequent flare in X-ray. The multiblob model spectrum is also shown to harden with decreasing magnetic field. In order to keep the size of the VHE emitting region of the order of the Schwarzschild radius, the local value of the magnetic

field should be ≤ 0.01 G. Figure 8.3 shows the multiblob scenario solution along with the 2009 SED.

Tavecchio & Ghisellini (2008) proposed a scenario in which a fast-moving spine is surrounded by a slower-moving sheath, producing VHE emission via inverse Compton scattering of photons from both the spine and the sheath layer. The scenario where the fast-moving spine contributes to low frequencies emission while the slower-moving sheath layer produces TeV emissions is preferred due to constraints from model parameters. The spine-sheath model does not require low energy emission and VHE gamma-ray emission to be correlated, which is true for the 2010 flare observation where no corresponding gamma-ray flare is observed by Fermi. However, the spine-sheath model seems to face difficulties to achieve a harder spectrum in the TeV energy range due to absorption of TeV photons from interaction with background radiation in the spine. The severe gamma-ray photon absorption can be alleviated by increasing the emission region size, but this is limited by the observed short time-scale variability.

8.4 Magnetosphere model

The vicinity of the black hole (the nucleus) has been suggested as the VHE emission site by Neronov & Aharonian (2007) in the black hole magnetosphere model, in which gamma-ray photons are produced by the inverse Compton process of ultrarelativistic electron/positron pairs created by the electromagnetic cascades in the black hole magnetosphere. The magnetosphere model is further extended by Vincent & Lebohec (2010) and applied to the M 87 data in a separate publication in preparation. A large electric field can be induced near the rotating black hole by the magnetic field. Charged particles are distributed in the magnetosphere and are transported by the relativistic jet outflow. Vacuum gaps can be formed in the magnetosphere when the supply of free charges is interrupted. Electrons/positrons can be accelerated by the electric field in the vacuum gaps to very high energies and result in synchrotron and IC radiations. Figure 8.4 shows the SED of the magnetosphere model normalized to the HESS data taken in 2005 at 0.5 TeV, along with the 2009 contemporaneous data from multiple wavebands. The magnetosphere model SED appears to reproduce the general shape of the broadband SED observed in 2009, and is currently the leading model which also explains the mechanism of how the charged particles are accelerated.

Different leptonic models cannot be distinguished based on VHE data alone. The

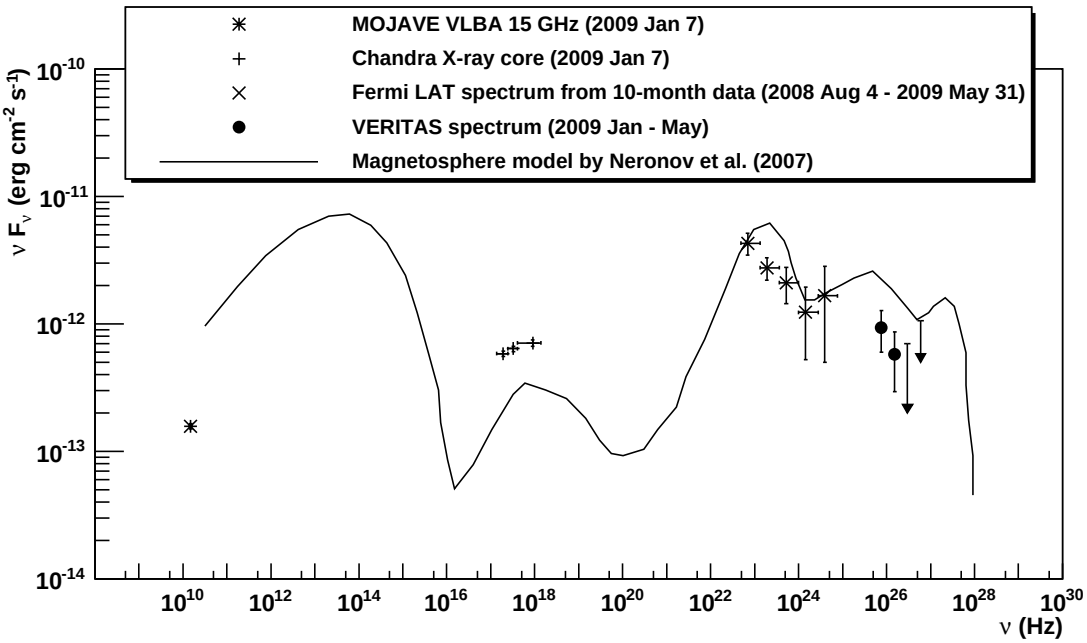

Figure 8.4. Spectral energy distribution from contemporaneous M 87 observations in 2009 and the magnetosphere model by Neronov & Aharonian (2007).

2010 flare of M 87, first reported by VHE gamma-ray telescopes (Ong & Mariotti, 2010), also has follow-up observations in X-ray, optical, and radio wavebands, giving the most complete sampling from different energy bands in comparison to the past flares which will help constrain the radiative processes involved. Multiwavelength monitoring work is being continued, and is essential to understanding particle acceleration mechanisms near black holes.

8.5 Other radio galaxies

Currently there are four radio galaxies with VHE gamma-ray emissions that were detected: M 87, Centaurus A, NGC 1275, and IC 310 (see Figure 8.5). While no population studies can be done with only four detections, the other three VHE gamma-ray detections are summarized below.

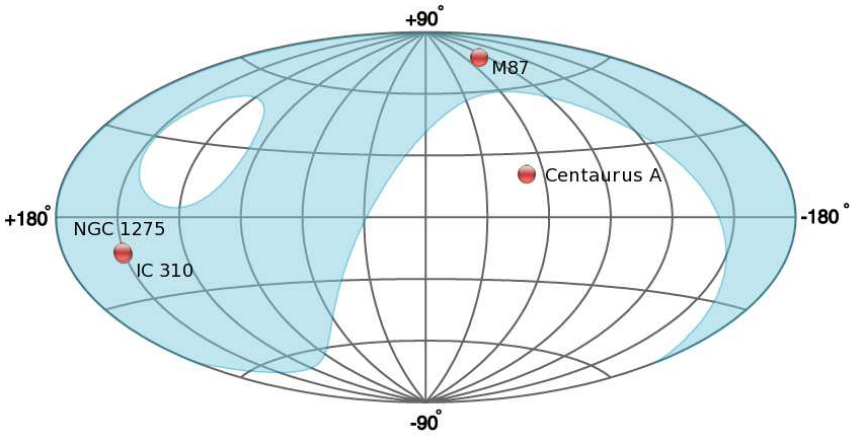

Figure 8.5. Radio galaxies detected in VHE gamma rays (reprinted with permission from Wakely & Horan (2008)). The blue shaded region is the portion of sky observable by the VERITAS array.

8.5.1 Centaurus A

Centaurus A (Cen A) is the nearest FR I radio galaxy, at a distance of 3.8 Mpc. The jet angle with respect to the line of sight is estimated between 15° and 80°. The core is believed to be a $(5.5 \pm 3.0) \times 10^7 M_\odot$ supermassive black hole. Nonthermal radiations have been observed from the nucleus and the kpc-scale jet. The inner jet structures are imaged in radio and X-ray, and with the proximity of Cen A they should be resolved by ground-based gamma-ray telescopes. The X-ray emission is consistent with a synchrotron model, suggesting the inverse Compton peak may be at gamma-ray energies (Bai & Lee, 2001). Cen A is visible for observation in the Southern Hemisphere. It was observed by the HESS array from 2004 to 2008 for over 120 hours (Aharonian et al., 2009). A statistical significance of $5\,\sigma$ is detected at a position compatible with the radio core and the inner jet region. The gamma-ray source extension upper limit is 0.2° ($\sim$ 13 kpc projected) at 95% confidence level. The flux at energies above 250 GeV is measured to be 0.8% of the Crab Nebula flux, making it one of the weakest gamma-ray source ever detected. No significant flux variability is found in the dataset. The differential photon spectrum is consistent with a power-law distribution, with a spectral index of $2.73 \pm 0.45_{\rm stat} \pm 0.2_{\rm sys}$. Both leptonic and hadronic models similar to those presented in the previous sections are compatible with the observed spectrum. Models that predict VHE gamma-ray emissions from the outer giant radio lobes however, do not match what is observed by the HESS telescopes. Further

insights from VHE gamma-ray data of Cen A to constrain models via flux and spectral variabilities require more senstive instruments than the current generation.

8.5.2 NGC 1275

NGC 1275 is a radio galaxy located in the center of the Perseus cluster at a distance of 73 Mpc. It is detected in gamma rays at energies greater than 100 MeV in 2008 (Abdo et al., 2009a). The detection is consistent with a point source. When compared to archival data, NGC 1275 appears to have significant varying flux in timescales from months to years.

Aleksić et al. (2010b) reported 24 hours of observation in Nov/Dec 2008 on the Perseus cluster, contemporaneous with the Fermi observation reported above. Upper limit on NGC 1275 is derived from these data and is consistent with the photon spectrum presented by Fermi.

VERITAS observed NGC 1275 for 11 hours in early 2009. The 99% confidence level upper limit derived from this dataset is incompatible with a simple extrapolation of the power law measured by Fermi. Contemporaneous Fermi data showed the early 2009 flux is dimmer than late 2008 flux at a statistical significance of $2.8\,\sigma$. However, flux variability alone cannot explain the nondetection by VERITAS and a viable explanation is that a cutoff in the photon energy spectrum is present or the energy spectrum follows a broken power law distribution (Acciari et al., 2009b).

After the reports of VHE gamma-ray emission upper limits, Kataoka et al. (2010) analyzed a full year's worth of Fermi data and reported month-scale variability in the dataset, and an exponential cutoff in the photon spectrum at 42.2 ± 19.6 GeV. VHE gamma-ray emission is then detected in 2010 by MAGIC after 14 hours of good quality data at a statistical significance of $5.2\,\sigma$ (Mariotti & MAGIC Collaboration, 2010). The flux is estimated to be $\sim 3\%$ of the Crab Nebula flux above 100 GeV and decreases rapidly as a function of energy. No signal is detected above 400 GeV.

8.5.3 IC 310

IC 310 is a radio galaxy located in the Perseus cluster at ~ 80 Mpc away. It is a head-tail radio galaxy, with a 15 arcminute extended "tail" aligned towards the center of the Perseus cluster. The existence of the tail is believed to be due to fast motion of the galaxy through the intracluster medium. Gamma-ray emission could be created from the inner jet region similar to M 87, or from the bow shock between the AGN outflow and the intracluster medium. The two possibilities would result in very different flux variability time scales,

from the light crossing time of the central supermassive black hole, to kpc scale where gamma-ray emission cannot be variable in less than 10^3 years.

Neronov et al. (2010) analyzed the Fermi LAT data and extracted photons above 100 GeV from the position of IC 310. This resulted in a $4.5\,\sigma$ detection at energies above 100 GeV. The IC 310 detection is 0.6° from the radio galaxy NGC 1275. NGC 1275 gamma-ray emission detected by Fermi is point-like and contained within a circle of radius 0.3°. Therefore the probability of photon contamination from NGC 1275 to the IC 310 detection is low. Flux variability cannot be determined due to the low photon statistics.

VHE gamma-ray emission from IC 310 is detected by the MAGIC telescopes at a statistical significance of $7.6\,\sigma$ after ~ 21 hours of observation between 2008 and 2010 (Aleksić et al., 2010a). The angular resolution of the MAGIC telescopes is not sufficient to determine the location of the VHE emission within IC 310. Unlike M 87, there is no strong flare in multiple wavebands to constrain the emission origin. In the 2008 dataset, only an upper limit for energies above 300 GeV is established at 1.9% of the Crab Nebula flux, while in the 2009/2010 dataset the flux is observed to be 2.5 ± 0.4% of the Crab Nebula flux. Light curve fitting showed hints of flux variability at a statistical significance of $\sim 3\,\sigma$. The observed VHE differential spectrum is consistent with a power-law distribution, with a spectral index of 2.00 ± 0.14. The spectrum obtained from the MAGIC observation is in good agreement with the spectrum presented by Neronov et al. (2010), consistent with a straight power law distribution without any breaks between 0.02 TeV and 7 TeV. Both hadronic and leptonic models are possible scenarios for the detection of gamma-ray emission from IC 310.

Overall, M 87 is the only radio galaxy that has been consistently detected in VHE gamma rays whether or not there are flaring activities. Cen A, despite being four times closer in distance, is one of the faintest VHE gamma-ray source detected, with no observed variability. NGC 1275 is detected only during a period of elevated flux so far, and the photon energy spectrum appears to have an exponential cutoff below 100 GeV. IC 310 is detected at a flux level similar to that of M 87, but no flux variability is found within the 2-year dataset. Its photon energy spectrum is harder than M 87's, i.e., the flux of IC 310 does not decrease as a function of energy as quickly as the flux of M 87.

Since the first year of observation of the Fermi LAT, a total of 7 radio galaxies are detected in the MeV-GeV gamma rays. Follow-up VHE observations are proposed to the other 3 radio galaxies that have not been detected in the GeV-TeV energy range. Improvement in the VHE instrument sensitivity, part of the future generation instrument

planning, can also help with detection of radio galaxies with weak VHE emission and flux variability, and with the spectral studies of these sources.

CHAPTER 9

CONCLUDING REMARKS

The field of ground-based gamma-ray astronomy has advanced significantly in the past decade, from having a handful of detections mostly of AGNs in 2000, to over 100 VHE gamma-ray sources of various classifications both galactic and extragalactic. The majority of the extragalactic sources are blazars, AGNs with the relativistic jet axis aligned with our line of sight. According to the unification scheme, radio galaxies are misaligned blazars. The jet misalignment of radio galaxies allows us to study jet morphology in ways that would not be otherwise possible. Of the 4 radio galaxies with known VHE emissions, M 87 is the only one that has been readily detected with multiple flares observed across the electromagnetic spectrum.

Gamma-ray photons have been predicted to be observable from M 87 since the 1960s, but no detection was reported until 2003. Shortly after, flaring activity was reported in 2005 and has been observed again in 2008 and 2010. From the VHE gamma-ray variability timescale of less than a day, the size of the VHE emission origin is constrained to within a radius of $1.3\delta R_s$, where δ is the relativistic Doppler factor and R_s is the Schwarzschild radius of the central black hole. However, due to the angular resolution of ground-based VHE gamma-ray telescopes, the emission location is not resolved within M 87. To resolve the jet of M 87, radio to X-ray observations are needed. Multiwavelength monitoring campaign during the M 87 flares showed correlated activities with the nucleus of M 87 instead of any jet features further away. During the VHE flare of 2008, radio and X-ray both showed increased flux from the nucleus instead of the nearby knot HST-1. This suggests the VHE emission originates from the nucleus region of M 87. Furthermore, this was the first establishment of association between radio waves and VHE gamma rays in AGN flare. The radio observation constraint the emission to less than $100\,R_s$ from the center. Combined with the VHE emission size constraint, this gives an upper limit of the relativistic Doppler factor which is important for modelling the emission processes and particle acceleration mechanisms.

Currently only the nonflaring 2009 data show a spectrum energy distribution from radio

to TeV gamma rays, and are best reproduced by leptonic models. To continue the study of particle acceleration and emission processes, broadband energy spectra are needed for both flaring and nonflaring periods in order to distinguish the different leptonic models that have been proposed. Also, the past two flares are well-sampled by VHE experiments, but not as well in the other wavelengths. Continual multiwavelength monitoring is needed to further study the timescales when lower energy emissions start increasing and decreasing in comparison to the VHE emissions. This could provide further insights into the AGN environment.

REFERENCES

Abdo, A. A., et al. 2009a, Astrophys. J., 699, 31

—. 2009b, Astrophys. J., 707, 55

—. 2011a, Science, 331, 739

—. 2011b, Astrophys. J., 727, 129

Abramowski, A., et al. 2011, Astrophys. J., accepted

Acciari, V. A., et al. 2008, Astrophys. J., 679, 397

—. 2009a, Science, 325, 444

—. 2009b, Astrophys. J., Lett., 706, L275

—. 2010, Astrophys. J., 716, 819

—. 2011a, Astrophys. J., 729, 2

—. 2011b, Astrophys. J., 738, 25

Acero, F., et al. 2009, Science, 326, 1080

Aharonian, F., Buckley, J., Kifune, T., & Sinnis, G. 2008, Reports on Progress in Physics, 71, 096901

Aharonian, F., et al. 2003, Astron. Astrophys., 403, L1

—. 2006a, Science, 314, 1424

—. 2006b, Astron. Astrophys., 457, 899

—. 2009, Astrophys. J., Lett., 695, L40

Aharonian, F. A. 2004, Very High Energy Cosmic Gamma Radiation : A Crucial Window on the Extreme Universe (River Edge, NJ: World Scientific Publishing)

Aharonian, F. A., et al. 2000, Astrophys. J., 539, 317

Albert, J., et al. 2008a, Astrophys. J., Lett., 685, L23

—. 2008b, Astrophys. J., 674, 1037

Aleksić, J., et al. 2010a, Astrophys. J., Lett., 723, L207

—. 2010b, Astrophys. J., 710, 634

Aliu, E., et al. 2008, Science, 322, 1221

Atwood, W. B., et al. 2009, Astrophys. J., 697, 1071

Bai, J. M., & Lee, M. G. 2001, Astrophys. J., Lett., 549, L173

Baltz, E. A., Briot, C., Salati, P., Taillet, R., & Silk, J. 2000, Phys. Rev. D, 61, 023514

Beilicke, M., Hui, C. M., Mazin, D., Raue, M., Wagner, R. M., & Wagner, S. 2008, in American Institute of Physics Conference Series, Vol. 1085, American Institute of Physics Conference Series, ed. F. A. Aharonian, W. Hofmann, & F. Rieger, 553–556

Benlloch, S., Rothschild, R. E., Wilms, J., Reynolds, C. S., Heindl, W. A., & Staubert, R. 2001, Astron. Astrophys., 371, 858

Berge, D., Funk, S., & Hinton, J. 2007, Astron. Astrophys., 466, 1219

Bicknell, G. V., & Begelman, M. C. 1996, Astrophys. J., 467, 597

Biermann, P. L., Ahn, E.-J., Medina-Tanco, G., & Stanev, T. 2000, Nuclear Physics B Proceedings Supplements, 87, 417

Biretta, J. A., Sparks, W. B., & Macchetto, F. 1999, Astrophys. J., 520, 621

Biretta, J. A., Zhou, F., & Owen, F. N. 1995, Astrophys. J., 447, 582

Bucholtz, A. 1995, Appl. Opt., 34, 2765

Caraveo, P., et al. 2010, The Astronomer's Telegram, 2903, http://www.astronomerstelegram.org

Chang, C. S., Ros, E., Kovalev, Y. Y., & Lister, M. L. 2010, Astron. Astrophys., 515, A38

Cheung, C. C., Harris, D. E., & Stawarz, Ł. 2007, Astrophys. J., Lett., 663, L65

Curtis, H. D. 1918, Publications of Lick Observatory, 13, 9

Das, A., & Ferbel, T. 2004, Introduction to Nuclear and Particle Physics - 2nd ed. (River Edge, NJ: World Scientific)

Duke, C., & LeBohec, S. L. 2011, GrISU(tah) analysis package, http://www.physics.utah.edu/gammaray/GrISU

Espinoza, C. M., Jordan, C., Stappers, B. W., Lyne, A. G., Weltevrede, P., Cognard, I., & Theureau, G. 2010, The Astronomer's Telegram, 2889, http://www.astronomerstelegram.org

Evangelista, Y., et al. 2010, The Astronomer's Telegram, 2866, http://www.astronomerstelegram.org

Fanaroff, B. L., & Riley, J. M. 1974, Mon. Not. R. Astron. Soc., 167, 31P

Ferrigno, C., Tennant, A., Horns, D., Weisskopf, M. C., Neronov, A., Tavani, M., Costa, E., & Caraveo, P. 2010a, The Astronomer's Telegram, 2994, http://www.astronomerstelegram.org

Ferrigno, C., Walter, R., Bozzo, E., & Bordas, P. 2010b, The Astronomer's Telegram, 2856, http://www.astronomerstelegram.org

Galante, N., & the VERITAS Collaboration. 2011, in International Cosmic Ray Conference, 32nd International Cosmic Ray Conference, 782

Galbraith, W., & Jelley, J. V. 1953, Nature, 171, 349

Gebhardt, K., Adams, J., Richstone, D., Lauer, T. R., Faber, S. M., Gültekin, K., Murphy, J., & Tremaine, S. 2011, Astrophys. J., 729, 119

Georganopoulos, M., Perlman, E. S., & Kazanas, D. 2005, Astrophys. J., Lett., 634, L33

Götting, N. 2006, Ph.D. thesis, Univ. Hamburg

Gould, R. J. 1965, Physical Review Letters, 15, 577

—. 1979, Astron. Astrophys., 76, 306

Hanna, D. 2008, in International Cosmic Ray Conference, Vol. 3, International Cosmic Ray Conference, 1417–1420

Harris, D. E., Biretta, J. A., Junor, W., Perlman, E. S., Sparks, W. B., & Wilson, A. S. 2003, Astrophys. J., Lett., 586, L41

Harris, D. E., Cheung, C. C., Biretta, J. A., Sparks, W. B., Junor, W., Perlman, E. S., & Wilson, A. S. 2006, Astrophys. J., 640, 211

Harris, D. E., Cheung, C. C., Stawarz, Ł., Biretta, J. A., & Perlman, E. S. 2009, Astrophys. J., 699, 305

Helene, O. 1983, Nuclear Instruments and Methods in Physics Research, 212, 319

Hillas, A. M. 1982a, Journal of Physics G Nuclear Physics, 8, 1461

—. 1982b, Journal of Physics G Nuclear Physics, 8, 1475

Hillas, A. M. 1985, in International Cosmic Ray Conference, Vol. 3, International Cosmic Ray Conference, ed. F. C. Jones, 445–448

Hillas, A. M., et al. 1998, Astrophys. J., 503, 744

Holder, J., et al. 2006, Astroparticle Physics, 25, 391

Horns, D., Tennant, A., Ferrigno, C., Weisskopf, M. C., Neronov, A., Tavani, M., Costa, E., & Caraveo, P. 2010, The Astronomer's Telegram, 3058, http://www.astronomerstelegram.org

Jelley, J. V. 1958, Cerenkov Radiation and its Applications (New York, NY: Pergamon)

Kanbach, G., Kruehler, T., Steiakaki, A., & Mignani, R. 2010, The Astronomer's Telegram, 2867, http://www.astronomerstelegram.org

Kataoka, J., et al. 2010, Astrophys. J., 715, 554

Kerker, M. 1969, The Scattering of Light and Other Electromagnetic Radiation (London, UK: Academic Press)

Kovalev, Y. Y., Lister, M. L., Homan, D. C., & Kellermann, K. I. 2007, Astrophys. J., Lett., 668, L27

Krennrich, F., et al. 2002, Astrophys. J., Lett., 575, L9

Le Bohec, S., et al. 2004, Astrophys. J., 610, 156

Lenain, J., Boisson, C., Sol, H., & Katarzyński, K. 2008, Astron. Astrophys., 478, 111

Levine, A. M., Bradt, H., Cui, W., Jernigan, J. G., Morgan, E. H., Remillard, R., Shirey, R. E., & Smith, D. A. 1996, Astrophys. J., Lett., 469, L33

Li, T., & Ma, Y. 1983, Astrophys. J., 272, 317

Longair, M. S. 2004, High Energy Astrophysics. Volume 1 Particles, Photons and Their Detection - 2nd ed. (Cambridge, UK: Cambridge)

Ly, C., Walker, R. C., & Junor, W. 2007, Astrophys. J., 660, 200

Mariotti, M. 2010a, The Astronomer's Telegram, 2431, http://www.astronomerstelegram.org

—. 2010b, The Astronomer's Telegram, 2967, http://www.astronomerstelegram.org

Mariotti, M., & MAGIC Collaboration. 2010, The Astronomer's Telegram, 2916, http://www.astronomerstelegram.org

Marshall, H. L., Miller, B. P., Davis, D. S., Perlman, E. S., Wise, M., Canizares, C. R., & Harris, D. E. 2002, Astrophys. J., 564, 683

McCartney, E. J. 1976, Optics of the Atmosphere (New York, NY: John Wiley & Sons, Inc.)

Mei, S., et al. 2007, Astrophys. J., 655, 144

Mücke, A., & Protheroe, R. J. 2000, in American Institute of Physics Conference Series, Vol. 515, American Institute of Physics Conference Series, ed. B. L. Dingus, M. H. Salamon, & D. B. Kieda, 149–153

Mücke, A., & Protheroe, R. J. 2001, Astroparticle Physics, 15, 121

Neronov, A., & Aharonian, F. A. 2007, Astrophys. J., 671, 85

Neronov, A., Semikoz, D., & Vovk, I. 2010, Astron. Astrophys., 519, L6

Ong, R. A. 2010, The Astronomer's Telegram, 2968, http://www.astronomerstelegram.org

Ong, R. A., & Mariotti, M. 2010, The Astronomer's Telegram, 2542, http://www.astronomerstelegram.org

Ostlie, D. A., & Carroll, B. W. 1996, An Introduction to Modern Stellar Astrophysics (San Francisco, CA: Pearson Addison-Wesley)

Owen, F. N., Eilek, J. A., & Kassim, N. E. 2000, Astrophys. J., 543, 611

Peck, E. R., & Reeder, K. 1972, Journal of the Optical Society of America (1917-1983), 62, 958

Perkins, J. S., Maier, G., & The VERITAS Collaboration. 2009, ArXiv e-prints: 0912.3841

Perlman, E. S., Harris, D. E., Biretta, J. A., Sparks, W. B., & Macchetto, F. D. 2003, Astrophys. J., Lett., 599, L65

Perlman, E. S., Sparks, W. B., Radomski, J., Packham, C., Fisher, R. S., Piña, R., & Biretta, J. A. 2001, Astrophys. J., Lett., 561, L51

Perlman, E. S., & Wilson, A. S. 2005, Astrophys. J., 627, 140

Pfrommer, C., & Enßlin, T. A. 2003, Astron. Astrophys., 407, L73

Price, R., Vincent, S., & Lebohec, S. 2011, Astroparticle Physics, 34, 871

Protheroe, R. J., Donea, A., & Reimer, A. 2003, Astroparticle Physics, 19, 559

Punch, M., et al. 1992, Nature, 358, 477

Quinn, J., et al. 1996, Astrophys. J., Lett., 456, L83

Reimer, A., Protheroe, R. J., & Donea, A. 2004, Astron. Astrophys., 419, 89

Reynolds, C. S., Heinz, S., Fabian, A. C., & Begelman, M. C. 1999, Astrophys. J., 521, 99

Rieke, G. H., & Weekes, T. C. 1969, Astrophys. J., 155, 429

Schmidt, F. 2011, CORSIKA Shower Images, http://www.ast.leeds.ac.uk/$\tilde{\text{f}}$s/showerimages.html

Shaposhnikov, N., Jahoda, K., Swank, J., Strohmayer, T., Markwardt, C., & Weisskopf, M. 2010, The Astronomer's Telegram, 2872, http://www.astronomerstelegram.org

Shepherd, N., Buckley, J. H., Celik, O., Holder, J., LeBohec, S., Manseri, H., Pizlo, F., & Roberts, M. 2005, in International Cosmic Ray Conference, Vol. 5, International Cosmic Ray Conference, 427

Shepherd, N. J. 2005, Absolute Calibration of VERITAS Telescopes Using Rayleigh Scattering, Master's thesis, Univ. of Utah

Tavani, M., et al. 2009, Astron. Astrophys., 502, 995

—. 2011, Science, 331, 736

Tavecchio, F., & Ghisellini, G. 2008, Mon. Not. R. Astron. Soc., 385, L98

Tennant, A., et al. 2010, The Astronomer's Telegram, 2882, http://www.astronomerstelegram.org

Tsvetanov, Z. I., Hartig, G. F., Ford, H. C., Dopita, M. A., Kriss, G. A., Pei, Y. C., Dressel, L. L., & Harms, R. J. 1998, Astrophys. J., Lett., 493, L83

Urry, C. M., & Padovani, P. 1995, Publ.. Astron. Soc. Pac., 107, 803

van de Hulst, H. C. 1957, Light Scattering by Small Particles (New York, NY: Wiley)

VERITAS Collaboration et al. 2009, Nature, 462, 770

—. 2011, Science, 334, 69

Vincent, S., & Lebohec, S. 2010, Mon. Not. R. Astron. Soc., 409, 1183

Wakely, S. P., & Horan, D. 2008, in International Cosmic Ray Conference, Vol. 3, International Cosmic Ray Conference, 1341–1344, http://tevcat.uchicago.edu

Walker, R. C., Ly, C., Junor, W., & Hardee, P. 2009, in Astronomical Society of the Pacific Conference Series, Vol. 402, Approaching Micro-Arcsecond Resolution with VSOP-2: Astrophysics and Technologies, ed. Y. Hagiwara, E. Fomalont, M. Tsuboi, & M. Yasuhiro, 227

Weekes, T. C. 2003, Very High Energy Gamma-ray Astronomy (Birkstol, UK: The Institude of Physics Publishing)

Weekes, T. C., et al. 1989, Astrophys. J., 342, 379

Wen, L., Levine, A. M., Corbet, R. H. D., & Bradt, H. V. 2006, Astrophys. J., Suppl. Ser., 163, 372

Wilson, A. S., & Yang, Y. 2002, Astrophys. J., 568, 133